Quaternary & Late Pliocene Seismic Stratigraphy of the Central Scotian Shelf

SIMON NEWTON, 2003

Dalhousie University

Department of Earth Sciences
Halifax, Nova Scotia
Canada B3H 3J5
(902) 494-2358
FAX (902) 494-6889

DATE APRIL 30, 2003

AUTHOR CHRISTOPHER SIMON NEWTON

TITLE QUATERNARY AND LATE PLIOCENE SEISMIC STRATIGRAPHY

OF THE CENTRAL SCOTIAN SLOPE

Degree B Sc   Convocation May 20   Year 2003

Permission is herewith granted to Dalhousie University to circulate and
to have copied for non-commercial purposes, at its discretion, the above title
upon the request of individuals or institutions.

QUATERNARY and LATE PLIOCENE SEISMIC STRATIGRAPHY of the CENTRAL SCOTIAN SLOPE

Simon Newton

Department of Earth Sciences
Dalhousie University, Halifax, Nova Scotia
March 2003

ABSTRACT

High-resolution single channel seismic reflection profiles collected by the Geological Survey of Canada Atlantic (GSCA) have been used to define the Quaternary and Late Pliocene seismic stratigraphy of the central Scotian Slope, southwest of Sable Island Bank. Reflection profiles used in this study have a dominant frequency at 180 Hz providing near 1 m vertical resolution. This resolution, approximately tenfold that of industry data, is ideal for describing the seismic facies and seismic stratigraphy of Quaternary and Late Tertiary strata of the central Scotian Slope.

Late Pliocene and Quaternary strata are represented by coherent, laterally continuous reflectors that thin or pinch out down-dip. Draping of reflectors over subsurface irregularities indicate the general mode of sediment deposition is by hemipelagic drape. Pre-glacial, Late Pliocene to early Quaternary (0.45 Ma) sediment was deposited during a period of relative slope stability that is interrupted only by two major periods of erosion. Glacial, mid- to late Quaternary strata are truncated by four erosional events indicating a period of slope instability. Several key reflectors have been identified and correlated throughout the study area. Isochron maps constructed from these reflectors indicate that pre-glacial sediment accumulated uniformly on the slope, whereas glacial sediment accumulated preferentially on the upper slope. In addition, numerous examples of slope instability were observed, including sediment failures, mass transport complexes, and structures related to near surface salt deformation.

TABLE OF CONTENTS

TABLE OF FIGURES

TABLE OF TABLES

ACKNOWLEDGEMENTS

1.1 Introduction to the Central Scotian Slope

The study area on the central Scotian Slope is located approximately 250 kilometres off the coast of Nova Scotia in water depths of 200 to more than 3000 m (Figure 1.1). The study area is bounded by Verrill Canyon to the east and by the West Acadia Valley on the west. It comprises approximately 4000 km^2 of the Scotian Slope (Figure 1.2).

Previous studies of the central Scotian Slope are either regional (Piper, 2001), were accomplished using a sparse dataset (Piper *et al.*, 1987; Piper and Normark, 1989; Piper and Sparkes, 1990) or have focused on near surface sediment and slope stability (Mosher *et al.*, 1989; 1994; Gauley, 2001). An abundance of recently acquired, high-resolution, single-channel, airgun seismic reflection data (Figure 1.2) permit renewed investigations into these topics. This study attempts to describe the Plio-Pleistocene development of the central Scotian Slope and explain its evolution. Emphasis is placed on comparing pre-glacial and glacial strata. The relatively undisturbed central Scotian Slope provides an excellent opportunity to evaluate the seismic stratigraphy and depositional style of Late Pliocene and Quaternary sediments.

1.2 Scope and Objectives of Project

The primary focus of this project is the mapping and temporal constrainment of the Late Pliocene and Quaternary sediment of the central Scotian Slope. To understand
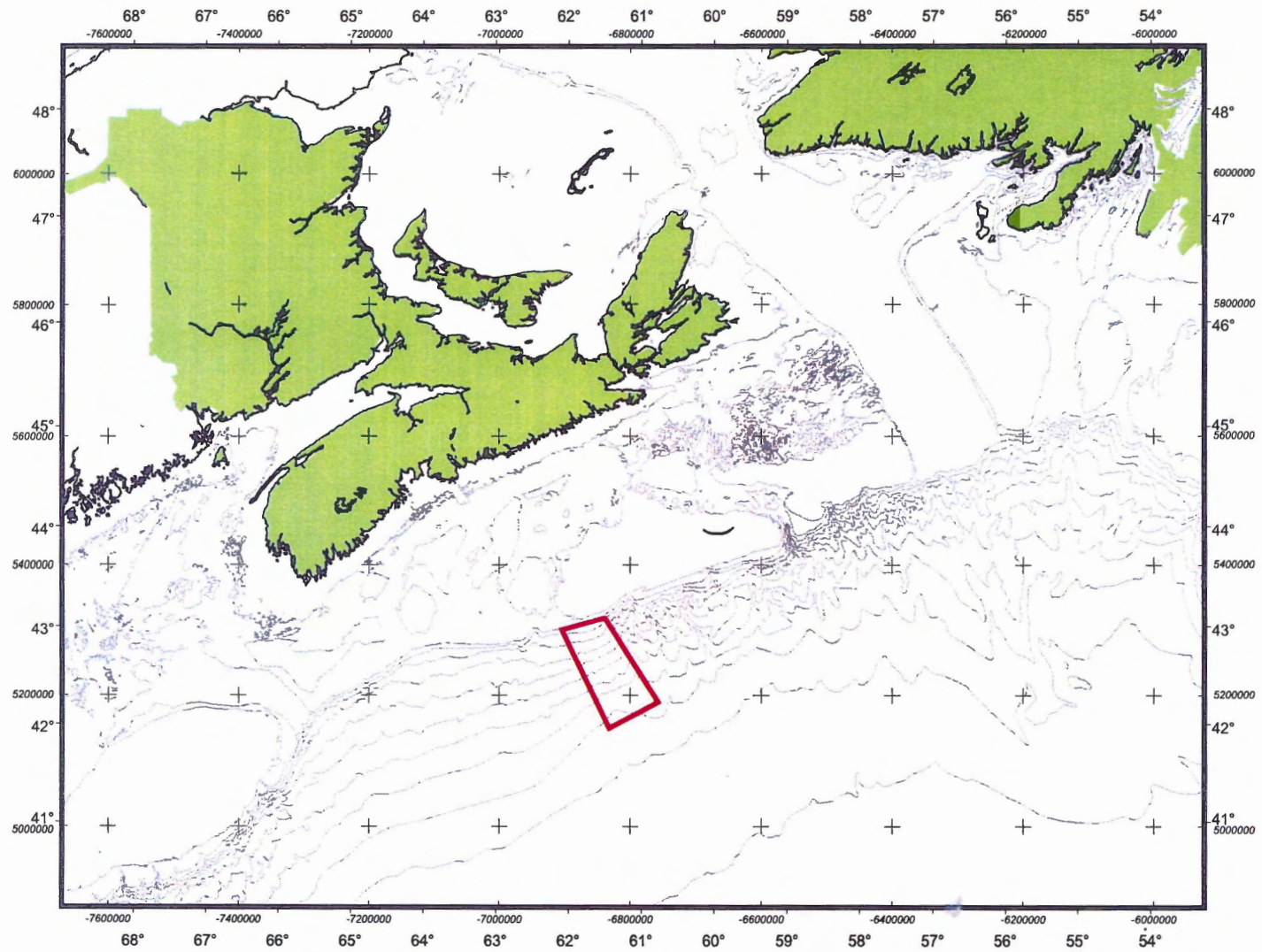
Figure 1.1: Location map of the central Scotian Slope. The study area is indicated by the red polygon.
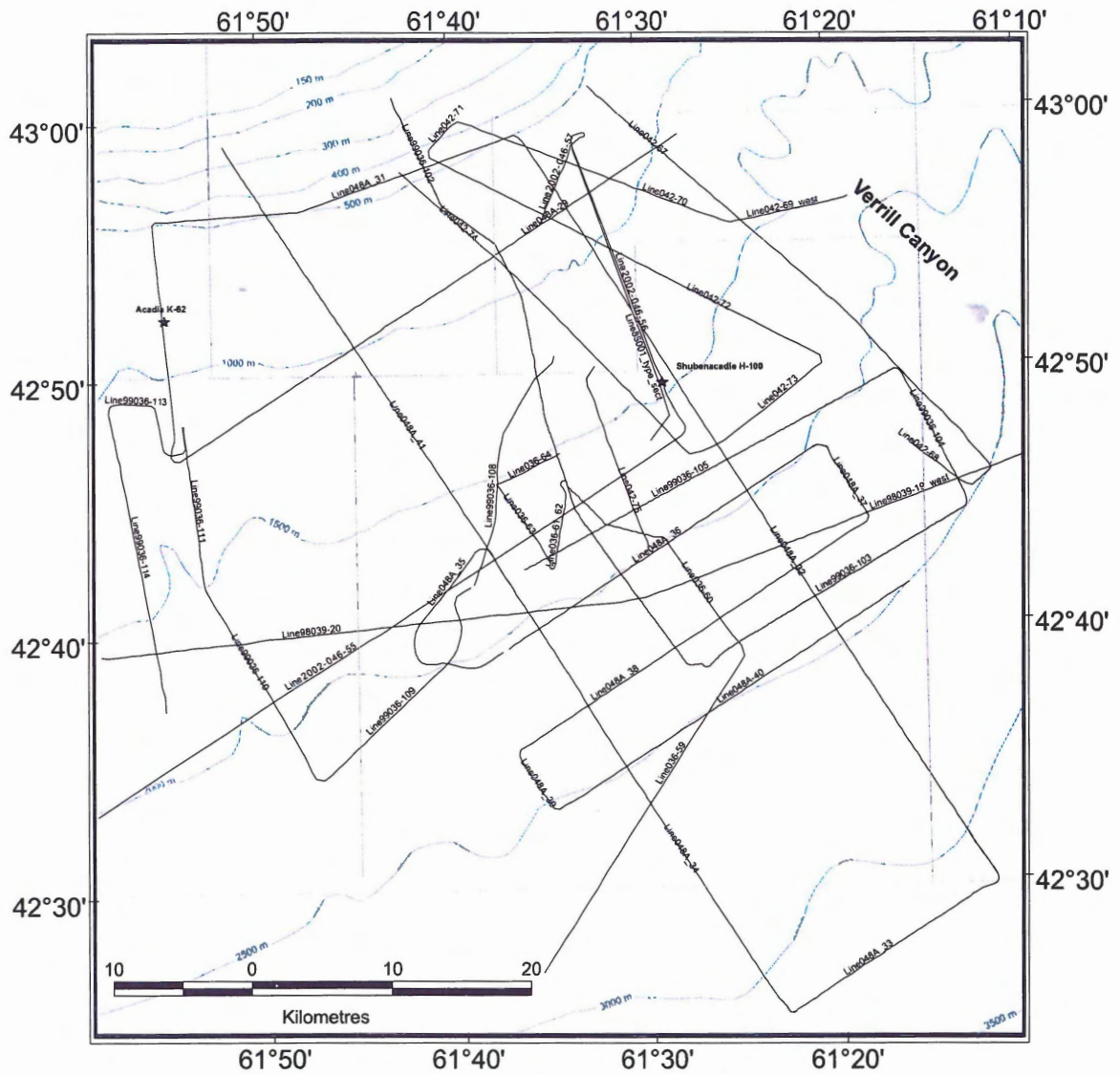
Figure 1.2: Map of study area showing seismic sections used in study with bathymetry. Stars indicate hydrocarbon exploration wellsites. Dotted lines indicate hydrocarbon lease boundaries.

the environment and time of deposition, biostratigraphic and sedimentological information from two exploration wells will be correlated to the seismic sections using synthetic seismograms. Results of this study are compared to previous studies of the Scotian Slope.

The Scotian Slope is currently under active hydrocarbon exploration, which is important from a geohazard viewpoint. This study provides synthesis of the shallow section and may help identify shallow drilling hazards.

1.3 Organization of Thesis

Chapter two outlines how the high-resolution seismic data used in this study were acquired and processed. Chapter three reviews the study area including our current understanding of the stratigraphy based on previous work. Chapter four presents the results of the project including isochron maps, a stratigraphic framework, and correlations to borehole data. Chapter five presents the depositional history of the region including its implications for geohazards, resulting conclusions, and recommendations for future work.

CHAPTER 2

DATA ACQUISITION METHODS AND ANALYSIS

2.1 General Data Types

Data used in this study include high-resolution, single channel, small airgun

(0.66 L – 1.31 L), reflection seismic sections collected by the Geological Survey of

Canada Atlantic Division (GSCA) and borehole data from two hydrocarbon exploration

wells. The majority of the seismic data used in this study were collected between 1998

and 2002 from the *CCGS Hudson*. Some paper seismic sections from earlier cruises were

also used; most notably, the type sections from Piper et al (1987) from cruises 81044 and

85001. The seismic data set is both practical and cost-effective for examining the upper

500 m of the sediment column in this environment.

2.2 Acquisition of Sleeve-Gun Reflection Data

An analysis of the procedures and fundamentals of seismic acquisition is outlined

to demonstrate the advantages and limitations of the data. Acquisition parameters for the

cruises are outlined in Table 2.1.

2.2.1 Acoustic Source

The goal of most seismic sources is a zero-phase delta-function, which would

provide the same power at all frequencies. In practice this wavelet is unattainable

(Yilmaz, 1987) and geophysical practice must work within the bounds of physical

limitations. Airguns typically produce a minimum phase wavelet with an impulse

response that approximates a delta function (Fig. 2.1). The airgun utilizes two high-

pressure chambers connected and sealed by a double-ended piston (Fig. 2.2). During

operation the two chambers are filled with high-pressure air. The gun is fired

5

Table 2.1: Some acquisition parameters for various cruises (Mosher, 2000, 2001, 2002; Piper, 1999).

Cruise	Source	Streamer	Hydrophone Array	Digitization rate (μs/sample)	Window (ms)	Low Cut (Hz)	High Cut (Hz)
85001	1 x 40 in^3 sleevegun	unknown	unknown	analog, n/a	n/a	unknown	unknown
98039	1 x 40 in^3 sleevegun	unknown	unknown	600	2397	100	500
99036	2 x 40 in^3 sleevegun array	Benthos 100 ft	75' section consists of 25 AQ-1 hydrophones at 36 in. spacing	500	1898	50	3000
2000-036	1 x 40 in^3 sleevegun	Benthos 100 ft	75' section consists of 25 AQ-1 hydrophones at 36 in. spacing	800	1500	130	3000
2000-042	1 x 40 in^3 sleevegun	Benthos 75 ft	75' section consists of 25 AQ-1 hydrophones at 36 in. spacing	800	1500	80	3500
2001-048A	2 x 40 in^3 sleevegun array	Benthos 75 ft	75' section consists of 25 AQ-1 hydrophones at 36 in. spacing	500	2048	35	1000
2002-046	2 x 40 in^3 sleevegun array	Teledyne model 178	50 T-1 acceleration-canceling hydrophones at 0.5 m spacing	250	2000	25	800

when a solenoid (S) opens a valve allowing high-pressure air to reach the underside of the piston thus allowing the piston to accelerate rapidly. This movement forces high-pressure air from the cylinder (C in fig. 2.2) to be released into the water producing a pressure wave that is the primary acoustic source (Telford *et al.*, 1976). Pressure in chamber C (fig. 2.2) decreases rapidly as air escapes into the water; pressure from the first cylinder then shuts the piston where it fills with air for a subsequent shot. Sleeveguns, a modified form of airgun, were used for the source on board the *CCGS Hudson*. Instead of having a piston and four vents to allow air to escape, a sleevegun has an outer sleeve that is moved, allowing a full 360° venting (Verbeek, 1995).
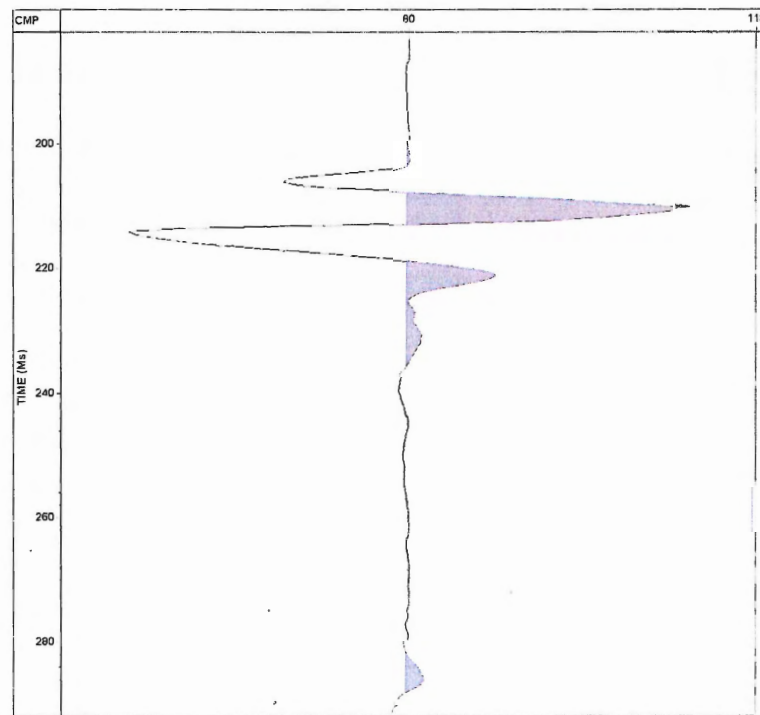
Figure 2.1: Acoustic signature of the 2 x 0.66 L sleeve gun array during Hudson 2002-046. This signature shows a good signature with both guns firing in phase (Piper and Mosher, 2002).
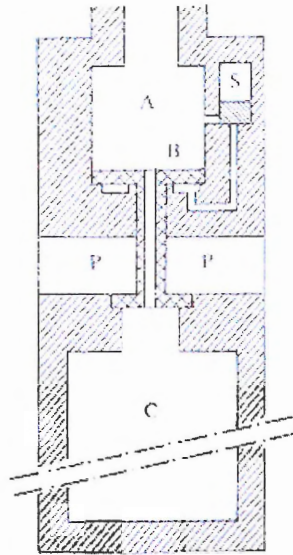
Figure 2.2: The valve of an airgun (Pieuchot, 1984)

The wavelet from a single airgun has three main components. The primary component is the primary pulse from the escaping air. This primary signature is followed by a negative pulse that is called the source ghost (Fig. 2.3). It results from the reflection of the primary pulse off the air-water interface. The deeper the gun is towed, the longer the lag time between the primary pulse and the source ghost. The initial portion of the airgun signature is the summation of these two waveforms. The summation results in notches or nulls in the frequency spectrum as certain frequencies cancel because of interference between the primary and the ghost components (Table 2.1). Notches will occur where the tow depth is half of the wavelength, or more precisely:

$$Freq = \frac{V_w}{2 \times x_t}$$

(eq. 2.1)
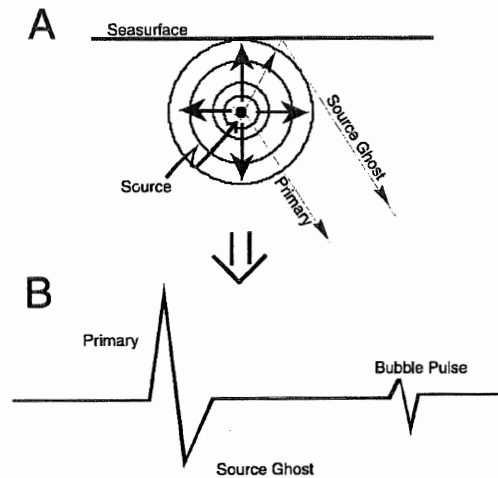
Figure 2.3: Cartoon showing wave paths of the source (A), convolving to form source signature (B) for marine air and sleeve guns (Mosher *et al.*, 1998)

Table 2.2: Gun depth and related frequency notches as a result of the convolution of the source ghost with the primary pulse. (Mosher *et al.*, 1998)

Gun depth (metres)	Notch Frequency	Notch Frequency (1st Harmonic)	Notch Frequency (2nd Harmonic)	Notch Frequency (3rd Harmonic)
0.5	1450 Hz	2900 Hz	4350 Hz	5800 Hz
0.75	967 Hz	1934 Hz	2901 Hz	3868 Hz
1.0	725 Hz	1450 Hz	2175 Hz	2900 Hz
2.0	362 Hz	725 Hz	1087 Hz	1450 Hz
3.0	242 Hz	483 Hz	725 Hz	967 Hz
4.0	181 Hz	362 Hz	544 Hz	725 Hz

The third component of the source is the bubble pulse or bubble effect. The effect is the result of the oscillation of the air bubble (the air released to produce the pressure wave), which expands and contracts until all energy is dissipated. When gas pressure exceeds hydrostatic pressure the bubble will expand. As the bubble expands the air pressure will fall bellow hydrostatic pressure, because of momentum of the expansion. As hydrostatic pressure exceeds air pressure, the net force then becomes inward resulting in a collapse of the bubble. When the bubble pressure again reaches hydrostatic pressure

the same feedback relation occurs. Seismic waves are generated as the bubble oscillates (Telford *et al.*, 1976). The lag time of the bubble pulse is related to its oscillation frequency, which is a function of the volume of air released, the air pressure at the time of release, and the ambient hydrostatic paper (Mosher, 1998). The energy from the bubble pulse may also create frequency notches when phase-reversed frequencies convolve and introduces an artifact in the seismic section that can interfere with interpretation of true reflection arrivals.

Two strategies to reduce the effects of the bubble pulse are used commonly; deconvolution filters and tuned arrays of airguns. Mosher *et al.* (1998) demonstrate how carefully tuned arrays of airguns reduce the effect of the bubble pulse. It is thought that the bubble pulses from two or more guns destructively interfere (Mosher, 1998). Aside from attenuating the bubble pulse, multiple airgun arrays increase the energy of the source without increasing the low frequency content of the signal, as would be the case with increasing gun size. Some data used in this study were acquired with a single airgun array and they have shallower penetration depths and lower signal to noise ratios compared to data acquired with a dual air-gun array.

Three factors affect the frequency content of the airgun source: shooting depth, pressure of the compressed air, and the volume of air (Pieuchot, 1984). With increased hydrostatic pressure at depth, the bubble from the airgun becomes smaller resulting in a higher frequency content; however, increasing the depth also serves to increase the energy of the bubble pulse and reduce the frequency content of the source signature. Higher pressure of compressed air increases the volume of the bubble, thereby increasing lower frequency content of the signal, as does increasing the volume of the air released.

Seismic acquisition parameters vary from cruise to cruise. The use of dual airgun arrays results in improved seismic data, because of higher energy and reduced bubble oscillation effects. Spectral analysis of the seismic data show frequency notching typically at approximately 200 Hz, suggesting a tow depth of 3.7 m for the airgun.

2.2.2 Streamer

Hydrophones are made of piezoelectric material, which produces an electrical potential when deformed (usually in ceramics of barium titanate or zirco-titanate of lead; Pieuchot, 1984). During seismic acquisition, pressure from the returning P-wave deforms the ceramic producing a charge. The elements of a hydrophone will also produce a charge when subjected to acceleration. For this reason, boat movements and waves produce significant noise below 30 Hz (Mosher pers. comm., 2002). This noise can be reduced through the use of acceleration-canceling hydrophones. By assembling two parallel elements (Fig. 4), the voltages produced by acceleration cancel each other whereas those produced by pressure of the seismic signal sum. All seismic sections recorded prior to 2002 at GSCA were captured using arrays of non-acceleration canceling hydrophones, suggesting that frequencies below 30Hz are dominated by noise.
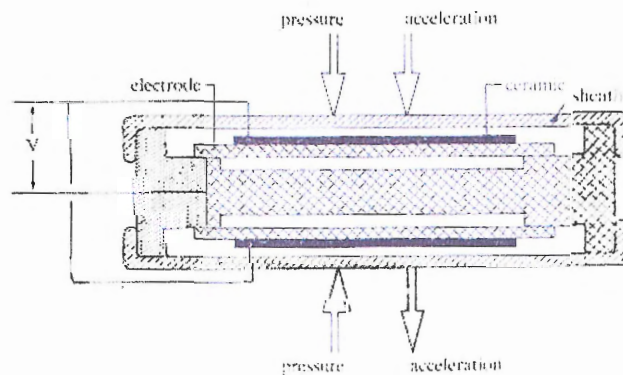
Figure 2.4: Schematic cross-section of an acceleration canceling piezo-electric hydrophone (Pieuchot, 1984)

11

Multiple hydrophones are typically arranged in arrays (in parallel) to sum and increase signal to noise ratios. The output of the hydrophones within the array is summed; however, to add constructively, the recorded signals of all the hydrophones must be in phase. The travel distance of the seismic signal between the nearest and farthest hydrophone in an array must be smaller than a quarter of the wavelength signal for the signal to add constructively (Verbeek, 1995).

Streamers are typically filled with a low-density fluid so as to achieve neutral buoyancy. The tow depth of the streamer is also important, as the signal may also be ghosted, called the receiver ghost. The streamer is typically towed at the same depth as the source, resulting in no further frequency notching.

2.2.3 Data logging

Data were recorded simultaneously by a digitizer and an electro-static analogue recorder. Acquisition parameters varied from cruise to cruise (Table 2.1). The signal was first passed through a Krohn-Hite filter with the low- and high-cut frequencies to ensure clean signal and Nyquist sampling criteria are met. Gain was applied (20 – 40 dB) to ensure appropriate signal levels. The signal was digitized using GSCA in-house software AGCDIG. A digitization rate of 500 µs means that the highest frequency that can be sampled, i.e. the Nyquist frequency, is 2000 Hz. A 1.5 to 2.4 second window was used because the seismic signal tends to be attenuated after 800 ms TWTT. The time window was shifted to account for deepwater delays. Water column time thicknesses can exceed 3.0 seconds TWTT at the base of the slope. Time delays for the seismic sections were recorded in the watch-keepers log and were restored in later processing. The

digitized seismic sections were stored on Exabyte tapes in a modified SEG-Y format for later retrieval.

2.3 Processing of Sleeve-Gun Reflection Data

The goal of seismic processing is to transform a recorded seismogram into a representation of the Earth's impulse response. In a typical industry setting there are three main processes: deconvolution, stacking, and migration (Yilmaz, 1987). Single-channel seismic data cannot be stacked.

Deconvolution can be used to increase resolution by compressing the basic seismic wavelet to approximate a spike and to suppress reverberating wave trains. A deconvolution could also be used to eliminate some of the effects of the seafloor multiple. Unfortunately, time constraints and volume of data made deconvolution impossible within the time-frame of this study. The drawback to the lack of deconvolution is that some resolution is lost, and the seismic data may be more difficult to interpret especially where the source signature is complex.

Migration is performed to increase lateral resolution by collapsing diffractions and moving dipping events to their true subsurface position. Effectiveness of migration requires a well-defined velocity model. Multi-channel seismic data reduces this variable through normal move-out (NMO) velocity analysis, which produce RMS (stacking) velocities.

Velocity information within the Late Pliocene and Quaternary strata of the central Scotian Slope is limited. Velocity data were analyzed from three sources: well site logs and piston core measurements, stacking velocities from high-resolution multi-channel

seismic data, and from a recent ocean bottom seismometer (OBS) wide-angle reflection deployment (LeBlanc, 2002). Direct measurement of velocity is only available for the near surface through piston cores, and for deeper strata through well site geophysical logs. The seismic sections remain unmigrated because of poor velocity constraints, and volume of data.

Seismic post-processing is a labor and computer intensive operation. The data examined in this study have not been intensively post-processed by GSCA or by the author. Typical processing involves frequency filtering and a gain function. Frequency filtering is used to eliminate unusable frequencies. In lines acquired using non-acceleration canceling hydrophones, frequencies below 60 Hz are considered noise. Frequency content of the source is minimal at approximately 400 Hz; any content above this frequency may also be considered noise. For this reason a trapezoid band-pass frequency filter has been applied to all seismic sections. A trapezoid-shaped filter prevents ringing that occurs if the filter slopes are too sharp (Gibbs phenomenon). Automatic gain control is applied to account for attenuation of the seismic signal with depth. While gain enhances the amplitude of deeper horizons, it also enhances noise.

2.4 Analysis of Sleeve-Gun Reflection Data

Seismic data are analyzed in three stages for this report. All seismic data were analyzed and interpreted in Seismic Micro-Technology, Inc. The Kingdom Suite+ 7.0™ (TKS) computer application for Windows™ based personal computers.
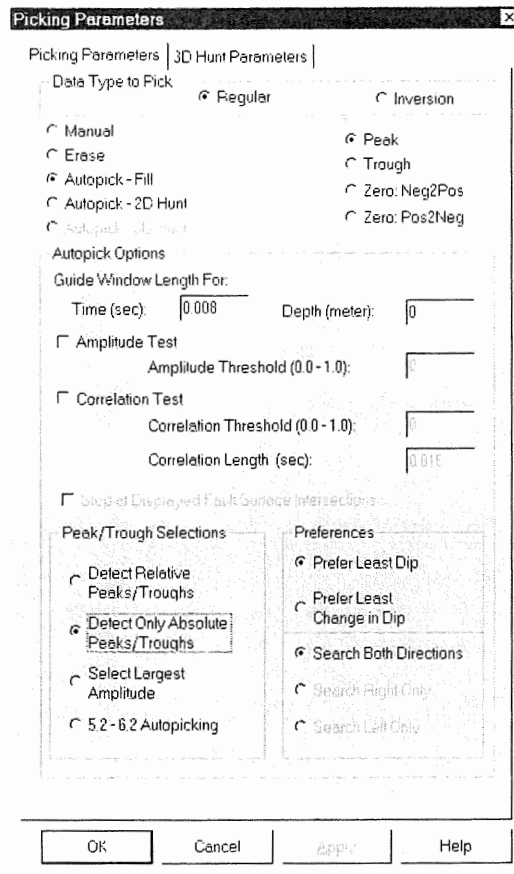
Figure 2.5: Horizon picking parameters of TKS

Key horizons from previous work were correlated with the data used in this study. Horizons established by Piper and Sparkes (1990) throughout the study area were correlated based on their type section line 81044-44. This type section, located on the upper slope, compares well with single-channel data used in this study. Horizons were then extended through the study area.

There are three modes (Table 2.3) and four attributes (Table 2.4) for conducting digital horizon picking. In general, the most effective for high-resolution data are the fill mode using absolute peaks or toughs. The fill mode was used for most picks in this

15

study. Where data were noisy, relative peaks and troughs were picked. Faults and

significant discontinuities were digitized concurrently with horizon picking.

Table 2.3: Picking tools available in TKS.

Picking Mode	Description
Manual	Pick points as they are digitized with single left-button mouse clicks
Autopick – Fill	Let the autopicker pick between digitized points with the event dropped to the appropriate phase while honoring the guide window. Points are digitized with single left mouse button clicks.
Autopick – 2D Hunt	Let the autopicker pick in both directions from a single click. Picking will stop at the end of the event.

Table 2.4: Methods to pick wave phases provided by TKS.

Phase	Description
Peak	A parabola is fit to three samples near the peak. The peak time and amplitude are computed from the parabolic fit.
Trough	A parabola is fit to the three samples near the trough. The trough time and amplitude are computed from the parabolic fit.
Zero-crossing (negative to positive)	Time is computed by linear interpolation between negative amplitude and a positive amplitude one sample later
Zero-crossing (positive to negative)	Time is computed by linear interpolation between positive amplitude and a negative amplitude one sample later.

Two picks have been made for each reflector; the first pick reflects only where the

event exits and the second is a duplicate of the first, except that picks have been extended

through correlative time surfaces where they do not exist. That is, where a reflector has

been eroded, the base of the erosion is selected for that pick. This second set of picks

was used to construct the structure and isochron maps (Appendix A, B).

16

Structure and isochron maps were created from gridded horizon information. They were gridded using an inverse to a power algorithm provided by TKS. In the inverse to a power algorithm, data points have decreasing weight with distance that varies with the power used. The structure maps were gridded using a power of one, such that the weight of given data point decreases linearly with distance. A power of one was selected because of the gradient of the seafloor; if a higher power were used, then strike sections would cause pronounced "highs" in the data that might be interpreted as actual features. The isochron maps were gridded using a power of two, such that the weight of given data point decreases exponentially with distance. A power of two was selected because interval thickness is variable over the study area and the regional gradient is weak. Data were gridded at 250 by 250 m pixels using low smoothing option. Maximum distance from a point was set at 15 km for the structure maps; this means that any points at a greater distance than 15 km from a pixel being gridded is not considered. Maximum distance from a point was set at 10 km for the isochron maps. Some control points were added to aid the gridding function in areas of sparse data.

Interval interpretation maps (Appendix C) were created based on interpreted seismic sections. The interpretation maps depict significant features within intervals including erosional surfaces (escarpments, channels), faulting, and deformation of strata. These maps do not show the timing of the events, but rather the effect of a given event. For example, a major escarpment in the western portion of the study area erodes strata from several intervals. This escarpment is mapped on all the intervals eroded as opposed to the stratigraphic horizon where the event occurred.

2.5 Wellsite Data

The two hydrocarbon exploration wells drilled within the area are outlined in Table 2.5. Well data, including digital logs, were derived from the GSCA Basin Database.

Table 2.5: Exploration wells within the study area.

Wells	Spud Date	RT (m)	Water Depth (m)	TD (m)	First Cuttings (m)	Last Sonic Reading (m)
Acadia K-62	April 11, 1978	12.6	866.3	5287.4	1200	1185
Shubenacadie H-100	November 2, 1982	24	1476.5	4200.0	2145	2581

2.6 Synthetic Seismograms

The synthetic seismogram is a mathematical model of the reflection seismogram. Synpak is a TKS module for creating synthetic seismograms using digital well logs of velocity and/or density. Synthetic seismograms allow correlation between seismic sections, which are in time, with borehole data, which are in depth. Changes in velocity and density in the lithological section produce impedance contrasts. The change in impedence is the reflectivity coefficient. Synpak convolves the measured reflection coefficient series with a desired wavelet.

2.7 Velocity Model

A velocity model is required for conversion of traveltime data. As indicated in section 2.3, velocity information is available from three sources: velocity logs from core and well control, one ocean bottom seismometer experiment (wide-angle reflection), and move-out velocities for high-resolution multi-channel lines acquired on GSCA cruise

81044. These data were analyzed and compared in an effort to produce an approximate velocity profile; however, discrepancies between the velocity information from various sources and lack of velocity information in deeper regions prevented the creation of a velocity model for the study area.

CHAPTER 3

BACKGROUND GEOLOGY

3.1 Stratigraphic and Tectonic Overview

The Atlantic margin developed with the Late Triassic rifting of the Pangaean supercontinent. This synrift phase is represented by thick sequences of both marine and non-marine late Mesozoic through Cenozoic sediments (Keen *et al.*, 1990). A brief summary of the stratigraphy is provided for reference (Fig. 3.1). Basement is overlain by Eurydice Formation redbeds and Argo Formation evaporites. Evaporite deposition terminated during the Early Jurassic (Wade and MacLean, 1990) and is succeeded by continental clastics and shallow marine dolostones of the Mohican and Iroquois formations. Clastic and carbonate strata of the Mohawk, Mic Mac, Abenaki and Verrill Canyon formations were then deposited along the margin of the basin. This section is overlain by a thick sequence of Early Cretaceous fluvial-deltaic strata of the Missisauga and Logan Canyon formations. The Late Cretaceous is represented by marine shales of the Dawson Canyon Formation. Strata of the latest Cretaceous and Paleogene transgression and subsequent Neogene regression belong to the Banquereau Formation. Two major structural features result with the development of the Scotian margin: syn-sedimentary, passive margin, listric faulting and deformation as a result of salt tectonics of the Argo salt (Fig. 3.2; Wade and MacLean, 1990).

3.2 Surficial Geology

The central Scotian Slope contrasts many other portions of the slope because of its largely intact Plio-Pleistocene stratigraphy (Mosher *et al.*, 1994). The study area is bounded on the west by the Acadia Valley system and on the east by the western margin

20
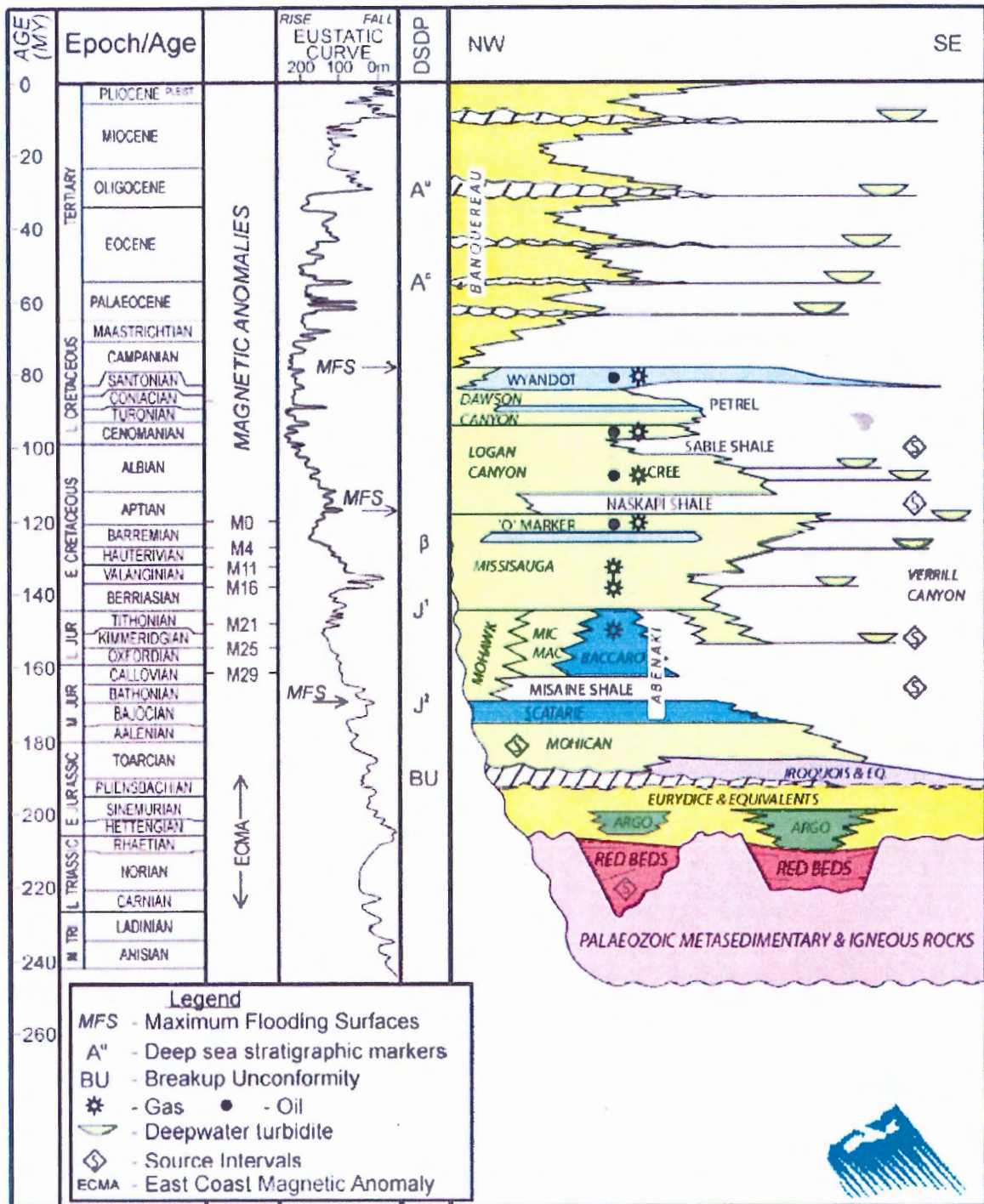
Figure 3.1: Generalized stratigraphic chart for the Scotian Basin (Kidston *et al.*, 2002; eustatic curve from Haq *et al.*, 1987).
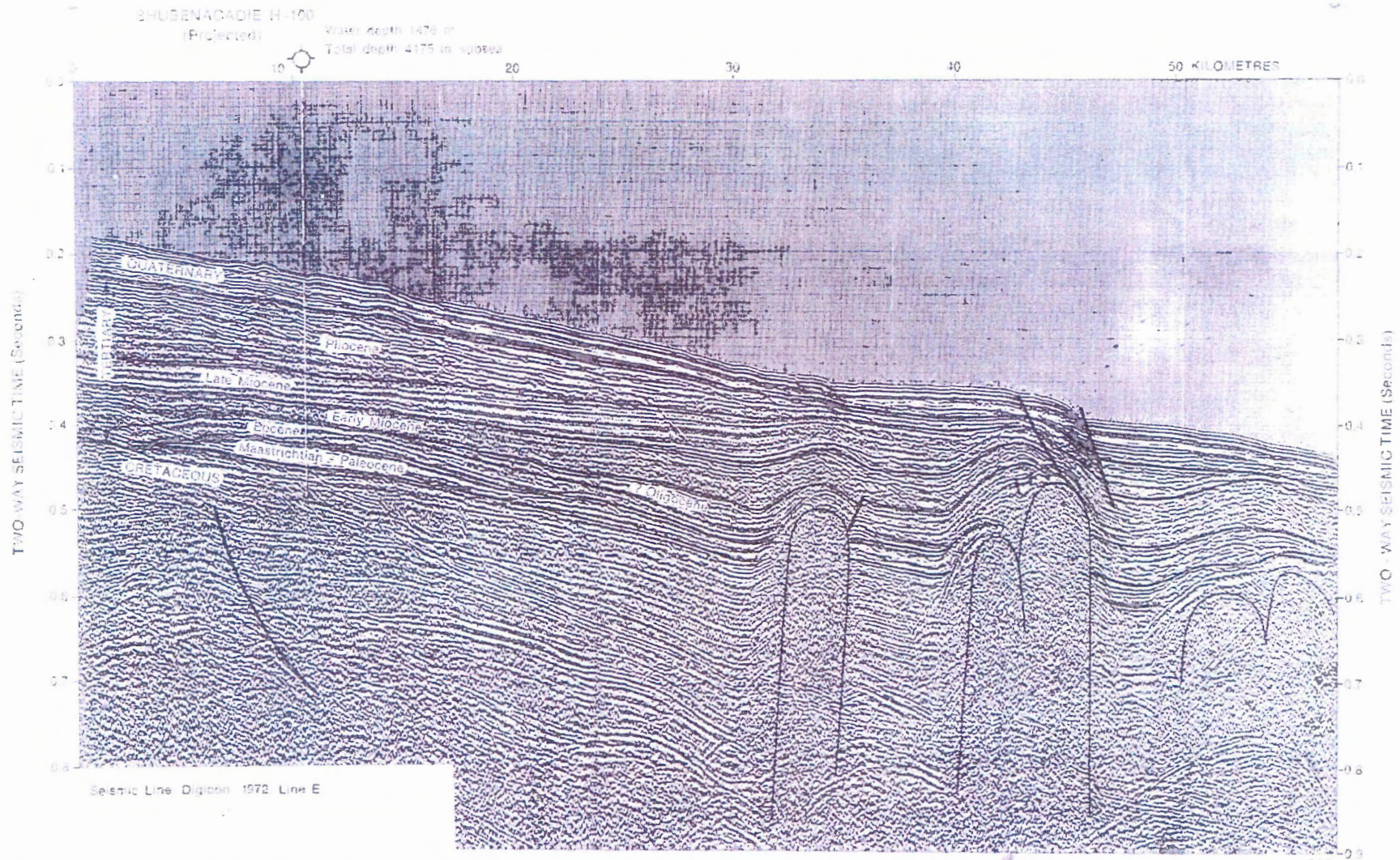
Figure 3.2: Industry seismic section from the central Scotian Slope near Shubenacadie H-100 showing subdivision of the Tertiary. Extensive deformation resulting from salt diapirism is present on the south end of section (Wade and MacLean, 1990). Line is located approximately 5 km west of line 2001-048A-32.

of Verrill Canyon where the slope is steeper and highly dissected by submarine canyons (Fig. 3.3a). Continental margin terminology is presented in Table 1. The slope gradient in the region varies from 3 degrees on the upper slope to 1.5 degrees on the lower slope (Fig. 3.3b; Mosher *et al.* 2001). The upper slope is relatively smooth. Wave-like bedforms are present in places at 180 to 250 metres below sea level (mbsl). Shallow gullies cut the seabed above the 300 m isobath. Relict iceburg pits and scours are observed between 300-550 mbsl, these features become muted with decreasing depth (Mosher *et al.*, 2001). Gullies head in water depths of 400 to 500 mbsl and terminate against semi-circular headscarps. The down-slope limit of till tongues regionally correspond to these head scarps (Gauley, 2001). Although the region is generally bathymetrically smooth, mass failure deposits are significant in the sedimentary column. Large, up to 300 m, pockmarks are visible in places. The lower slope hosts common linear scarps up to 100 m high. Domal anticlines are present over salt diapers on the lower slope.

Table 3.1: Terminology used to describe continental margins (Piper and Sparkes, 1987)

Terminology	Definition
Continental shelf	extends seaward from the coastline to an increase in slope between 80 and 130 mbsl
Continental slope	on the Scotian margin extends from the shelf break to a decrease of gradient at 2000 to 2500 mbsl
Upper slope	From shelf break to break in slope at canyon heads typically at 400-600 mbsl
Middle slope	From the line at canyon heads to a decrease in gradient typically at 1000 to 1400 mbsl
Lower slope	Zone between the middle slope and continental rise
Continental rise	Defined by a change in gradient to less than one degree
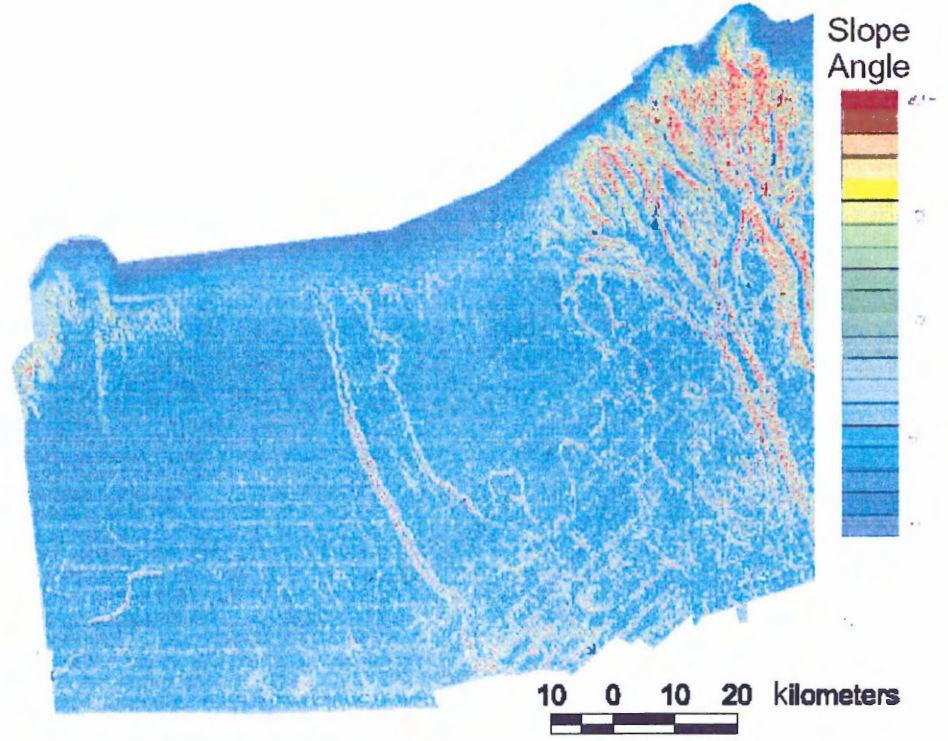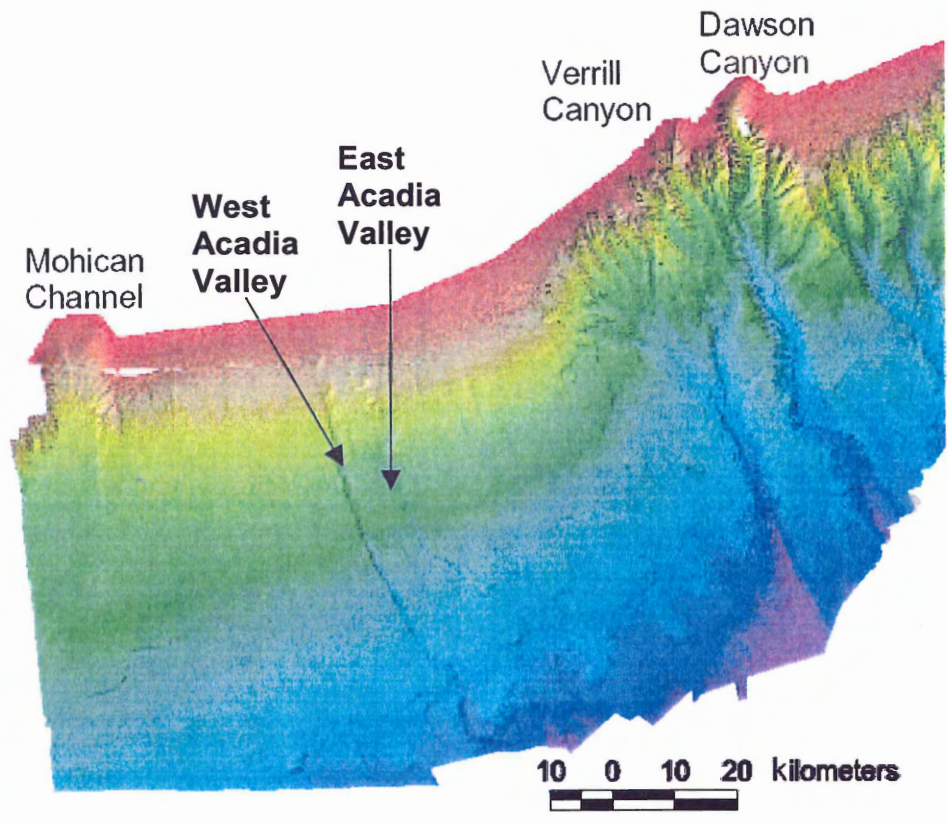
Figure 3.3: A) Seafloor surface render derived from multibeam bathymetric sonar data showing morphology of the study area (from Mosher *et al.*, in press). B) Slope angle map derived from multibeam sonar data of the study area (from Mosher *et al.*, in press).
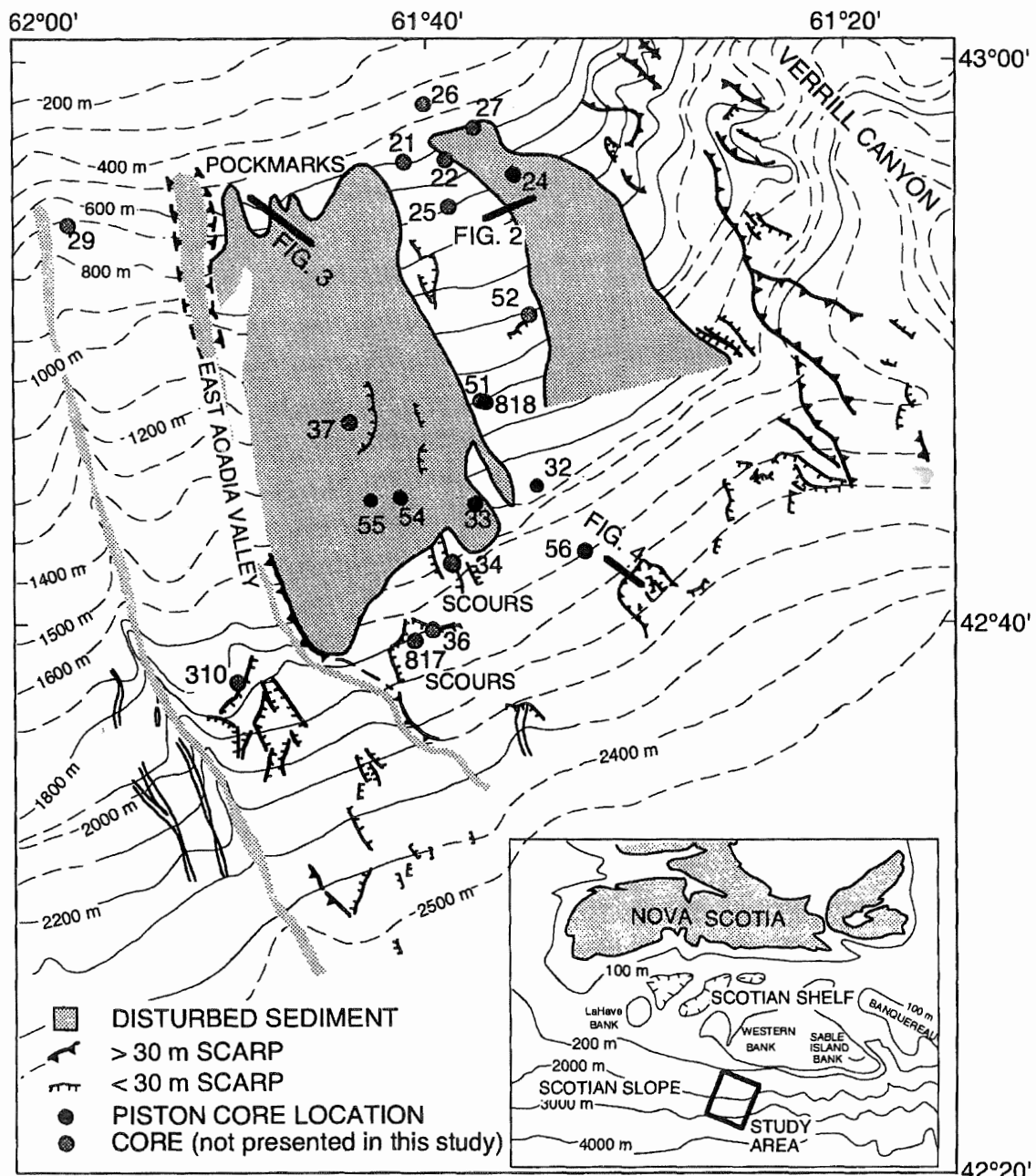
Figure 3.4: Bathymetric map of the study area, showing principal morphometric features (from Mosher *et al.*, 1994, after Piper *et al.* 1985).

The study area itself was divided into eastern and western disturbed zones based

on sidescan sonar studies (Fig. 3.4; Piper *et al.*, 1985). These zones are characterized by

rotational slumps and are abundant in 600-1000 m water depth. Pockmarks are also

abundant at this depth (Baltzer *et al.*, 1994). Bedding plane slides and larger slump scars

are common on the lower slope (Mosher *et al.*, 1994). Recently acquired multi-beam

data show that the largest failure escarpments developed in water depths of 2000 to 2500

m (Fig. 3.5). These arcuate escarpments are met upslope by numerous shallow sub-

parallel gullies that extend upslope to the limit of glacial till in about 500 m water depth.

Mosher *et al.* (1994) suggest that this deformation occurred 12,000 years BP coinciding

with the deglaciation of the shelf. The strata below some of these scarps show

demonstrable offset in high-resolution (sparker) profiles (Bennett, 2000). On the lower

slope and abyssal plain, downslope-trending gullies and valleys meander around domal

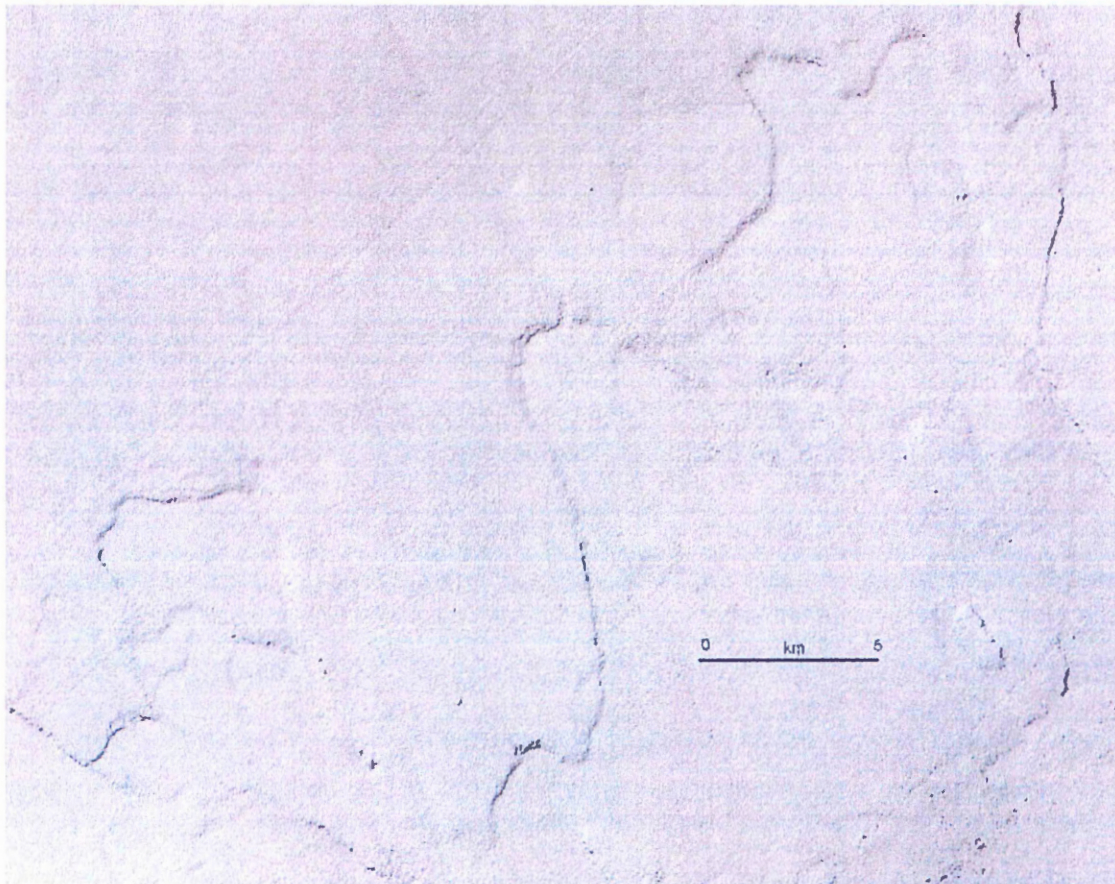structures and a complex pattern of surface escarpments surround them.

Figure 3.5: Detailed image of large arcuate failure found within the lower slope region of the study area (from Pickrill *et al.*, 2001).

3.3 Late Pliocene and Quaternary Stratigraphy

3.3.1 Lithostratigraphy

Late Pliocene and Quaternary lithostratigraphy is poorly understood within the study area. Samples are only available from piston cores and two hydrocarbon exploration wells with limited samples of the Quaternary section. Piper *et al.* (1987) examined the cuttings from Acadia K-62 and show the Pliocene section is composed of biogenic-rich mud corresponding to an accumulation of terrigenous muds mixed with pelagic detritus. These strata form part of the Banquereau Formation of the Scotian Shelf. The late Pliocene section (between red and gold horizons of Piper *et al.*, 1987) is marked by frequent thin sand beds, which are probably related to a decrease in sea level regression. No samples are available between the base of the Quaternary and near surface samples from piston cores.

Near surface sediments of the Scotian slope are well documented in literature, in part as a result of petroleum exploration. Mosher (1987) defines two formations: the uppermost Holocene formation which forms a 1-2 m drape over underlying sediments and a late Pleistocene formation. Mosher *et al.* (1994) believe the late Pleistocene formation was deposited by ice-margin processes. They identified five facies (Table 3.2) and determined that all facies with the exception of facies 1 were the result of mass flow deposition (Mosher *et al.*, 1994). The deposits generally occur on a scale finer than those observed acoustically, such that mapping facies by acoustic means or by correlation of piston cores is impossible. Bioturbated, silty clay and, rarely, thin bedded sand occur in close association, forming a 1-2 m thick unit at the top of most cores (Holocene section). This is consistent with slow rates of accumulation (on the order of <5 cm per year) and

27

implies that sediment processes are not strong enough to mobilize coarse sediment from the outer shelf and that ice rafting is minimal. Mosher *et al.* (1994) postulate that thinning and fining of beds of laminated silt and clay are fine-grained turbidites (Fig. 3.6). Sediment from piston cores demonstrate a variety of facies that represent fine-scale mass flow deposits, including turbidites and debrites that are associated with the late Pleistocene formation. Beds within the piston cores could not be correlated suggesting localized events. The presence of till on the outer Scotian shelf has been confirmed locally by core samples. West of the study area Hill *et al.* (1983) documented the presence of boulders on the upper slope apparently derived from till.

Table 3.2: Sedimentary facies described from piston core and their interpretations (Mosher *et al.*, 1994)

Facies	Description	Interpretation
1	Bioturbated, mottled silty clay	Comprises hemipelagic deposition of the Holocene formation, consistent with slow rates of accumulation (5 cm per 1000 years). Occurrences deeper in sedimentary section are believed to result from similar conditions.
2	Homogenous (sandy) silty clay	Comprises upper parts of turbidite unit
3	Laminated silt and clay	Typically greater than 1 m thick and fining upward occur in the Late Pleistocene Formation in association with Facies 2 and 5. Equivalent to fine-grained turbidites
4	Thin bedded sand	Comprises basal parts of turbidite unit
5	Silty clay with sand and gravel	Occur within late Pleistocene Formation, pebbly texture is characteristic of submarine debris flows (see Mosher *et al.*, 1994 for an extended explanation)

Two scales of mass flow processes are identified. Large-scale events are responsible for the two large areas of disturbed sediment, areas of erosional scour and bedding plane slides. The resolution of the piston core data does not allow the processes to be determined. Local, fine-scale mass-flow deposits may be related to ice-margin sedimentation (Mosher *et al.* 1989).

Large-scale slope failures occur within the acoustically defined disturbed zones. Deformed sediment is observed in cores. These areas are thought to represent areas of rotational slumping (Piper *et al.*, 1987).
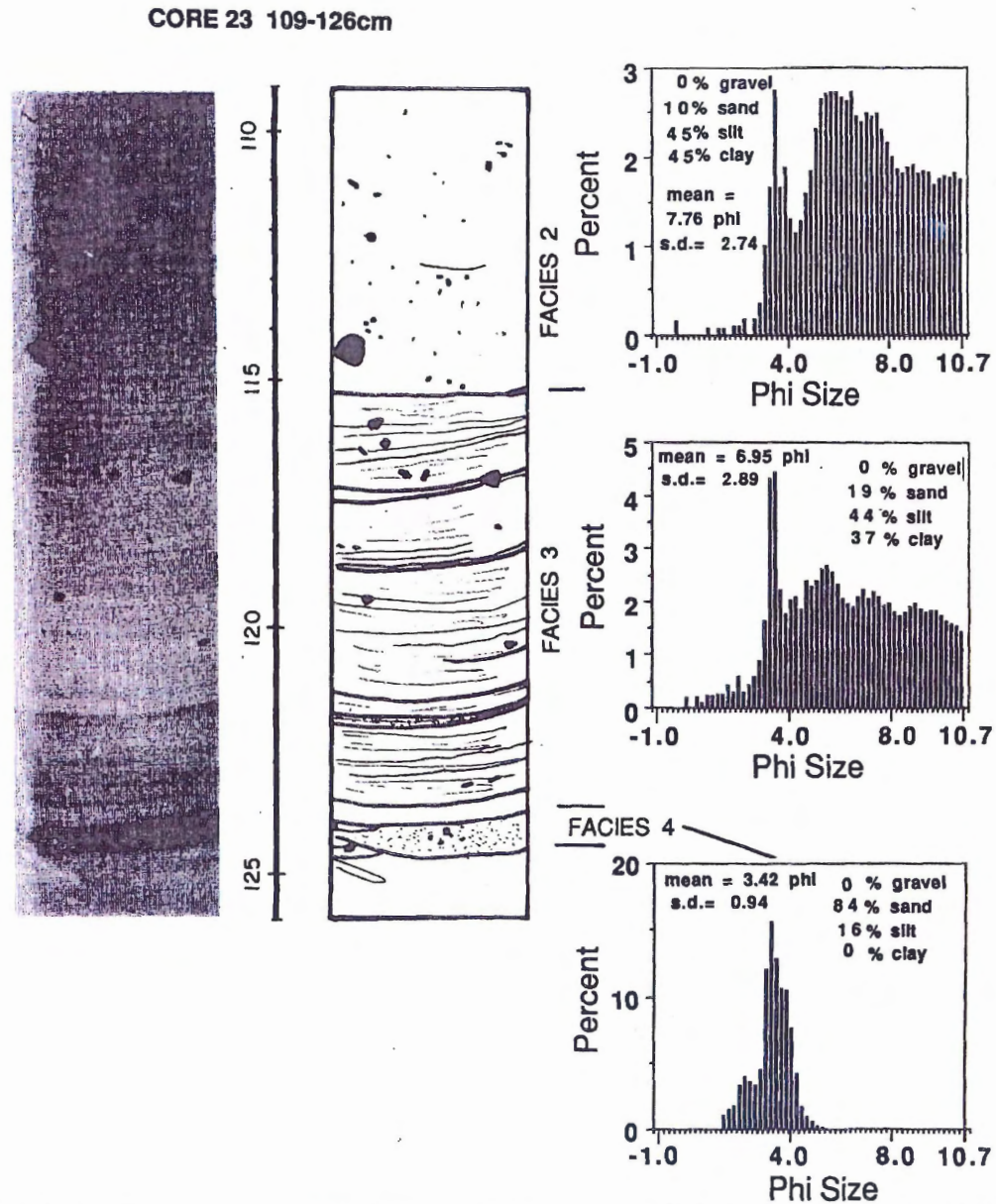

CORE 23 109-126cm

Figure 3.6: X-radiograph of a thin slab showing examples of Facies 2, Facies 3, and Facies 4 sediment, with grain size distribution curves. Facies 2 is structureless. Note the distinct laminations in Facies 3. Facies 3 passes gradationally upwards into Facies 2. Facies four is seen as a thin bed of fine sand. (from Mosher *et al.*, 1994)

3.3.2 Seismic Stratigraphy

Much of the established stratigraphic information for the Scotian slope is derived from seismic sections. The seismic stratigraphy within the study area was initially established by Piper *et al.* (1987) and revised by Piper and Normark (1990). Further work using higher resolution sparker data by Mosher *et al.* (1989) and Gauley (2001) are also of interest to this study.

No formal names have been applied to the late Pliocene and Quaternary strata and several naming schemes have been used in literature (Table 3.3). This study uses the nomenclature convention of Piper and Sparkes (1990), which has gained acceptance through Piper (2001).

The initial framework of the central Scotian Slope was established using 21 high-resolution multi-channel seismic sections supplemented by several high-resolution single channel seismic sections and multi-channel industry sections (Fig. 3.7; Piper *et al.*, 1987). The study focused on the development of Dawson and Verrill canyons; as a result most of the sections are located east of this study within Verrill Canyon.

The Oligocene facies (purple to dark green) is represented by two equally-spaced intervals of relatively continuous parallel to sub-parallel reflectors (Piper *et al.*, 1987). The Miocene interval (dark green to red) is similar in character to the Oligocene interval within the study area; however, the package thins to the east. Erosion of the light green to red unit marks the development of the ancestral Dawson Canyon (Fig. 3.8). The ancestral channel is draped by acoustically transparent sediment below red and provides an age constraint for the channel development as mid to late Pliocene, correlating to a sea level lowstand (Fig. 3.9).

30

Table 3.3: Neogene and Quaternary nomenclature used in the study area. This study uses the scheme of Piper and Sparkes (1990).

Piper and Sparkes, 1990	Regional Reflector (Piper and Normark, 1989)	Mosher et al. 1989	Piper et al., 1987	Probable age (Piper, 2001)
Light Red	A	I		
Light Yellow		II		
Brown		III		
Carmine	B	IV	Yellow	Middle Pleistocene (0.45 Ma)
Gold (flesh)			Gold	
Rose		V		
Grey	C	VI		Basal Pleistocene (1.6 Ma)
Magenta				
Blue			Blue	
Red	D		Red	
Lavender	E		Light Green	Middle Pliocene
Orange				
Pink				Basal Pliocene
Canary	F		Dark Green	Early Miocene (deep water); Miocene/Eocene unconformity (shallow water)
			Purple	Oligocene
			Pink	Late Cretaceous

The red to blue interval onlaps the western edge of the valley and is of variable thickness (Fig. 3.8), thinning slightly upslope west of the ancestral channel. Within the channel, the red horizon is characterized by short discontinuous reflections that alternately become more continuous. On the upper slope west of the ancestral channel, the unit shows an alternation of low mounds with divergent sub-parallel reflections and small depressions with short discontinuous reflections. The red to blue interval consists of continuous parallel reflectors on the lower slope west of the channel.
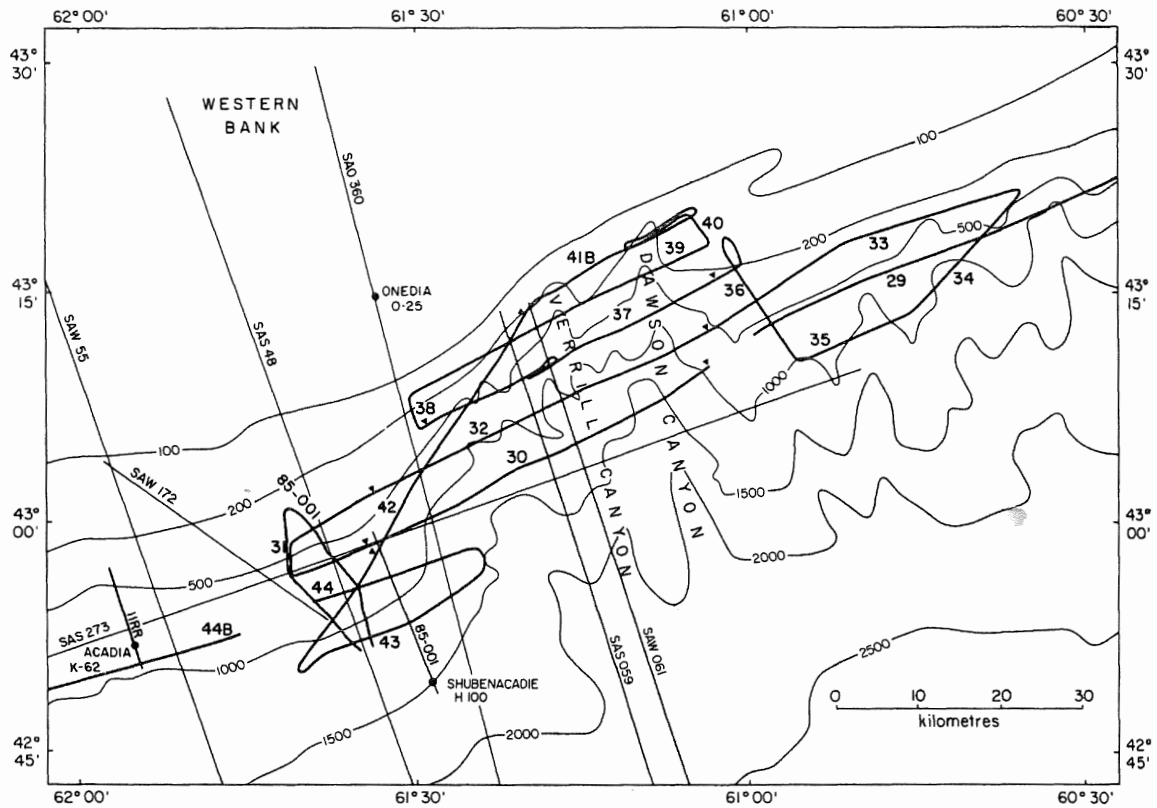
Figure 3.7: Location of seismic profiles used by Piper *et al.* (1987). Lines 29 to 44 and 11RR are high-resolution multi-channel seismic profiles. The SA series of lines are industry low frequency multi-channel sections, and line 85-001 is a single channel high-resolution profile.

The blue to gold interval is described west of Verrill Canyon as consisting of parallel or slightly divergent reflections that drape pre-existing bathymetry. The unit thins downslope and towards the margin of Verrill Canyon. The interval from red to gold infills much of the ancestral channel. Two intervals of gully cutting are recognized on the slope west of Verrill Canyon. The older episode occurs at blue and is only recognizable on the upper slope, whereas the younger episode (just below gold) is widespread. Piper *et al.* (1987) suggests that this gully cutting is the result of sea level lowstands.
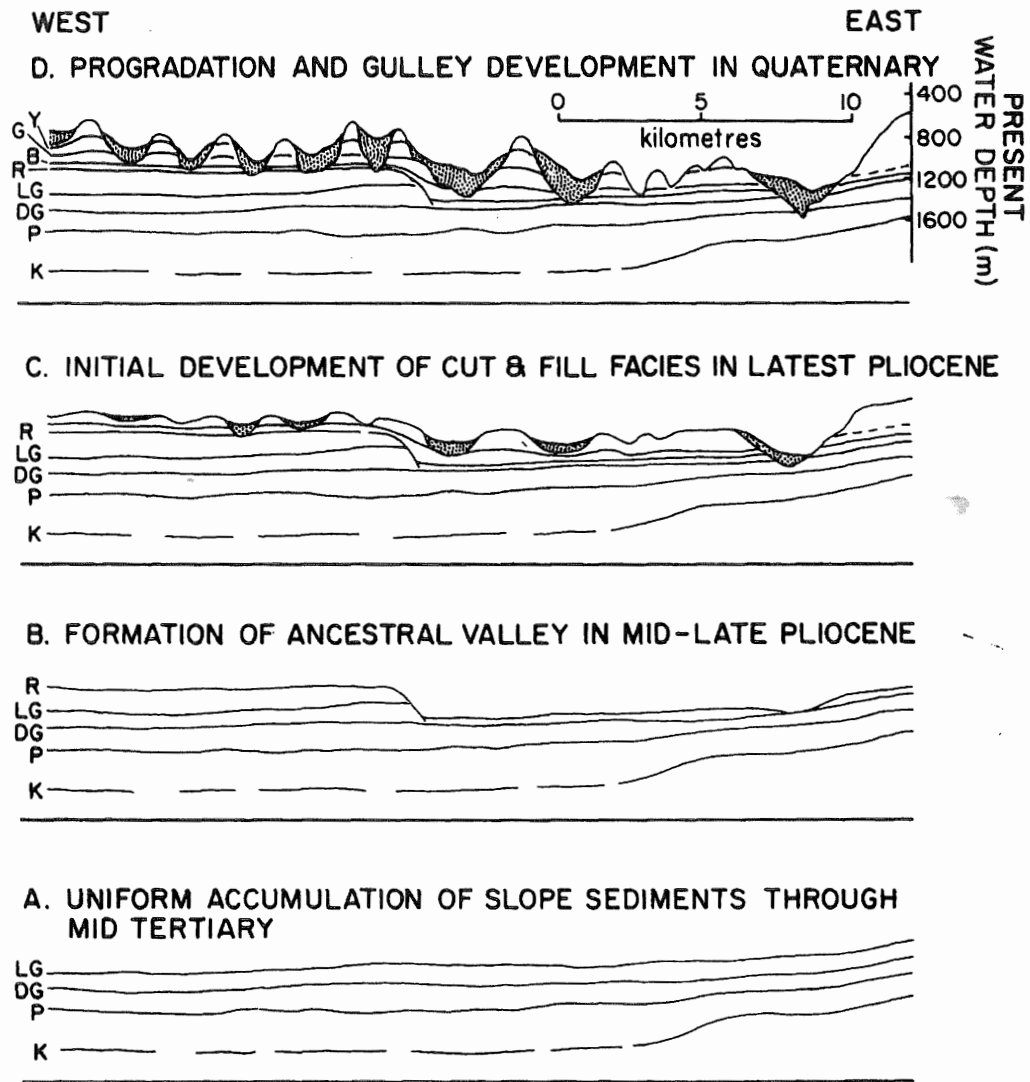
32

WEST   EAST

D. PROGRADATION AND GULLEY DEVELOPMENT IN QUATERNARY

0   5   10

kilometres

PRESENT WATER DEPTH (m)

400
800
1200
1600

G
Y
B
R
LG
DG
P
K

C. INITIAL DEVELOPMENT OF CUT & FILL FACIES IN LATEST PLIOCENE

R
LG
DG
P
K

B. FORMATION OF ANCESTRAL VALLEY IN MID-LATE PLIOCENE

R
LG
DG
P
K

A. UNIFORM ACCUMULATION OF SLOPE SEDIMENTS THROUGH MID TERTIARY

LG
DG
P
K

Figure 3.8: Schematic strike sections showing evolution of the Late Cenozoic sedimentary sequence. A: Uniform accumulation of slope sediments through mid-Tertiary. B: Formation of ancestral Valley in mid- to Late Pliocene. C: Initial development of cut and fill facies in Late Pliocene. D: Progradation and gully development in Quaternary. Study area is located in western half of section (From Piper at al., 1987)

The sequence above gold forms a drape over existing topography, but is difficult to correlate on the western margin of the ancestral channel because of erosion. The unit above yellow shows similar character. In the northern part of the study area the yellow horizon comprises irregular short discontinuous reflections that become a continuous coherent reflection in deeper water. This sequence above yellow thickens upslope and

33

interfingers with wedges of unstratified sediment with irregular upper surfaces,
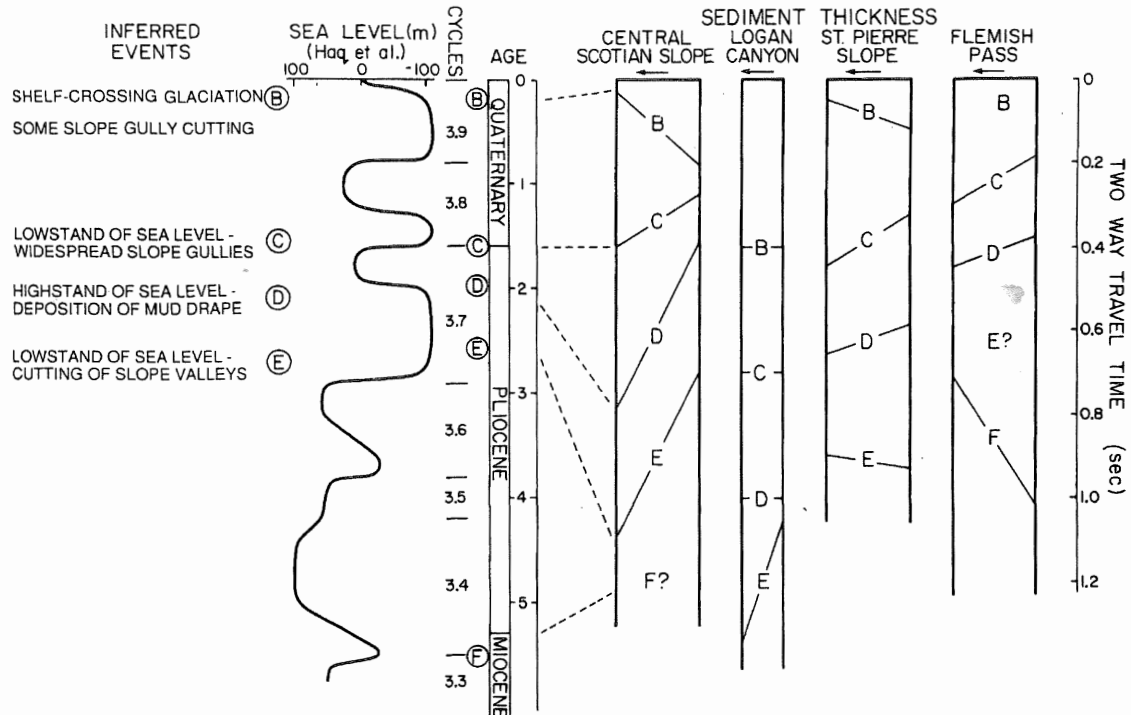
interpreted as till tongues.

Figure 3.9: Summary of thickness variations between key reflectors B to F (assumed to be correlated time horizons and tentatively dated in the age column) in progradational areas on the central Scotian Slope, Logan Canyon area, St. Pierre Slope and western flank of Flemish Pass (arrows indicate downslope direction). Figure also shows correlation with Haq *et al.* (1987) sea-level curves and synthesis of principal inferred events controlling deposition. (From Piper and Normark, 1989)

CHAPTER 4

RESULTS

4.1 Key Reflectors

Nine reflectors of the Piper and Sparkes (1990) seismic stratigraphic scheme were identified and correlated throughout the study area (Fig. 4.1). The oldest reflector identified is red followed by blue, magenta, grey, rose, flesh, carmine, brown, and light red.

4.2 Seismic Facies

Six seismic facies have been identified within the study area (Fig. 4.2). Facies 1 (Fig. 4.2a, 4.2b) is composed of high-amplitude, continuous parallel reflections. This facies generally overlies Facies 2, which is identified by its acoustically transparent (incoherent) character. Facies 2 contains low amplitude parallel reflectors, but it is difficult to determine whether these are reverberations within the strata, or real reflectors. Facies 3 is composed of low amplitude, somewhat chaotic reflections capped by a continuous, high-amplitude horizon (Fig. 4.2c). Facies 3 is typically mounded in strike sections. Facies 4 is composed of moderate amplitude, highly chaotic and discontinuous reflections (Fig. 4.2d) and is restricted to the upper slope. Facies 5 is composed of highly chaotic, low-amplitude reflections capped by a by an interval of moderately chaotic, high amplitude, laterally continuous reflections (Fig. 4.2e). Facies 6 is similar to Facies 1 and 2 except reflections are hummocky and somewhat discontinuous (Fig. 4.2f).
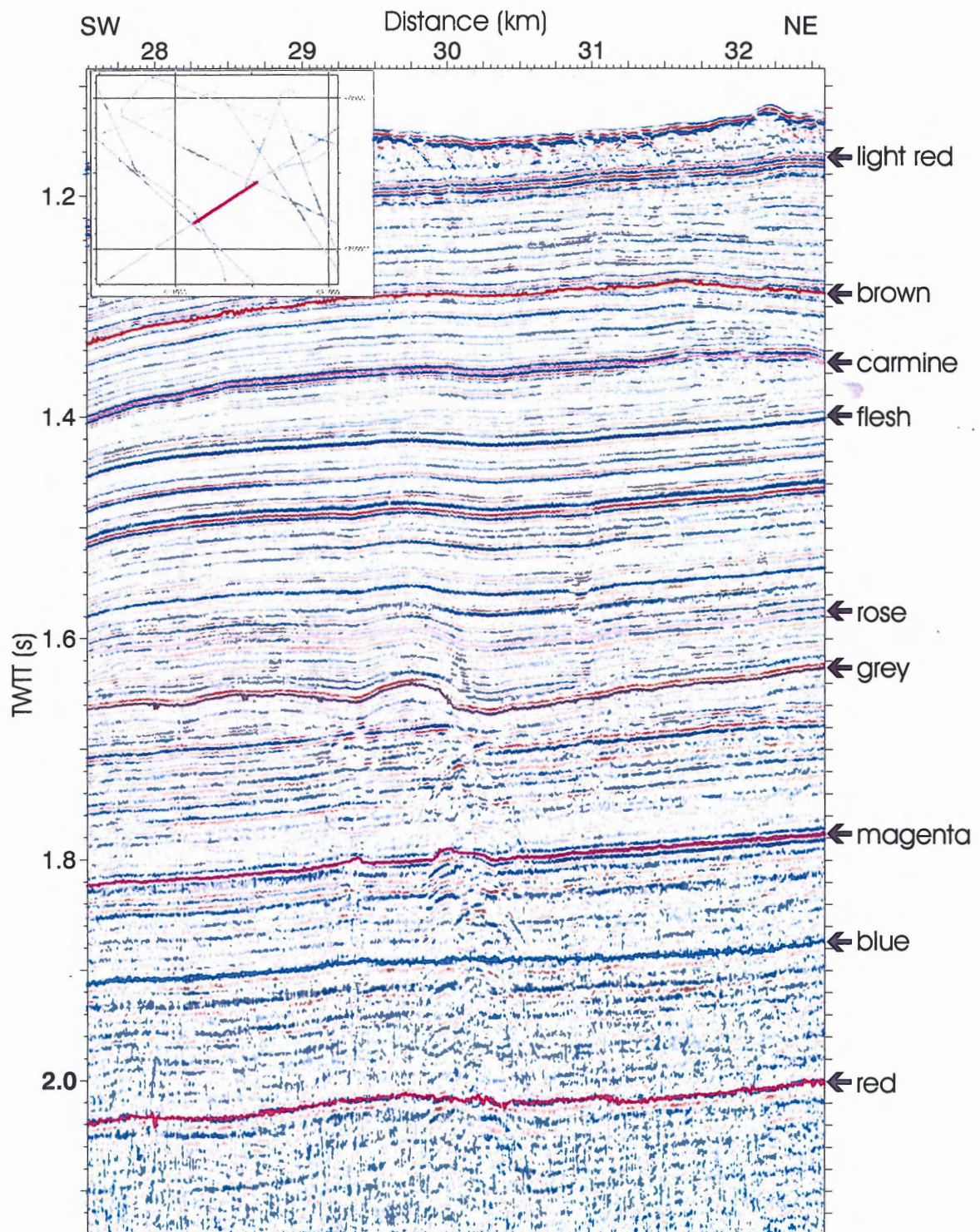
Figure 4.1: Strike section on the upper slope showing nine key reflectors correlated throughout the study area. This segment forms part of line 2001-048-29, which overlies type section 81044-44 of Piper and Sparkes (1990). Inset map for location.
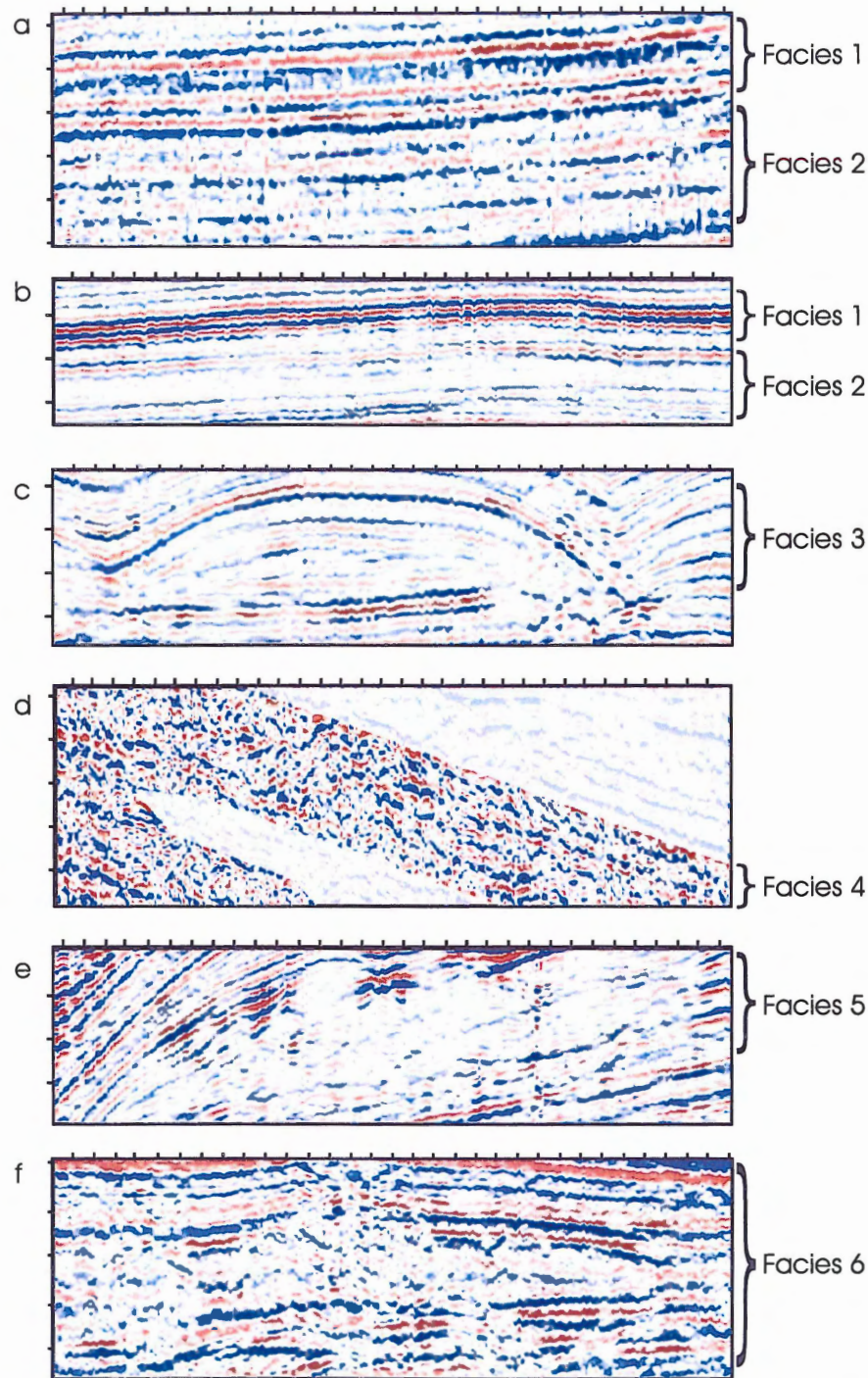
Figure 4.2: Six seismic facies identified within the study area from high-resolution airgun seismic. Facies 1 is composed of high-amplitude continuous reflectors. Facies 2 is composed of low amplitude continuous to somewhat discontinuous reflectors. Figures A and B contrast facies one and two in the deep subsurface and shallow subsurface respectively. Facies 3 (Figure C) is composed of internally low amplitude, discontinuous reflectors capped by a continuous high amplitude horizon that typically shows varied relief. Facies 4 (Figure d) is composed of highly chaotic, high amplitude reflectors. Facies 5 (Figure E) is composed of highly chaotic low amplitude reflectors capped by an interval of moderately chaotic, high amplitude reflectors. Facies 6 (Figure f) is similar to facies one and two except that reflectors are hummocky and somewhat discontinuous. All figures have the same scale; each vertical increment represents 20 ms TWTT, and each horizontal increment represents 50 m.

37

4.3 Velocity Model

Compressional wave velocity data from multi-sensor track and discrete measurements of piston cores reveals that velocities within the upper few metres of strata are on average 1500 m/s (Gauley, 2001).

Between the maximum penetration of piston cores and the top of the borehole measurements, there is very little velocity data and no physical samples with which to determine interval velocities. An ocean bottom seismometer (OBS) station provides velocity information within this interval, as do velocity picks from multi-channel seismic data of cruise 81044. OBS data of LeBlanc (2002) (Fig. 4.3) suggests there is a strong gradient in the first 200 m of sediment followed by a lower velocity gradient beneath. The higher velocity layer corresponds to the carmine horizon. LeBlanc argues that this sudden velocity increase may be related to the presence of a gas hydrate zone, but there are no collaborative data to confirm this hypothesis. The OBS-derived velocity gradient shows no low velocity layer below the high velocity layer, which is characteristic of gas hydrate zones (Yuan *et al.*, 1996). As a result, the preferred interpretation of the velocity profile is that it is strictly lithologically controlled.

Stacking velocities of high-resolution multi-channel lines were also analyzed. The lines were apparently processed three times, first in 1982 by Geophysical Services Incorporated (GSI), then in 1984 by GSI, and finally by Seiscom Delta in 1986.
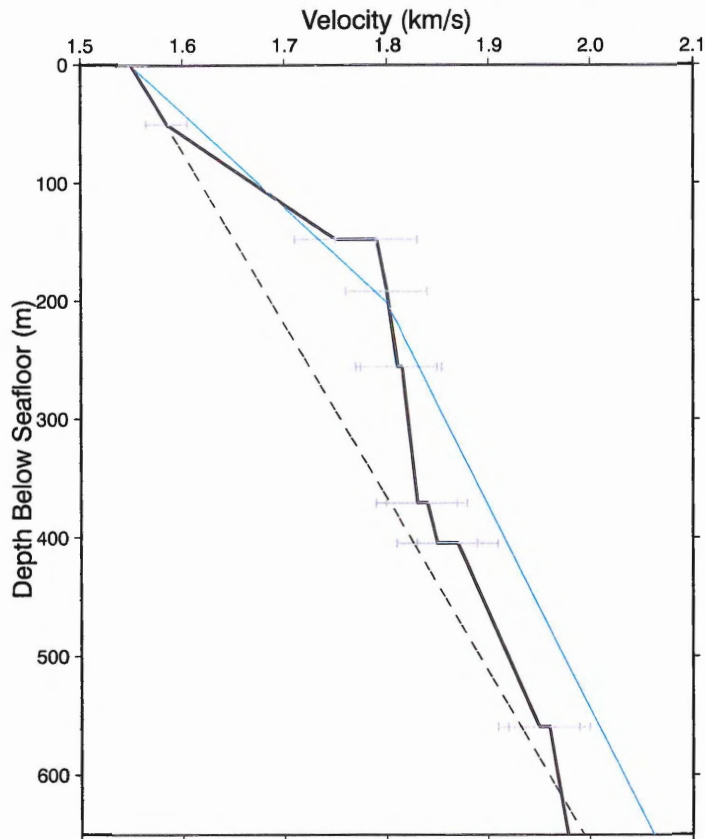
Figure 4.3: Plot of velocity vs. depth (below sea level) from the OBS reflection model of LeBlanc (2002). The blue line is refraction data, the solid line (with error bars) is reflection data, and the dashed line is the regional trend.

Stacking velocities from the Seiscom Delta analyses do not appear to correspond to velocities achieved by other methods for the uppermost section. Many of the semblance CDPs from these lines use a seafloor velocity of 1450 m/s but interval velocities selected at 50 to 75 ms below the seafloor are typically 3000 to 3500 m/s. Root-mean squared (RMS) velocities have been selected at 1550 m/s for the first semblance pick below the seafloor. This defined jump in RMS velocity over a small travel time results in a large interval velocity for the shallow section. At 150 ms below seafloor the stacking velocities become more reasonable and average approximately 2100 m/s.

The 1984 GSI lines have velocity analyses every three kilometres and the GSI 1982 lines have one semblance CDP per line published. Stacking velocities for this line show velocities in the range of 1490 to 1550 for the seafloor and show an increase to 1680 m/s at 175 ms. Below 175 ms, the velocity trend appears to increase linearly with depth. The GSI velocities appear to be much lower than those obtained from the OBS reflection data.

Velocity logs from the Acadia K-62 well show that velocities between 370 and 800 ms below seafloor vary from 1550 m/s to 1925 m/s with an average of 1675 m/s. These velocities are lower than the reflection OBS data.

All of the velocity data are located on the upper slope, and it is unclear how the velocity profile will change with increasing water depth coincident with reduced sediment accumulation rates downslope. Therefore seismic data are presented in two-way travel time values, as opposed to depth values, because of poor velocity control.

4.4 Seismic Units

Nine seismic intervals are derived from the key reflectors. Time interval isochron maps for the intervals are found in Appendix B. All intervals are referred by their bounding surfaces; that is, the red-blue interval refers to the interval between the red and blue reflectors.

4.4.1 Red-blue Interval

The red-blue interval is poorly imaged in the high-resolution data sets because of its depth of burial. On the mid- to upper slope, the basal interval is composed of low amplitude incoherent reflectors of Facies 2 and the upper interval composed of high-amplitude continuous reflectors Facies 1. The red-blue interval is marked by numerous faults that are identifiable in both strike and dip sections. These faults are described in section 4.5.

The red-blue interval thins downslope; from 120 ms to 10 ms (Fig. B1). Much of this thinning occurs in water depths of 2.5 to 2.65 seconds over 5 km distance downslope. Within the upper and mid-slope region, westward thinning of the interval takes place; the interval attains thicknesses of 140 ms near Verrill Canyon and thins to 110 ms in the East Acadia Valley. The red-blue interval is absent in the eastern limit of the study area, on the western edge of Verrill Canyon. The interval cannot be correlated accurately across a region of significant salt deformation on the lower slope (Figs. C1, C2). In this area the reflection character of the interval changes to Facies 6. The red-blue interval appears to drape topography of the red horizon.

4.4.2 Blue-magenta Interval

The blue-magenta interval is imaged throughout most of the survey lines (Fig. A2 and A3) and is similar to the red-blue interval in that the base of the interval is represented by Facies 2 and the top of the interval is represented by Facies 1. The blue-magenta interval also drapes topography at the blue reflector. The blue-magenta interval thins downslope from 110 ms to 15 ms and exhibits rapid thinning over the same region

as red-blue (Fig. B2). The blue-magenta interval also shows similar west to east thinning (from 110 to 90 ms) on the upper and mid-slope region of the study area. The blue-magenta interval is also absent in the easternmost region of the study area. Immediately north of the salt dome on the south end of line 2001-048A-34 the interval thickens from 35 ms to 70 ms, in contrast to the gradual downslope thinning observed on line 2001-048A-32. The interval cannot be correlated accurately across a region of significant salt deformation on the lower slope, and in this area the seismic character of the sequence shifts to Facies 6.

4.4.3 Magenta-grey Interval

The magenta-grey interval consists of three vertically stacked facies. The lowermost portion is represented by Facies 2 and is draped by Facies 1. Facies 1 has a locally irregular upper surface and is capped by Facies 3. On the upper to mid-slope, Facies 1 is eroded approximately 10 ms, but in some channels erosion is up to 45 ms. Facies 1 is absent in areas of the mid- to lower slope representing approximately 40 ms of eroded strata. The top of the unit is bounded by a continuous, high-amplitude reflection. Numerous channels dissect Facies 3.

Thickness of the magenta-grey interval isochron is variable (Fig. B3). It thins downslope from 175 ms on the upper slope to 50 ms at the base of the slope with significant thinning (35 ms) at the southern region of the study area north of salt dome structures. The interval thins rapidly to 70 ms on the western flank of Verrill Canyon, but is not truncated on the flanks of the canyon compared to the interval from red to magenta. The magenta-grey section also shows thinning in the East Acadia Valley and on the upper

42

slope in the far western region of the study area, but thickens in the West Acadia Valley. The interval cannot be correlated accurately through the region of salt deformation on the lower slope.

4.4.4 Grey-rose Interval

The grey-rose interval is composed of two seismic facies in sequence; a basal sequence of Facies 2 capped by an interval of Facies 1. The character of Facies 2 in this case varies from the definition in that it has more pronounced low amplitude reflections. Facies 1 is also significantly thinner than underlying intervals (20 ms). The pattern of isochron thickness for grey-rose is distinctly different from previous isochrons (Fig. B4). Grey-rose shows little to no downslope thinning with a pronounced thick area (130 ms) in the western portion of the study area. The interval thins to 15 ms into the Acadia Valley system where the top of the interval is truncated. This interval also shows thinning over both of the prominent salt dome features near the base-of-slope. On the lower slope, south of the salt dome the interval shows Facies 6 development. The reflectors through this interval drape the irregular topography at grey.

4.4.5 Rose-flesh Interval

The rose-flesh interval is composed of four intervals of Facies 2 / Facies 1 sequences. The two lower sequences comprise two thirds of the interval thickness; each sequence is approximately 50 ms on the mid-slope. Similar to the grey-rose interval, these sequences have few high-amplitude reflectors in Facies 1. The upper two sequences

43

are approximately 30 ms thick. These reflectors drape the rose surface and there is no infilling of its topography.

The rose-flesh interval thins downslope from 200 ms to 70 ms (Fig. B5). Much of this thinning takes place on the lower slope where strata are truncated by erosion. The interval is also truncated at the edge of the Acadia Valley. This truncation is parallel to the shelf-edge north of the Acadia K-62 exploration well and deflects downslope east of the exploration well. The rose-flesh interval shows complex erosional features on the margin of Verrill Canyon. Thinning over both of the salt dome features is evident and there is a shift towards Facies 6 beyond the salt domes.

4.4.6 Flesh-carmine Interval

The flesh-carmine interval contains a Facies 2 / Facies 1 sequence in the central and eastern part of the study area and is entirely Facies 5 in the western portion of the study area. The Facies 2 interval is similar to underlying intervals except that it fills remnant topography from the magenta-grey interval. Mounds (40 ms on the upper slope) are consistently located to the west of the ponded sediment.

The flesh-carmine interval thins moderately downslope from 75 ms at the upper slope to 45 ms on the lower slope (Fig. B6). Much of this thinning occurs on the upper slope. The interval thins to 30 ms in the east Acadia Valley and is absent on the lower slope. It thickens into the West Acadia Valley where it is 95 ms on the upper slope and 70 ms on the mid-slope. In this area of thickening the interval is entirely composed of Facies 5. The interval is absent in the eastern region of the study area on the mid- to lower slope.

4.4.7 Carmine-brown Interval

The carmine-brown interval is composed of at least two and possibly three Facies 2 to 1 sequences. Evidence of these sequences is seen in the western portion of the study area in the valley adjacent to Verrill Canyon. The lower sequence thins eastward from 30 ms to 12 ms on the mid-slope and reflectors associated with this event thin and blend in with Facies 2 of the middle interval. The middle and upper sequences are very thin, both approximately 20 ms thick on the mid-slope. Upslope, these strata interfinger with wedges of Facies 4 strata (Fig. 4.4).

The carmine-brown interval shows moderate downslope thinning from 70 ms to 0 ms thickness (Fig. B7). The entire interval is truncated on the lower slope in the central portion of the study area. In the western region, this escarpment re-establishes on the mid-slope south of Acadia K-62 exploration well. The interval shows significant thickening east of line 2001-048A-32 where it fills a large topographic low. Further east, the interval is eroded. The upper sequence of the interval is eroded locally on the mid to lower slope.

4.4.8 Brown-light red Interval

On the upper slope, the base of the brown-light red interval is composed of a 32 ms thick Facies 1 bed overlain by four Facies 2 / Facies 1 sequences. The basal three sequences are all approximately 20 ms thick and the upper sequence is approximately

45
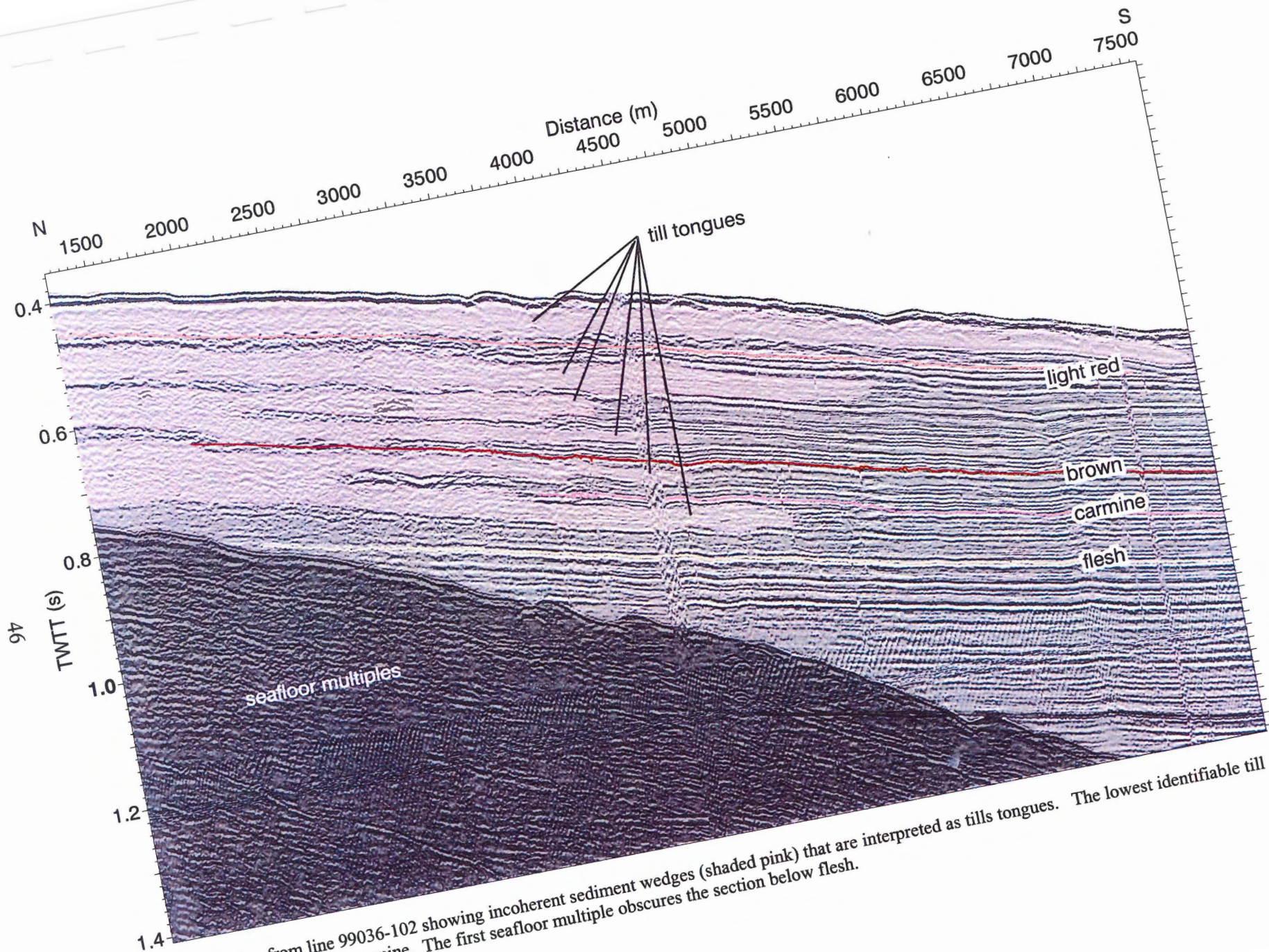
Figure 4.4: Section from line 99036-102 showing incoherent sediment wedges (shaded pink) that are interpreted as tills tongues. The lowest identifiable till tongue lies immediately below carmine. The first seafloor multiple obscures the section below flesh.

70 ms thick on the upper slope. These sequences thin rapidly downslope and become nearly indistinguishable as the basal three sequences thin to 10 ms. The fourth sequence thins to 34 ms on the midslope. On the upper slope the interval interfingers with Facies 4 strata (Fig. 4.4). The brown to light red interval shows rapid downslope thinning on the upper slope. On the mid- to lower slope there is little or no thinning.

4.4.9 Light red-seafloor Interval

The light red to seafloor interval is composed of a Facies 2 to Facies 1 sequence. On the upper slope these strata are somewhat contorted and Facies 2 changes into Facies 4 moving upslope. The interval shows downslope thinning from 100 ms on the upper slope to 25 ms on the mid-slope. Up to 10 ms of strata within the upper portion of the light red-seafloor interval are eroded in two large areas of the upper and mid- slope.

4.5 Faults

Two types of faults are notable within the study area. Type 1 faulting (Figs. 4.5, 4.6) is only observed in the red-blue interval and restricted to the upper and mid- slope regions. Some faults appear to displace strata up to magenta, but it is difficult to discern whether this is sedimentary drape of lower relief or offset sediment beds. Type 1 faults show an average displacement of 20 ms; however, observable displacement ranges from 5 ms to 30 ms. Offset of blue and red reflectors appears to be approximately the same. When examined without scale exaggeration the faults appear to be near vertical. The motion along these faults is somewhat variable in strike sections, but in dip sections they are normal displacement faults.

47
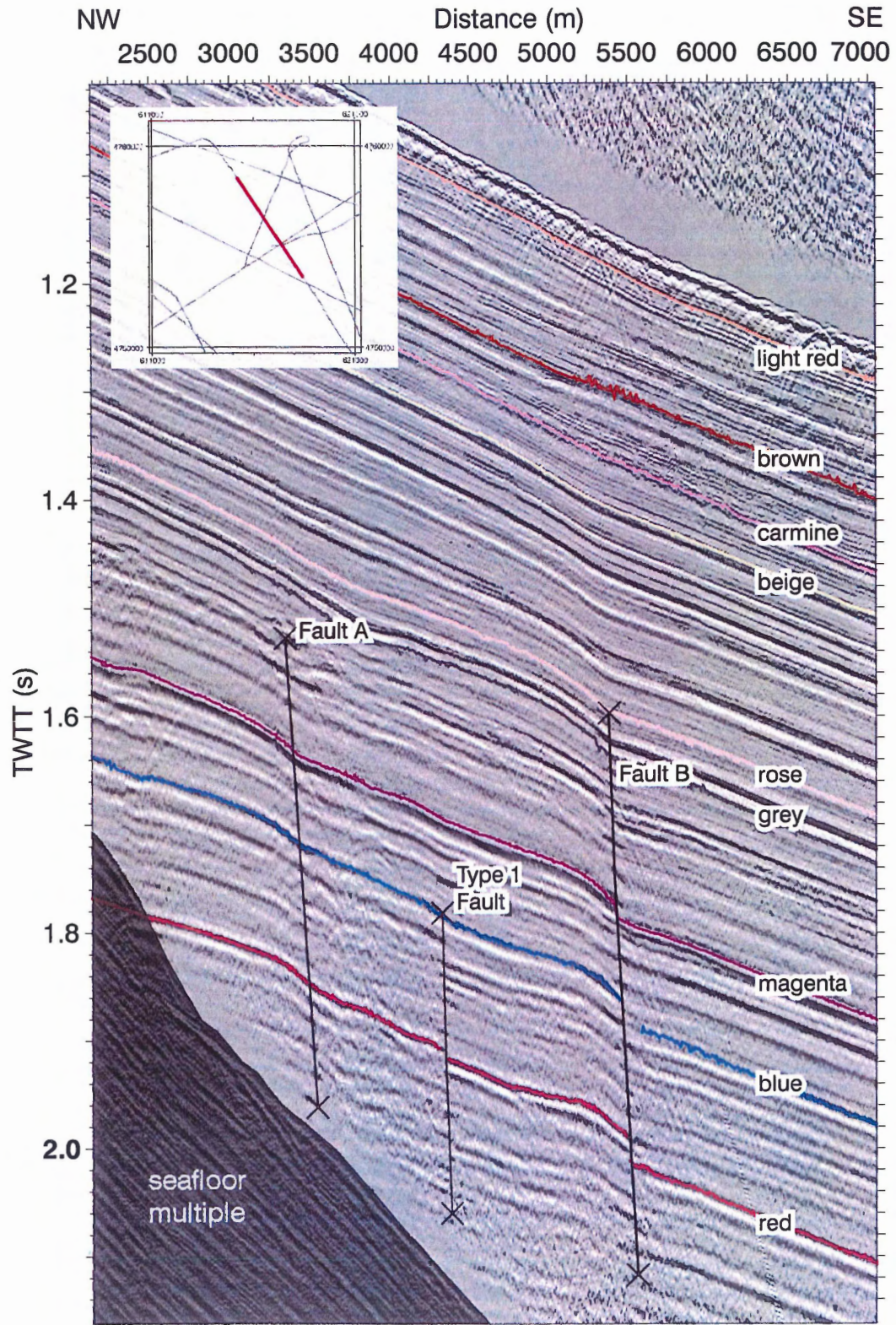
Figure 4.5: Part of line 2002-048A-32 showing three normal faults (black lines). From north to south these are Fault A, a Type 1 fault, and Fault B. Inset map indicates position of seismic section.
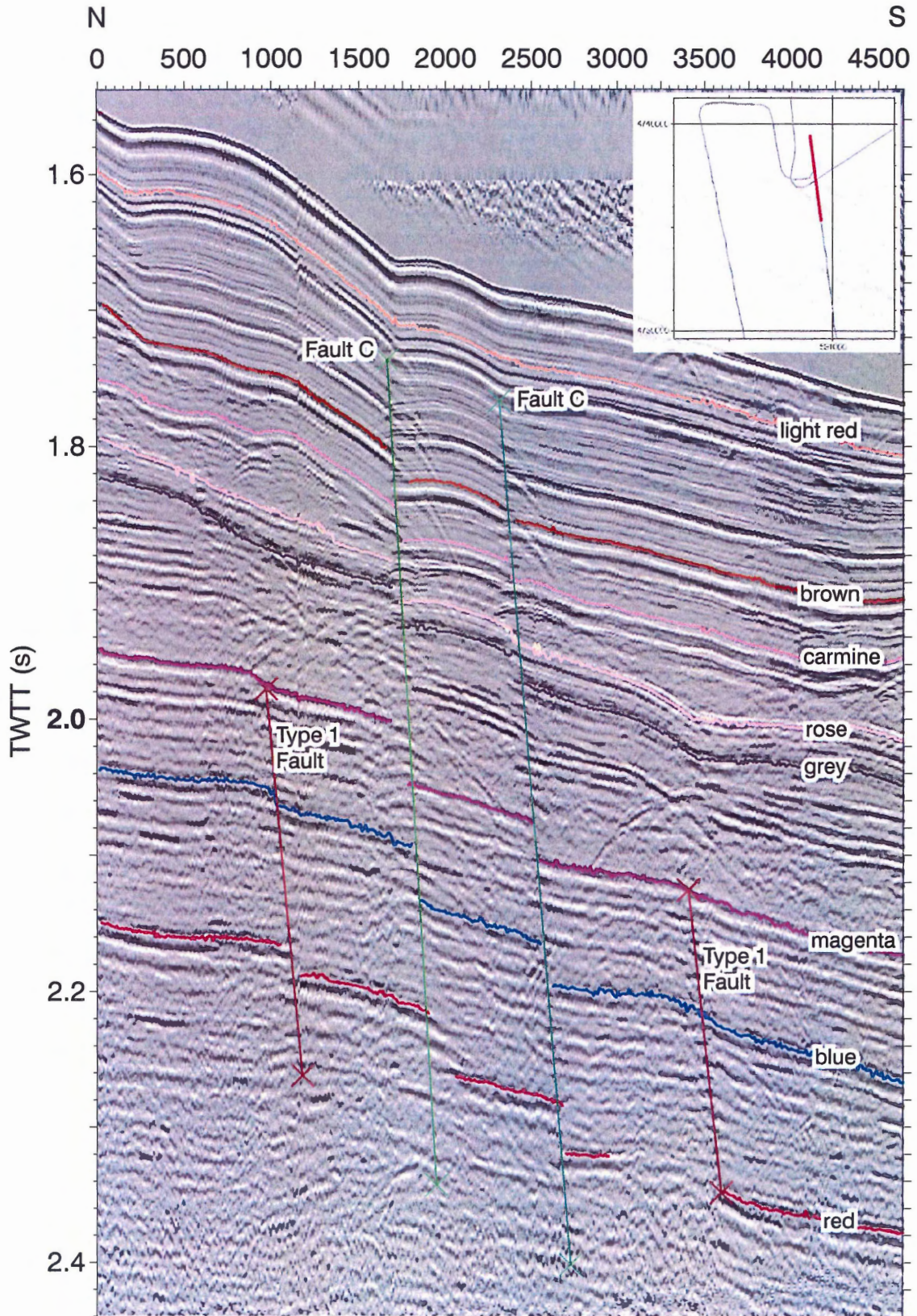
Figure 4.6: Portion of line 99036-111 showing two Type 1 faults (red) and two faults that form Fault C (green). Inset map shows location of section.

Four Type 2 faults are identified (Fault, A, B, C, D from north to south). These faults are correlated on the plan view interpretation maps (Appendix C). All of the faults are parallel to the shelf. Displacement is varied along some of the faults.

The northernmost fault (Fault A; Fig. 4.5) is a listric, normal fault verging basinward. The red-blue, blue-magenta, and magenta-grey intervals show minor upslope thinning on the footwall and thickens over the downslope hanging wall suggesting it may have been active during the entire red to grey time interval. Fault A shows only minor displacement, with a maximum of 10 to 15 ms within the red-blue interval.

Fault B (Fig. 4.5) is a normal and basinward verging fault that shows displacement through to rose. This displacement isindicated by upslope thinning and downslope thickening within the red-blue, blue-magenta, magenta-grey, and grey-rose intervals. It is difficult to determine whether strata above rose are faulted or draped over the fault topography. This fault was primarily active between the deposition of magenta-grey and shows 40 ms of displacement (line 2001-048A-32; see Fig. 1.2 for line locations) through the interval. Displacement decreases westward; 1.5 km west (line 2000-042-72) displacement is 17 ms.

Fault C (Fig. 4.6) is a combination of at least two, normal, basinward verging faults approximately 500 m apart. The faults appear to have been active between grey-magenta and during the brown-light red interval based on upslope thinning and downslope thickening. The fault may also have been active recently, but it is difficult to determine whether strata above light red drape fault topography or are offset by faulting. Fault C shows maximum displacement of 105 ms up to the magenta interval on line 99036-111.
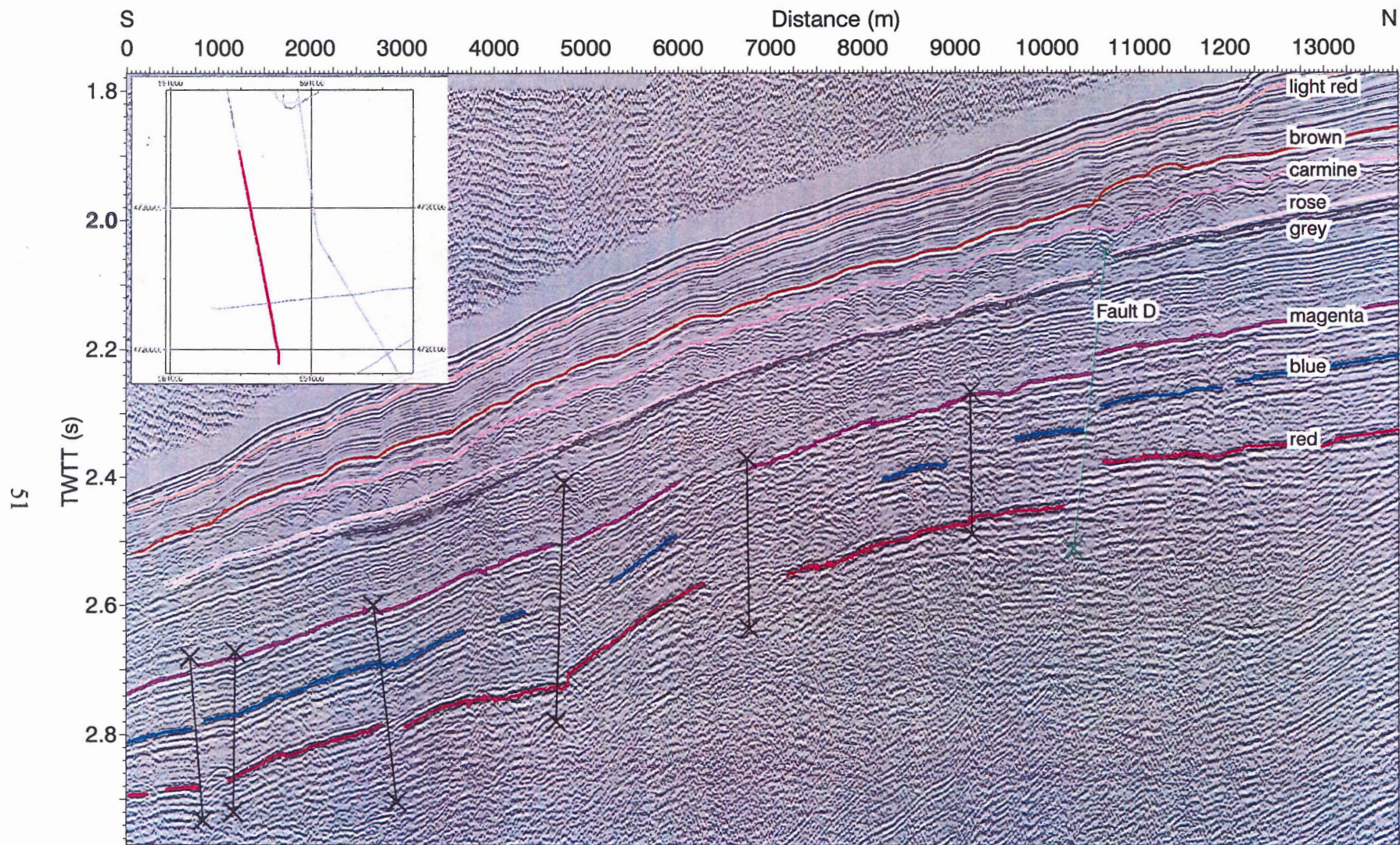
Figure 4.7: Part of line 99036-114 showing Fault D (green line) and six other faults (black lines). Inset map shows location of section.

Displacement is much less 4.9 km east and 2.8 km west where offset is approximately 59 ms.

In the western portion of the study area, there is a set of at least six faults on the mid-slope (Fig. 4.7). The northernmost, Fault D, is the most significant of these. Fault D is a normal fault with 62 ms of displacement at red. Fault D was active during the red-blue interval and during the flesh-carmine interval as indicated by upslope thinning and downslope thickening. This fault occurs on line 99036-114 and cannot be correlated eastward on other lines. South of Fault D is a series of faults on line 99036-114 that can be correlated eastward to lines 99036-111 and 110. These faults have various displacements on the order of 20 ms. Most are normal faults, but at least two show reverse displacement. These faults verge either basinward or landward. Within the faulted area, the resulting structure at red forms a domal shape. It is difficult to determine when these faults were active; displacement is visible up to the grey horizon.

A similar set of faults, but all with basinward, normal displacement exists on the eastern margin of the study area on the mid- slope on the north end on line 99036-104. These faults show 25 ms displacement on average, and were active during the magenta-grey interval.

4.6 Correlation to Exploration Wells

Correlation to both Acadia K-62 and Shubenacadie H-100 exploration wells was attempted using synthetic seismograms. Because both wells were drilled for hydrocarbon exploration, samples from the upper strata were discarded and were only logged with the neutron density and gamma ray tools. At Acadia K-62, first cutting samples are from 1200 m below the rotary table (m RT). Velocity logs end (shallowest reading) at 1181 m RT and density logs end at 2558 m RT. In Shubenacadie H-100 first samples are obtained 2145 m RT and velocity logs end at 2581 m RT. Unfortunately, the velocity log ends below the depth of penetration of the seismic data used in this study, and the samples at 2145 m RT begin just below the red horizon. A synthetic seismogram useful for this study for the Shubenacadie H-100 well cannot be created from these data; therefore, borehole information cannot be accurately correlated to seismic.

A synthetic seismogram was constructed with the velocity log from Acadia K-62 and correlated with seismic line 2001-048A-30 (Fig. 4.8). The correlation is somewhat tenuous. The borehole is located to the north of a fault and penetrates a channel or the levee of a channel above grey. The correlation of the synthetic is based primarily on the deeper horizons, because of the complex nature of seismic data above magenta. The tie shows that the first samples from Acadia K-62 at 1200 m were taken within the grey-rose interval near the grey horizon. The magenta horizon shows a very weak tie to the synthetic seismogram; however, the red and blue horizons correlate well with the synthetic seismogram. The magenta interval lies at a depth of 1302 m followed by blue at 1353 m and red at 1425 m, based on these correlations. Other events observed in the synthetic seismogram correlate loosely with events on the seismic sections.
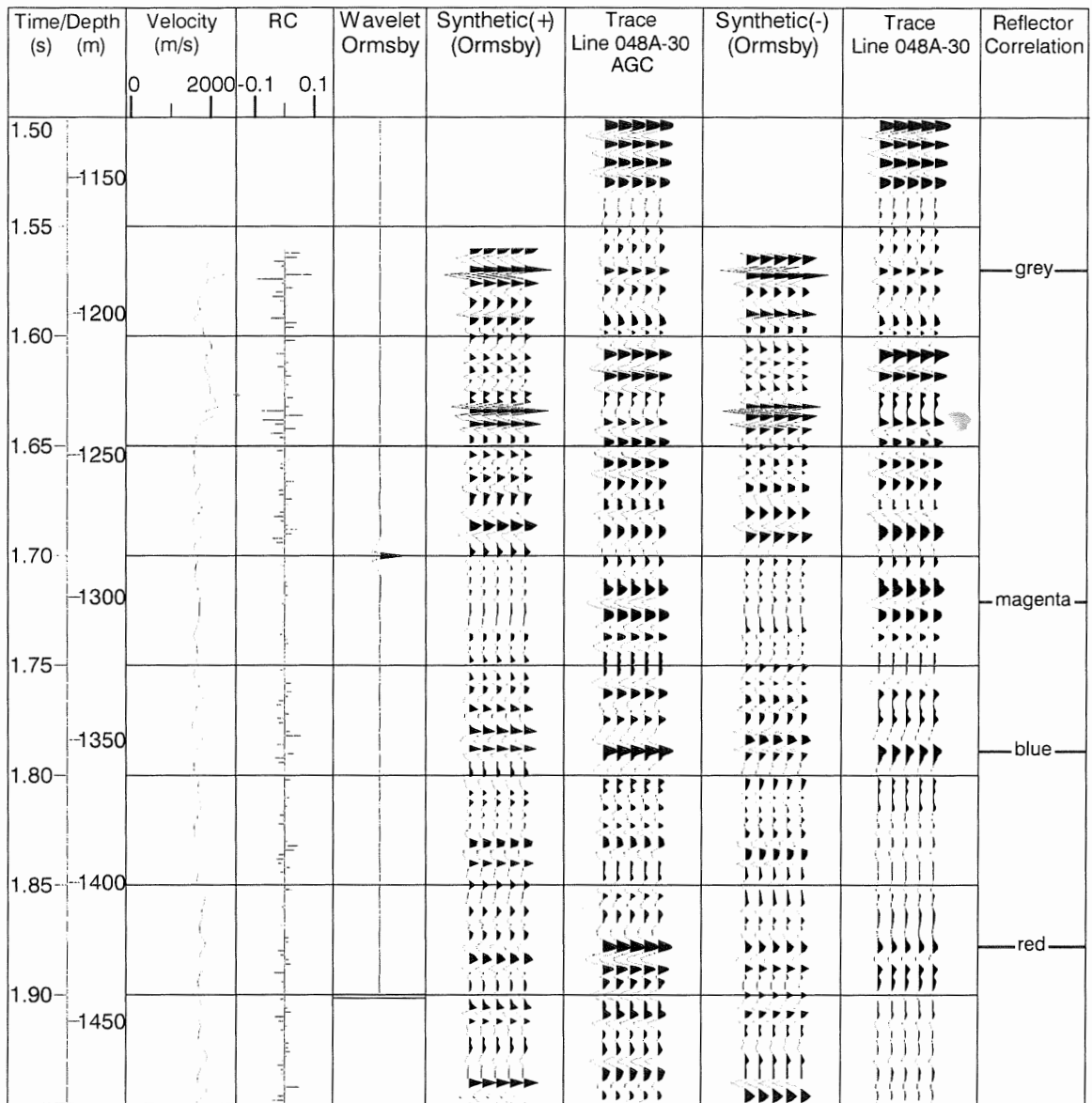
Figure 4.8: Correlation of synthetic seismogram for Acadia K-62 with high-resolution seismic section. The reflection coefficient (column 3) is generated from the velocity well log (column 2) as there are no density logs through this interval.. The reflection coefficient is convolved with an Ormsby wavelet (column 4), which approximates the source signature to generate a synthetic seismogram (columns 5 and 7; positive and negative polarity respectively). The negative polarity synthetic seismogram is correlated with the five closet seismic traces of line 2001-048A-30, which are presented both with and without automatic gain control applied (columns 6 and 8 respectively). The negative synthetic is used because the seismic is loaded as reverse polarity for this line. Correlation of the synthetic seismogram with the seismic traces produces a TWTT - depth relationship (column 1).

Piper *et al.* (1987) report age correlations from upper borehole samples both in the Acadia K-62 and Shubenacadie H-100 wells. They suggest that the first sample from the Acadia K-62 site at 1200 m has an uppermost Pliocene foraminiferal assemblage (upper part of zone N21: 1985 in Piper *et al.*, 1987). Some Pleistocene species were observed at 1260 m, but it is thought that this is the result of downhole contamination as a result of cave-in while drilling. Piper *et al.* (1987) also report that the first mid-Pliocene assemblages (zones N19-N20) occur at 1650 m RT and continue to 1720 m RT. This fact suggests that the grey horizon marks the base of the Pleistocene at 1.6 Ma.

The first samples in the Shubenacadie H-100 well were recovered at 2140 m. These samples have been assigned a mid- to Late Pliocene age (foraminifer zones N19-N21; Piper *et al.*, 1987). Piper and others report that this corresponds to a horizon below red.

4.7 Sources of Error

There are several areas where error can be introduced the seismic horizon picks, problems related to the seismic datum, and age control.

It is difficult to quantify the error from seismic horizon picks. All of the picks have been examined at least three times, and the ties have been carefully scrutinized. All of the horizons interpreted are distinctive, and correlate well throughout the study area.

Some issues arise when considering the reference datum of the seismic data. All of the lines used in this study were tied to line 2001-048A-29. In spite of this calibration, some lines within the same survey and between multiple surveys do not tie correctly. These misties are likely the result of navigational errors. Every line has been adjusted as

best as possible so that line crossings tie as closely as possible, but some offsets remain, which are apparent on some of the maps in Appendix A and B.

The most difficult problem to address in this study is age control. Age assignments are based on either micropaleontological analysis of well cuttings, or on extrapolation, assuming linear sedimentation rates. It is important to note that the depth of well cuttings have a high degree of uncertainty, but are useful for approximate ages used in this study.

Survey line spacing constrains the resolution of this study. Some line spacings reach 15 km, implying interpolation is required for large areas where no data exist.

CHAPTER 5

INTERPRETATION AND CONCLUSIONS

5.1 Timing of Events

The Plio-Pleistocene depositional history of the study area is constrained by age control from three horizons. Foraminiferal assemblages from exploration wells indicate 1) Late Pliocene age for the red horizon and 2) a basal Pleistocene age (1.8 Ma) for the grey horizon. 3) The carmine horizon is identified as the commencement of shelf crossing glaciation on the Scotian Margin and so is assigned an age of 0.45 Ma (Piper, 2001). Reflectors at carmine and above interfinger with wedges of unstratified sediment upslope (Facies 4; Fig. 4.4); these incoherent wedges are identified as till tongues (Piper at al. 1985, 1987; King and Fader, 1986). Several authors have attempted to establish till tongue stratigraphy to apply ages to horizons within the study area (Mosher *et al.*, 1989; Gauley, 2001) and in other areas of the Scotian Margin (Piper *et al.*, 2002). Seismic data examined in this study suggest the lowest till tongue lies immediately below the carmine horizon. The commencement of shelf-crossing glaciation may occur immediately below carmine; however, the carmine horizon is used as the marker horizon for this event because it is high-amplitude and continuous (correlateable) throughout the study area.

5.2 Depositional History

The intervals identified are categorized into two groups: sediment deposited prior to glaciation and sediment deposited during glacial and interglacial periods. Sediment between the red and carmine horizons were deposited prior to major shelf-crossing glaciations and are referred to as non-glacial strata based on the lowermost occurrence of

the till tongues at the carmine horizon. Sediment between the carmine horizon and the seafloor were deposited during glacial/interglacial cycles and are glacially influenced.

5.2.1 Non-glacial Sequences

The non-glacial interval is composed of nine cycles of Facies 1-2 sequences that thin moderately downslope. Sedimentation appears to be dominated by hemipelagic processes based on the draping nature of reflectors within the group. The seismic character of Facies 1 and 2 are open to interpretation; however, with the ties to industry wells, well cuttings and logs suggest that Facies 1 is interbedded silty clay and sand (or sandy clay) and Facies 2 is silty mud. High amplitude, laterally continuous reflectors of Facies 1 presumably corresponds to turbidite depositional processes and low amplitude discontinuous reflectors of Facies 2 presumably corresponds to hemipelagic drape similar to acoustically incoherent sediment deposited on the Scotian Slope during the Holocene.

The non-glacial interval is marked by three erosional events: development of a minor escarpment within the red-blue interval, large-scale erosion within the magenta-grey interval, and erosion during the rose-flesh interval. The escarpment in the red-blue interval developed on the mid- to lower slope, but the erosional feature is not extensive and only observed on two seismic lines.

The base of Facies 3 within the magenta-grey interval is interpreted as a significant, widespread erosional event and is marked by local erosion into Facies 1 of the magenta-grey interval. Erosion of Facies 1 corresponds to the development of mounds interpreted as overbank deposits that are common in the central and western portions of the study area. Erosion during this time period may have removed strata to

58
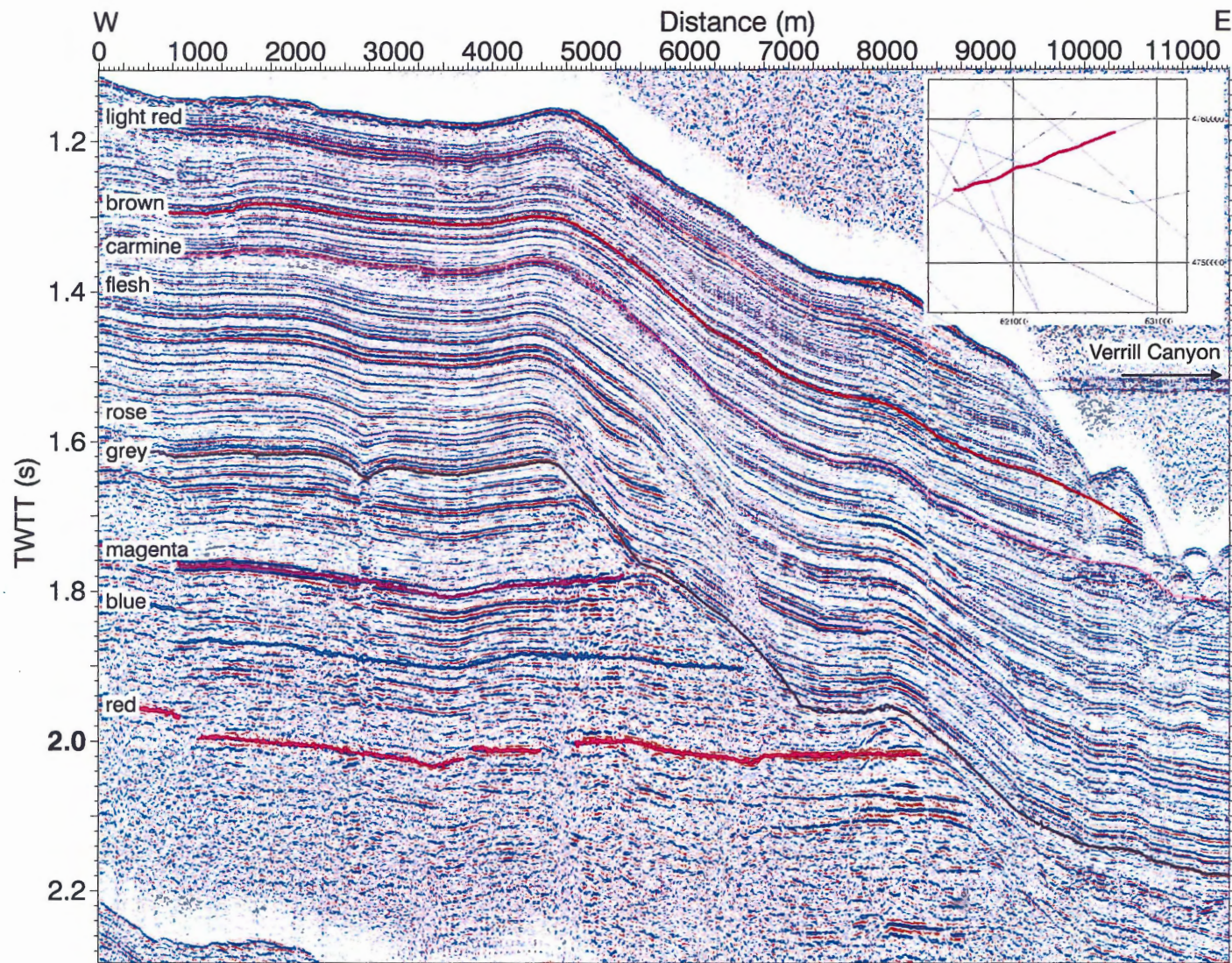
Figure 5.1: Part of line 2002-046-58 showing erosion of magenta to below red. Inset map for location.

the red reflector, and locally deeper on the flanks of Verrill Canyon. This erosion resulted in removal of at least 390 ms of sediment on the mid-slope (Fig. 5.1). The amount of erosion decreases downslope where the red, blue, and magenta reflectors abut a salt dome. The step-like morphology of the unconformity suggests that erosion may have occurred in two phases, but there is no collaborative evidence to support this suggestion. Erosion during the magenta-grey interval may relate to movement along Fault B. Thinning on the north side of the fault and thickening on the south side suggests that Fault B was active during deposition of this interval.

A significant escarpment develops on the lower slope during the rose-flesh interval. The escarpment removes 65 ms of sediment on the lower slope. In the eastern portion of the study area this escarpment divides into two separate bathymetric features which cannot be correlated past the margin of Verrill Canyon.

5.2.1 Glacial Sequences

The glacial period is composed of eight cycles of Facies 1 / Facies 2 sequences that interfinger on the upper slope with six till tongues (Fig. 4.4). Sedimentation appears to be hemipelagic based on the draping nature of the facies. Isochron maps show sediment accumulation is greatest on the upper slope and exhibits rapid downslope thinning (Fig. B10).

There is little lithologic information available for the glacial interval. Facies 1 may represent alternating beds of sand and mud as indicated by the high amplitude, coherent reflections within the facies, and the facies groundtruth with the Acadia K-62

well, as described earlier. Facies 2 may represent silty clay similar to modern Holocene sediment on the Scotian Slope.

Four erosional events occur during the glacial period: erosion at the carmine horizon, erosion of the entire carmine-brown interval on the lower slope, a minor escarpment that develops on the mid- to upper slope at light red, and the disturbed zone near the seafloor on the mid- and upper slope.

The commencement of shelf-crossing glaciation corresponds to substantial erosion in the western portion of the study area, which created the Acadia Valley system. The escarpment heads in the upper slope west of Acadia K-62 and deflects south to form a slope parallel topographic feature. The escarpment has eroded strata down to the upper parts of the grey-rose interval, which on the upper slope corresponds to 170 ms of strata that has been removed. This major escarpment within the study area also shows a step-like morphology (Fig. 5.2), which corresponds to the top of Facies 1 of the lower cycle of the rose-flesh interval, suggesting increased competence of Facies 1 strata. Following this episode of mass wasting, three channels develop in the Acadia Valley system. The two eastern channels form the East Acadia Valley, and the western channel forms the West Acadia Valley. The western channel appears to have developed at the same time as Facies 5 was deposited. Facies 5 may represent the development of a debrite within the Acadia Valley system. The morphology of the western channel shows a distinct levee and overbank deposit (Fig. 5.3). The exact timing of erosion forming the eastern and central channels is uncertain. Levees are not developed on these channels and the channels do not appear to erode the strata below the unconformity. The central channel formed in a bathymetric low that developed during the magenta-grey interval. The
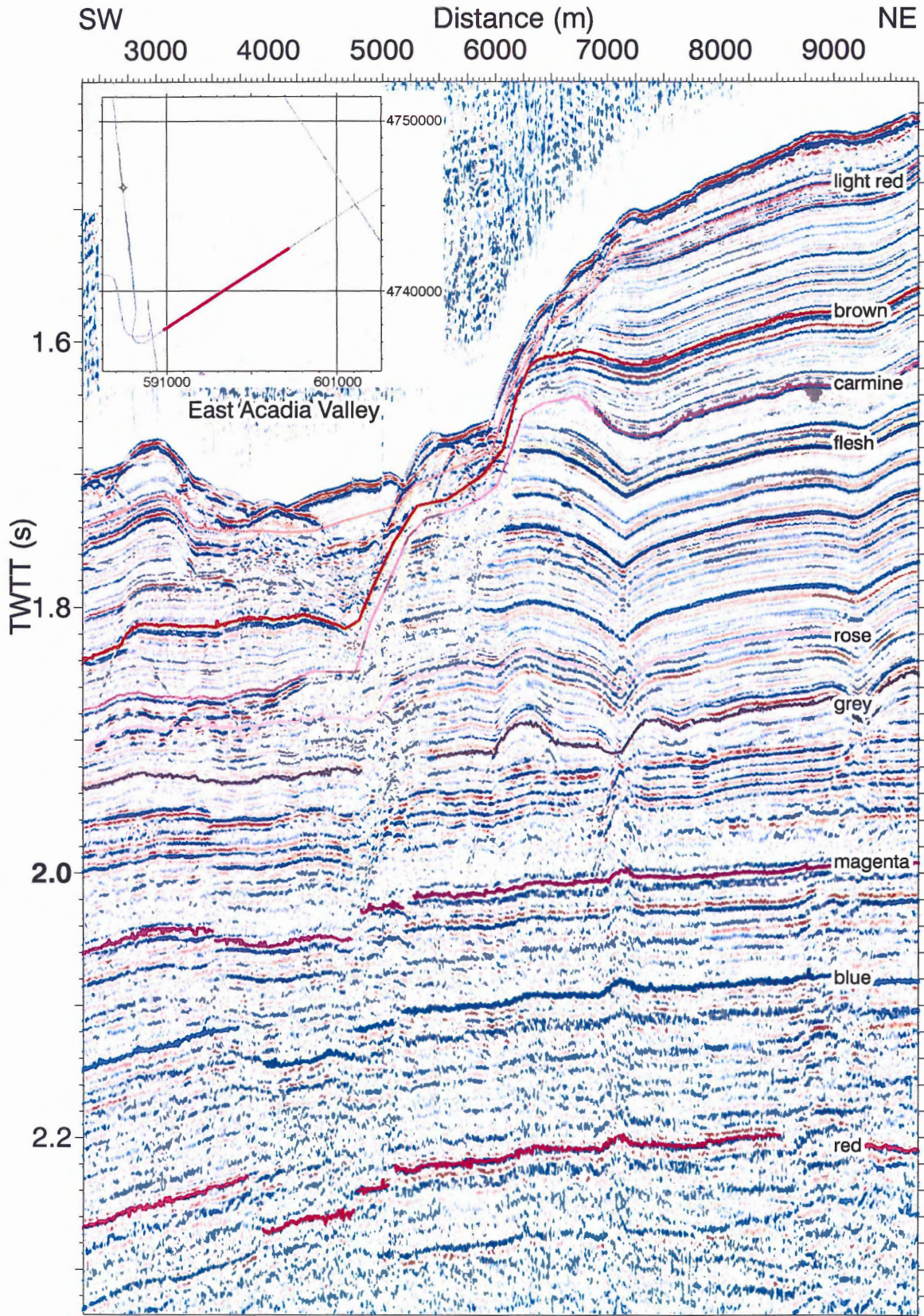
Figure 5.2: Part of line 2001-048A-29 showing erosion from flesh to below rose.
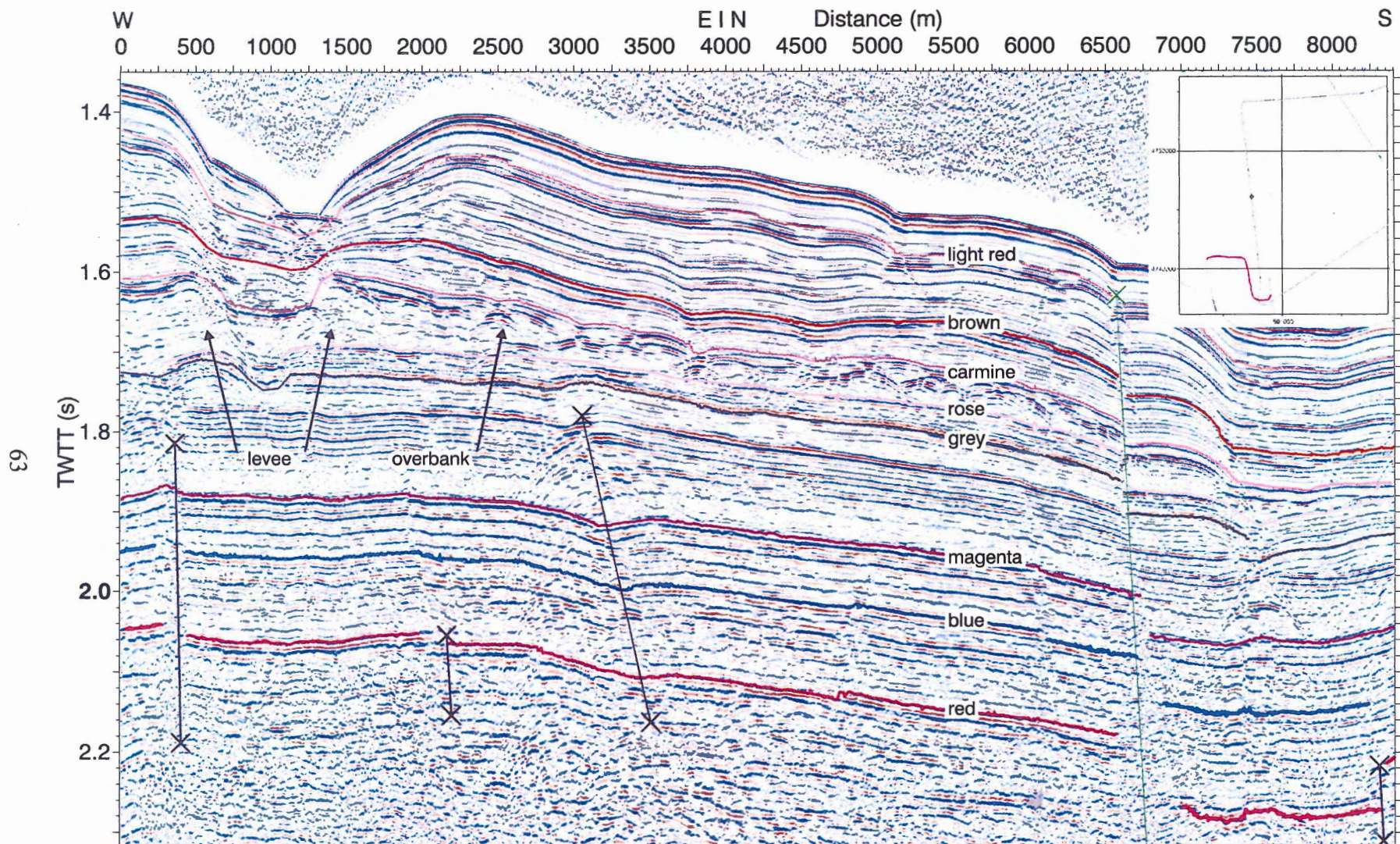
Figure 5.3: The western channel of the Acadia Valley system is imaged on line 99036-113. Several faults are visible including Fault C (green line).

eastern channel developed along the flank of the unconformity. During this interval, fault D was active on the mid-slope suggesting that erosion may be linked to fault activity.

The carmine-brown interval is entirely truncated by an escarpment on the lower slope in the central portion of the study area. On the eastern and western extents of the study area the escarpment deflects upslope where it heads on the upper slope.

Approximately half of the brown-light red interval is truncated on the mid-slope. On the lower slope, several 1-2 km-wide channels incise most of the interval. The resolution of the seismic data prevents identifying whether these channels developed at or beneath the light red reflector. Two channels are observed on the upper slope in the Acadia Valley System. Fault C may have been active during this period.

The disturbed seafloor described by Mosher *et al.* (1994) is the fourth erosional event within glacial sediment. Up to 10 ms of strata are eroded in two large areas of the seafloor on the upper and mid- slope. Mosher et al. (1994) ascribe this event to seismically triggered slope failure.

5.3 Comparison of Non-glacial and Glacial Time Periods

A comparison of the non-glacial intervals (red to carmine) and glacial intervals (carmine to seafloor) shows three overall differences. 1) Sediment accumulation patterns reveal greater volumes of sediment were deposited on the upper slope during periods of glaciation. 2) Slope instability and related failures were more frequent during periods of glaciation, and 3) an increase in frequency of Facies 1 / Facies 2 sequences during glacial intervals.

Accumulation patterns are different in glacial and non-glacial sediment. The interval isochron for the carmine-seafloor period (Fig. B10) shows significant sediment accumulations on the upper slope and rapid downslope thinning. This downslope thinning is especially pronounced in the brown-seafloor interval. The non-glacially influenced strata display less prominent downslope thinning (Fig. B9).

Three erosional events occur within the pre-glacial period and four occur during the glacial period. The number of events is more significant when time is considered. The grey horizon provides the deepest well-constrained age control at 1.8 Ma. Only two periods of slope instability occur between grey and carmine during 1.35 m.y. of non-glacial sedimentation. This period of relative slope stability contrasts the four distinct events that occur during the 0.45 m.y. of glacial sedimentation and implies the slope was unstable during the glacial period.

The frequency of Facies 1 / Facies 2 cycles increases during the glacial period. The strata between grey and carmine show seven cycles during a 1.35 m.y. time period. The carmine to seafloor interval shows eight cycles during a 0.45 m.y. time period. Above the carmine horizon, Facies 2 comprises a larger portion of the interval. In the pre-glacial strata, Facies 1 comprises half of the interval.

5.4 Implications of Results

The results of this stratigraphic study show a potential relationship between activity on faults and development of substantial erosion. The development of Facies 3 at the top of the grey interval and the development of the escarpment on the western margin corresponds to activity on some of the faults (e.g. Fault B) in the eastern region of the

study area. The development of the Acadia Valley appears to be linked to activity on

Fault D in the western portion of the study area.   Data presented show that major failures

may occur with periods of activity on faults. Publicly available, multi-channel industry

seismic lines 83-582aa 88-1a indicate that these faults may be related to salt tectonism.

Salt diapirs underlie much of the Scotian Slope (Wade and MacLean, 1990; Kidston *et

al.*, 2002). Based on interpretations of these industry sections it is interpreted that faults

were more active earlier in the eastern portion of the study area and active recently in the

western portion of the study area (J. Shimeld, pers. comm., 2003). Faulting likely acts in

concert with other factors to produce slope instability.

Gauley (2001) identified four main mechanisms for sediment failure on the

central Scotian Slope: 1) earthquakes, 2) deep and 3) shallow excess pore pressure due to

rapid sedimentation, and 4) dissociation of gas hydrates. Rapid loading of glacio-marine

sediment is considered a factor in slope stability because it could prevent drainage,

resulting in over-pressure of the pore-water. Dissociation of methane hydrates and

adjustment of the hydrate stability zone with fluctuating climate and sea level could cause

failures on the slope. Other mechanisms were discounted for various reasons including

tidal activity, storm loading, bioturbation, and mud-diapirs. Gauley (2001) provides

convincing evidence that tectonic failure cannot be responsible for all failures based on

the frequency of failures and the potential frequency of earthquakes. This study lacks

necessary precision to delineate the various factors contributing to slope instability;

however, a link to faulting, potentially related to salt tectonism is added as a failure

mechanism possibility.

This thesis also showed that the carmine reflector might not correspond to the commencement of major shelf crossing glaciations as promoted by Piper *et al.* (1987). Examination of the high-resolution seismic data on computer workstations permits more detailed stratigraphic analysis of the seismic sections, and permitted the identification of a till tongue immediately below the carmine reflector, suggesting that a reflector between flesh and carmine corresponds to the commencement of shelf crossing glaciation. The carmine reflector marks the first change from glacial to interglacial sediments within this interval.

5.4.1 Implications to Hydrocarbon Development

The results of this thesis have implications on hydrocarbon exploration within the area in relation to near seafloor geohazards. Mosher *et al.* (1994) have shown that the seafloor is stable in the region under current conditions and slope instability must be triggered. The data set used for this analysis provides little means of determining precisely when fault C was most recently active. Timing is difficult to determine because near surface sediment may drape the fault, or be offset by the fault. Smaller line spacing of high-resolution data or 3D seismic data may resolve the timing of movement on this fault. Renewed activity on these faults could cause slope instability.

5.5 Conclusions

The Late Pliocene to Recent development of the central Scotian Slope is dominated by hemipelagic and turbidite deposition interrupted by two major phases of slope failure. Pre-glacial (older than mid-Pleistocene) sediment is composed of

alternating sequences of Facies 1 and Facies 2. Pre-glacial strata also incurred rare, small slope failures of minor volume. The glacial period incurred common large slope failures and possibly frequent minor slope failures. There is a marked change in sediment accumulation patterns between glacial and non-glacial periods. The glacial period incurred thick sediment accumulation on the upper slope, which contrasts a gentle gradient of downslope thinning for pre-glacial intervals.

Activity on shallow faults correlates with periods of major slope instability both on the western margin of Verrill Canyon and more recently with the creation of the Acadia Valley system, but do not correlate with smaller scale slope instability features.

5.6 Recommendations for Future Work

There is great scope for future research in this area of the Scotian Slope. There is a need to establish more accurate age relationships for the deeper intervals within this study. This study confidently correlates the rose and flesh horizons and tentatively correlates the grey horizon through the area of significant salt deformation at the base of the slope. It is expected that these horizons can be correlated through the continental rise to deep-sea core sites to obtain further age constraints.

Future work within the study area would benefit from added groundtruthing. There is very little lithologic information beyond the reach of piston cores; understanding the subsurface in this area depends on control obtained through lithologic information. The area is currently under active hydrocarbon exploration, and additional information obtained from potential hydrocarbon exploration wells would greatly increase our understanding of the area. Industry 3D seismic surveys may also contribute to further

understanding within the area permitting investigation of features within the large data gaps of this analysis.

Other future work might include examining the shelf slope transition to help understand the interactions between the shelf and the slope. Single-channel lines used in this study do not permit investigations in shallow water because of water bottom multiples. A survey consisting of high-resolution, processed, multi-channel seismic lines would allow further work in understanding this part of the system. There is potential that glacial features exist deeper in the section, but currently this is obscured by seafloor multiples and signal attenuation on the seismic sections.

REFERENCES

Baltzer, A., Cochonat, P., and Piper, D.J.W. 1994. In situ geotechnical characterization of sediments on the Nova Scotian Slope, eastern Canadian continental margin. Marine Geology, **41**: 291-308.

Bennett, J.R. 2000. Near-surface faults on the Scotian Slope, Eastern Canada. Unpublished B.Sc. (honours) thesis, Saint Mary's University, Halifax, Nova Scotia, 63 pp.

Gauley, B.-J.L. 2001. Lithostratigraphy and sediment failure on the central Scotian Slope. M.Sc. thesis, Dalhousie University, Halifax, Nova Scotia, 214 pp.

LeBlanc, R.C. 2002. Central Scotian Slope stability: the possible role of methane hydrates. Unpublished B.Sc. (honours) thesis, Dalhousie University, Halifax, Nova Scotia, 79 pp.

Haq, B.U., Hardenbol, J., and Vail, P.R. 1987. Chronology of fluctuating sea levels since the Triassic. Science, **235**: 1156-1157.

Hill, P.R., Piper, D.J.W., and Normark, W.R. 1983. PISCES IV submersible dives on the Scotian Slope at 63°W. Current Research part A. Geological Survey of Canada, **83-1A**, 65-69.

Keen, C.E., Loncarevic, B.D., Reid, I., Woodside, J., Haworth, R.T., Williams, H. 1990. Tectonic and geophysical overview. *In* Geology of the continental margin of eastern Canada. *Edited by* M.J. Keen and G.L. Williams. Geological Survey of Canada Geology of Canada No. 2, Chap. 2, pp. 31-85.

Kidston, A.G., Brown, D.E., Altheim, B., and Smith, B.M. 2002. Hydrocarbon Potential of the Deep-Water Scotian Slope. Canada-Nova Scotia Offshore Petroleum Board, Halifax, Nova Scotia, 111pp.

King, L.H., and Fader, G.B. 1986. Wisconsinan Glaciation on the continental shelf – southeast Atlantic Canada. Geological Survey of Canada, Bulletin 363.

Mosher, D.C. 1987. Late Quaternary sedimentology and sediment instability of a small area on the Scotian Slope. M.Sc. thesis, Memorial University of Newfoundland, St. John's, Newfoundland, 248 pp.

Mosher, D.C. 2000. CCGS Hudson Cruise 2000-042 expedition report, Scotian Slope. Unpublished GSC Internal Report, 50 pp.

Mosher, D.C. 2001. CCGS Hudson Cruise 2001-048A expedition report, Scotian Slope. Unpublished GSC Internal Report, 32 pp.

Mosher, D.C., Piper, D.J.W.P., Campbell, D.C., and Jenner, K.A. In press. Near surface geology and sediment failure geohazards of the central Scotian Slope. *In* High Resolution Geological and Geophysical Studies of Continental Margin Geohazards. *Edited* by W. Stager, E.H. Doyle, and W. Bryant. American. Association of Petroleum Geologists Memoir ###.

Mosher, D.C., MacDonald, R., Hewitt, A.T., and Hill, W.T. 1998. Small airgun arrays for high resolution geophysical surveying. Geological Survey of Canada, Current Research, 1998D, pp. 43-50.

Mosher, D.C., Moran, K., and Hiscott, R.N. 1994. Late Quaternary sediment, sediment mass flow processes and slope stability on the Scotian Slope, Canada. Sedimentology, **41**: 1039-1061.

Mosher, D.C., Piper, D.J.W., Gustavs, V.V., Aksu, A.E., and Fader, B.F. 1989. Evidence for Wisconsinan Glaciations in the Verrill Canyon Area, Scotian Slope. Quaternary Research, **31**: 27-40.

Pickrill, R.A., Piper, D.J.W., Collins, J.T., Kleiner, A., and Gee, L. 2001. Scotian Slope mapping project: the benefits of an integrated regional high-resolution multibeam survey. Offshore Technology Conference paper, OTC 12995.

Pieuchot, M. 1984. Volume 12: Seismic Instrumentation. *In* Handbook of Geophysical Exploration, Section 1: Seismic Exploration. Edited by H. Klaus and S. Treitel. Geophysical Press, London, England, 375 pp.

Piper, D.J.W. 1999. CCGS Hudson 1999-036 expedition report, Scotian Slope. Unpublished Internal GSC Report, 86 pp.

Piper, D.J.W. 2001. The Geological Framework of Sediment Instability on the Scotian Slope: Studies to 1999. Geological Survey of Canada Open File 3920, 202 pp.

Piper, D.J.W., and Mosher, D.C. 2002. CCGS Hudson Cruise 2002-046 expedition report, Scotian Slope. Unpublished GSC Internal Report, 62 pp.

Piper, D.J.W., and Normark, W.R. 1989. Late Cenozoic sea-level changes and the onset of glaciation: impact on continental slope progradation off eastern Canada. Marine and Petroleum Geology, **6**: 336-347.

Piper, D.J.W. and Sparkes, R., 1990. Pliocene – Quaternary geology, central Scotian Slope. Geological Survey of Canada Open File 2233.

Piper, D.J.W, Farre, J.A., Shor, A. 1985. Late Quaternary slumps and debris flows on the Scotian Slope. Bulletin of the Geological Society of America, **96**: 1508-1517.

Piper, D.J.W., Normark, W.R. and Sparkes, R. 1987. Late Cenozoic acoustic stratigraphy of the central Scotian Slope, eastern Canada: Canadian Bulletin of Petroleum Geology, **35**: 1-11.

Piper, D. J. W., Mudie, P. J., Fader, G. B., Josenhans, H. W., MacLean, B., and Vilks, G. 1990. Quaternary Geology. *In* Geology of the continental margin of eastern Canada. *Edited by* M.J. Keen and G.L. Williams. Geological Survey of Canada Geology of Canada No. 2, Chap. 10, pp. 475-607.

Piper, D.J.W., Mosher, D.C., Newton, C.S. 2002. Ice-margin seismic stratigraphy of the central Scotian Slope. Geological Survey of Canada Current Research, 2002-E16, 10 pp.

Telford, W.M., Geldart, L.P., and Sheriff, E.R. 1976. Applied Geophysics. Cambridge University Press, Cambridge, 860 pp.

Verbeek, N.H. 1995. Aspects of high resolution marine seismics. Post-doctoral thesis, Utrecht University, Utrecht, The Netherlands, 52 pp.

Wade, J. and MacLean, B. 1990. The geology of the southern margin of Canada. *In* Geology of the continental margin of eastern Canada. *Edited by* M.J. Keen and G.L. Williams. Geological Survey of Canada Geology of Canada No. 2, Chap. 5, 167-238.

Yuan, T., Hyndman, R.D., Spence, G.D., and Desmos, B. 1996. Seismic Velocity Increase and Deep-Sea Gas Hydrate Concentration Above a Bottom-Simulating Reflector on the Northern Cascadia Continental Slope. Journal of Geophysical Research, **101**: 13655 – 13671.

Yilmaz, O. 1987. Seismic Data Processing. Society of Exploration Geophysicists, Tulsa, Oklahoma, USA, 526 pp.

APPENDIX A:
STRUCTURE MAPS FROM REFLECTION PROFILES

TABLE OF CONTENTS

Figure A1: Red horizonstructure map. The red horizon cannot be accurately correlated in the southeast region of the study area. Scale bar indicates TWTT in seconds. Contour interval is 25 ms with bold contours every 125 ms.
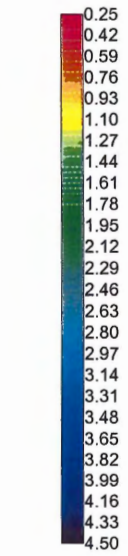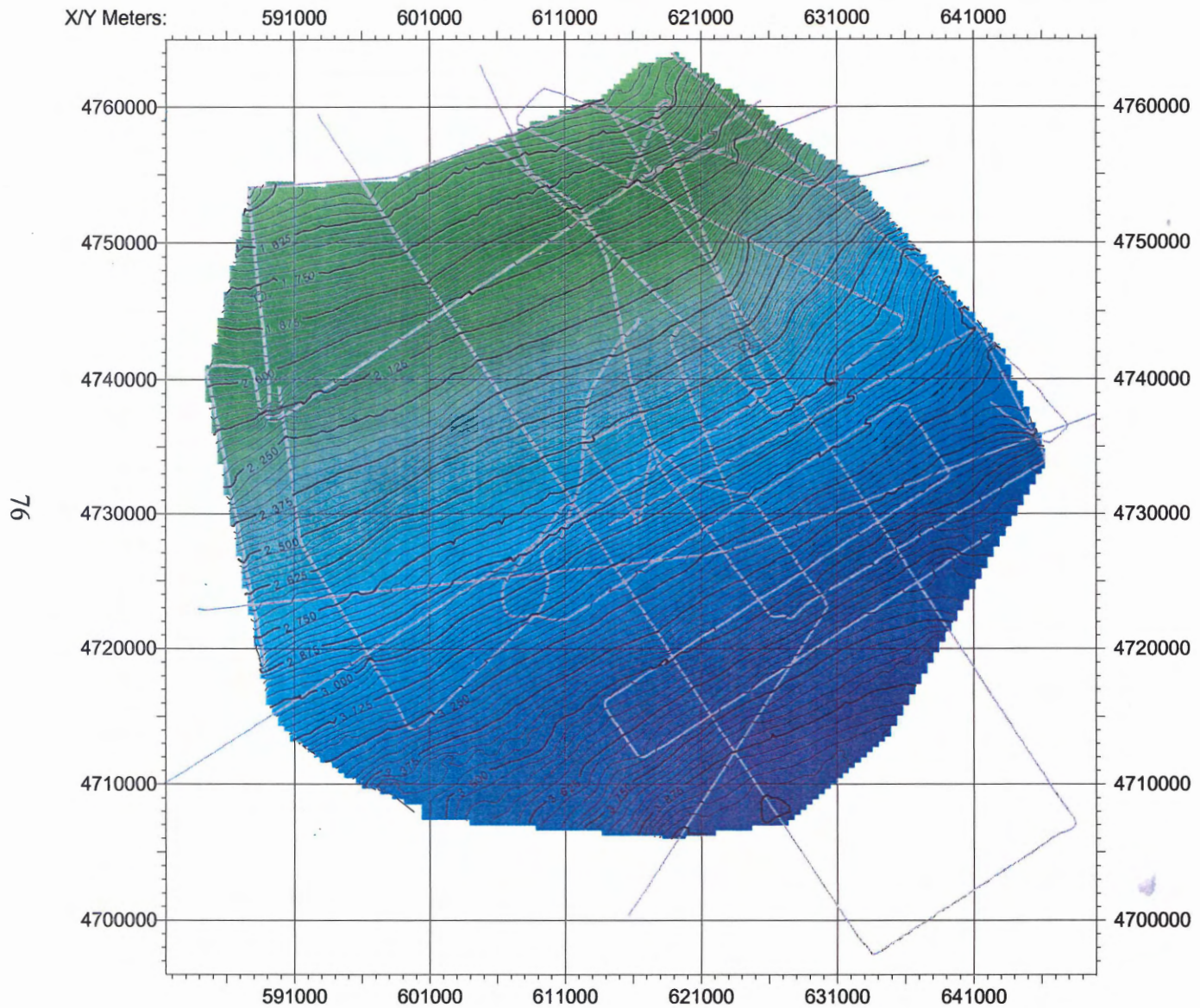
Figure A2: Blue horizon structure map. The blue horizon cannot be accurately correlated in the southeast region of the study area. Scale bar indicates TWTT in seconds. Contour interval is 25 ms with bold contours every 125 ms.
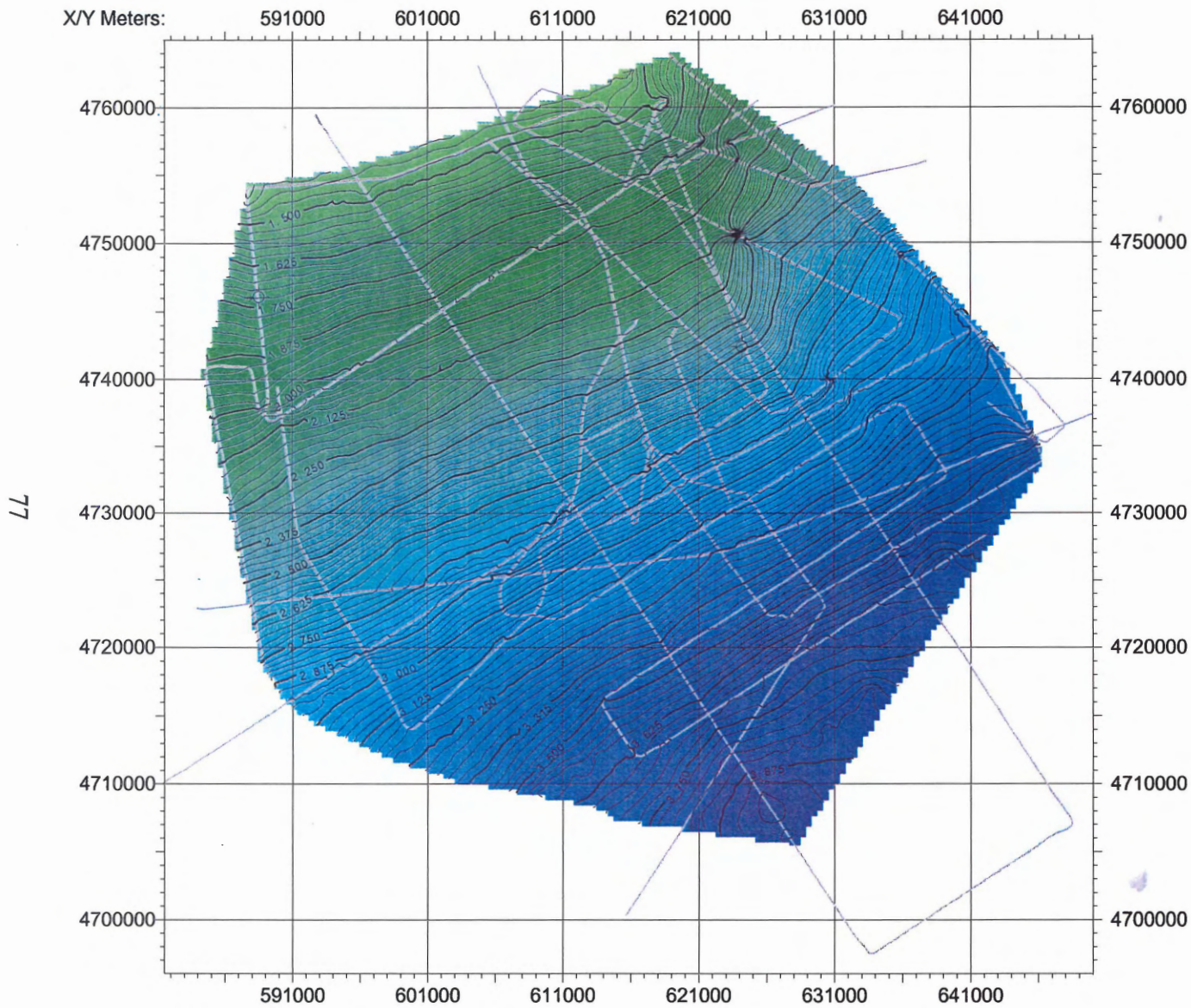
Figure A3: Magenta horizon structur emap. The magenta horizon cannot be accurately correlated in the southeast region of the study area. Scale bar indicates TWTT in seconds. Contour interval is 25 ms with bold contours every 125 ms.
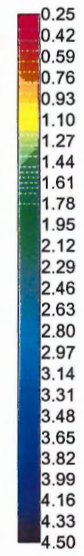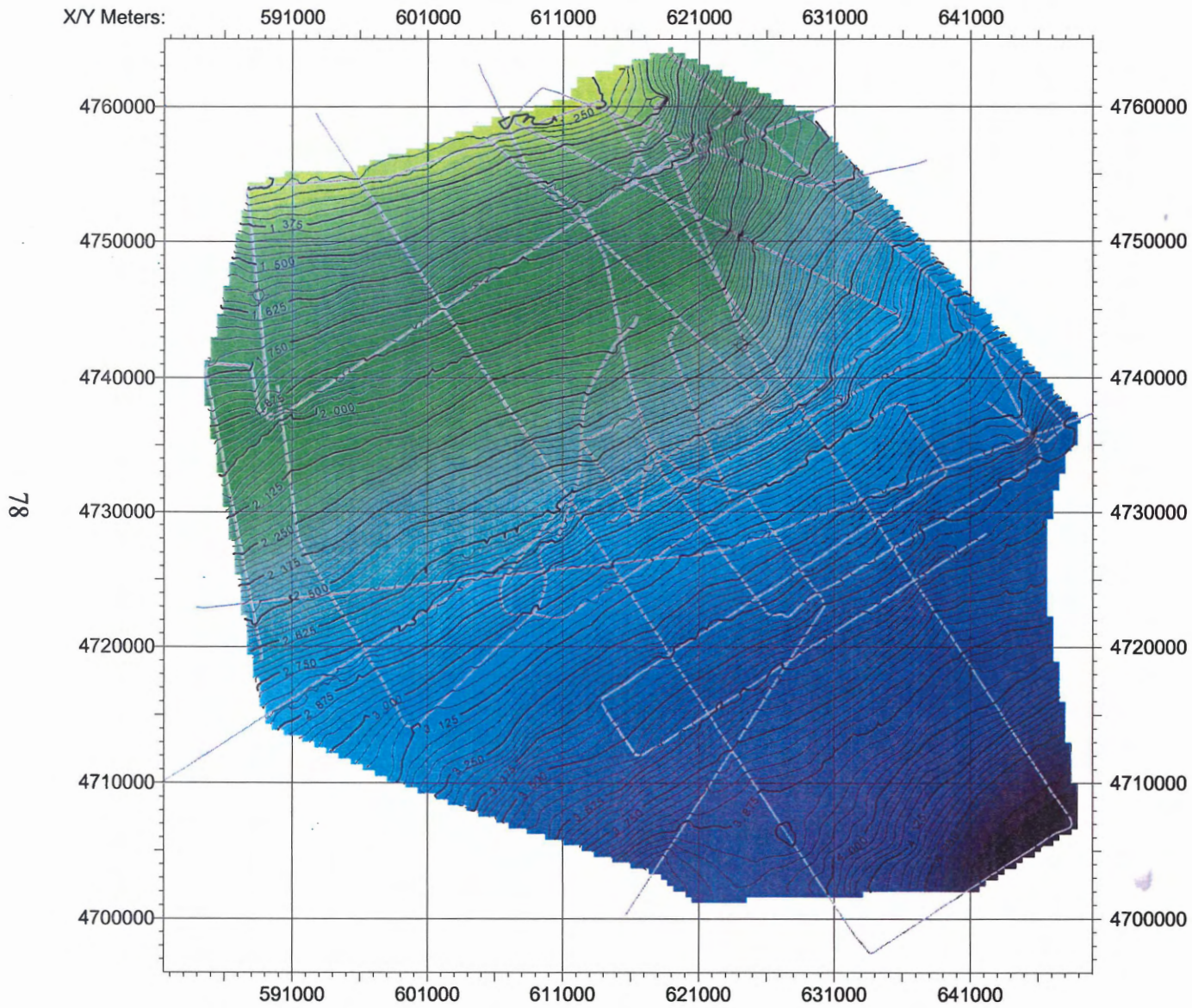
Figure A4: Grey horizon structure map. Scale bar indicates TWTT in seconds. Contour interval is 25 ms with bold contours every 125 ms.
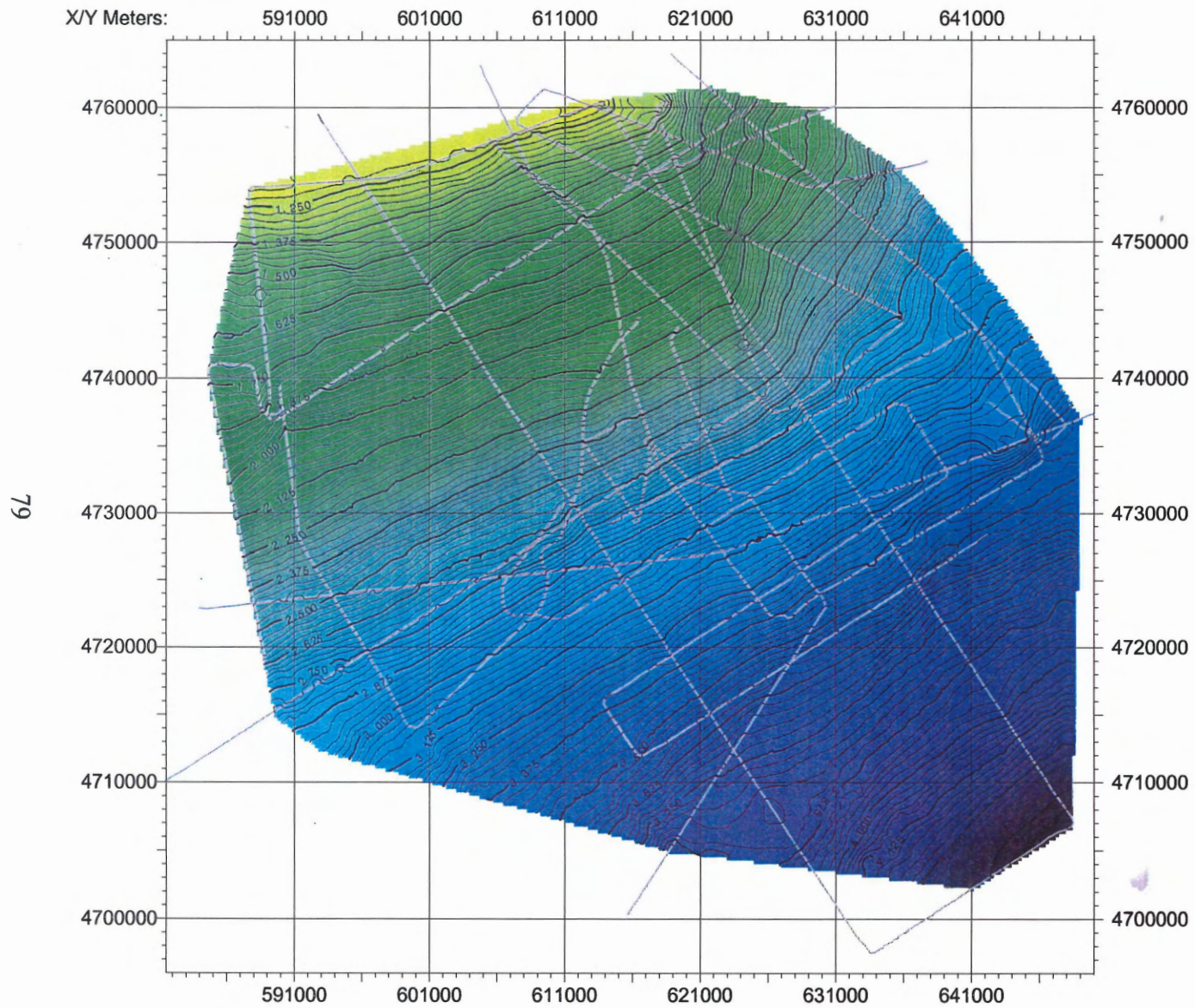
Figure A5: Rose horizon structure map. Scale bar indicates TWTT in seconds. Contour interval is 25 ms with bold contours every 125 ms.

79
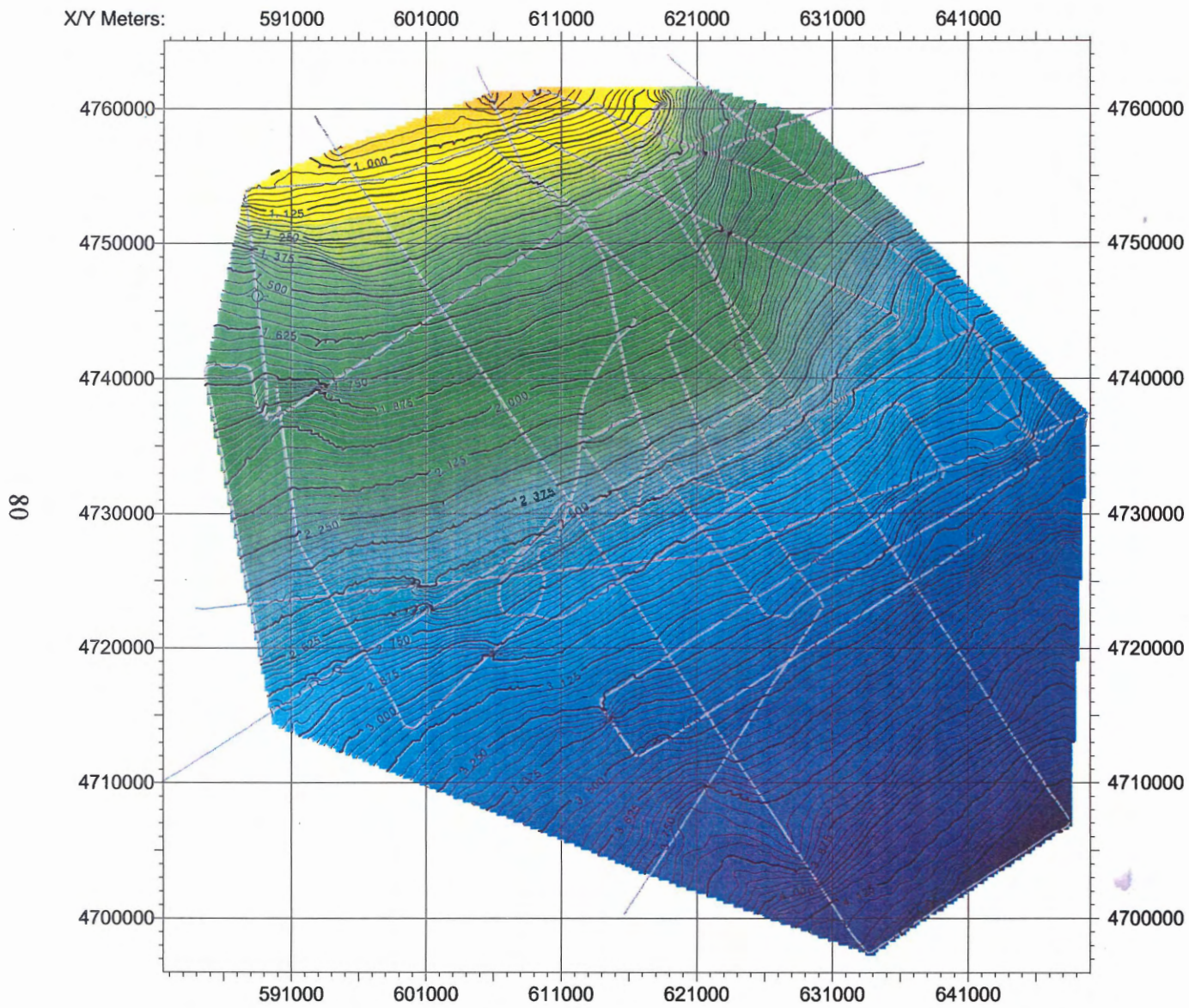
Figure A6: Flesh horizon structure map. Scale bar indicates TWTT in seconds. Contour interval is 25 ms with bold contours every 125 ms.
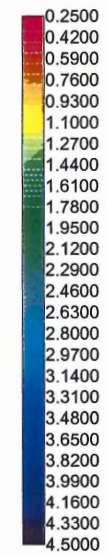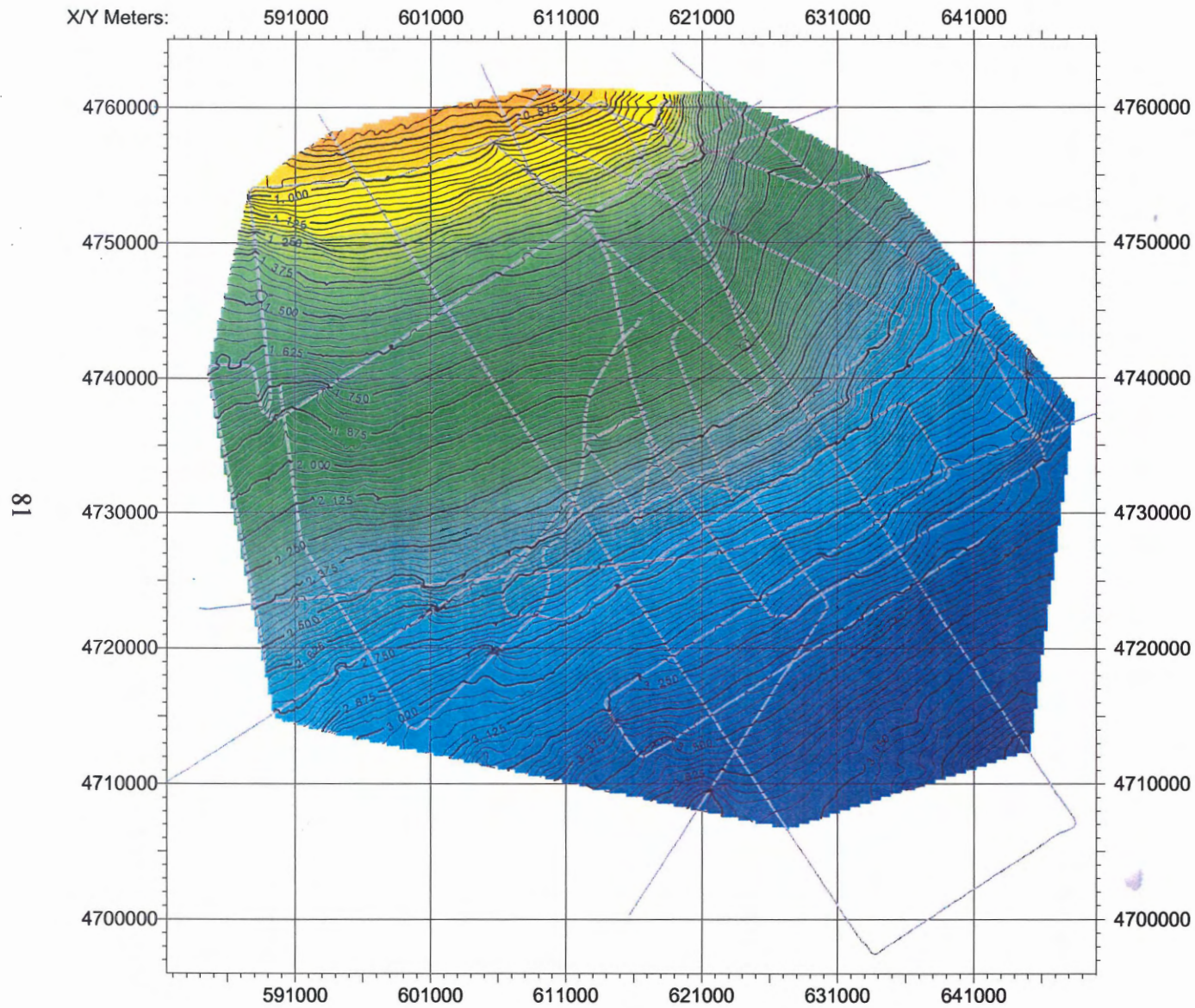
Figure A7: Carmine horizon structure map. Scale bar indicates TWTT in seconds. Contour interval is 25 ms with bold contours every 125 ms.
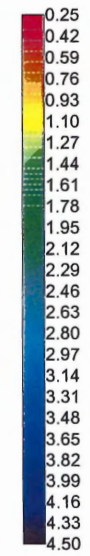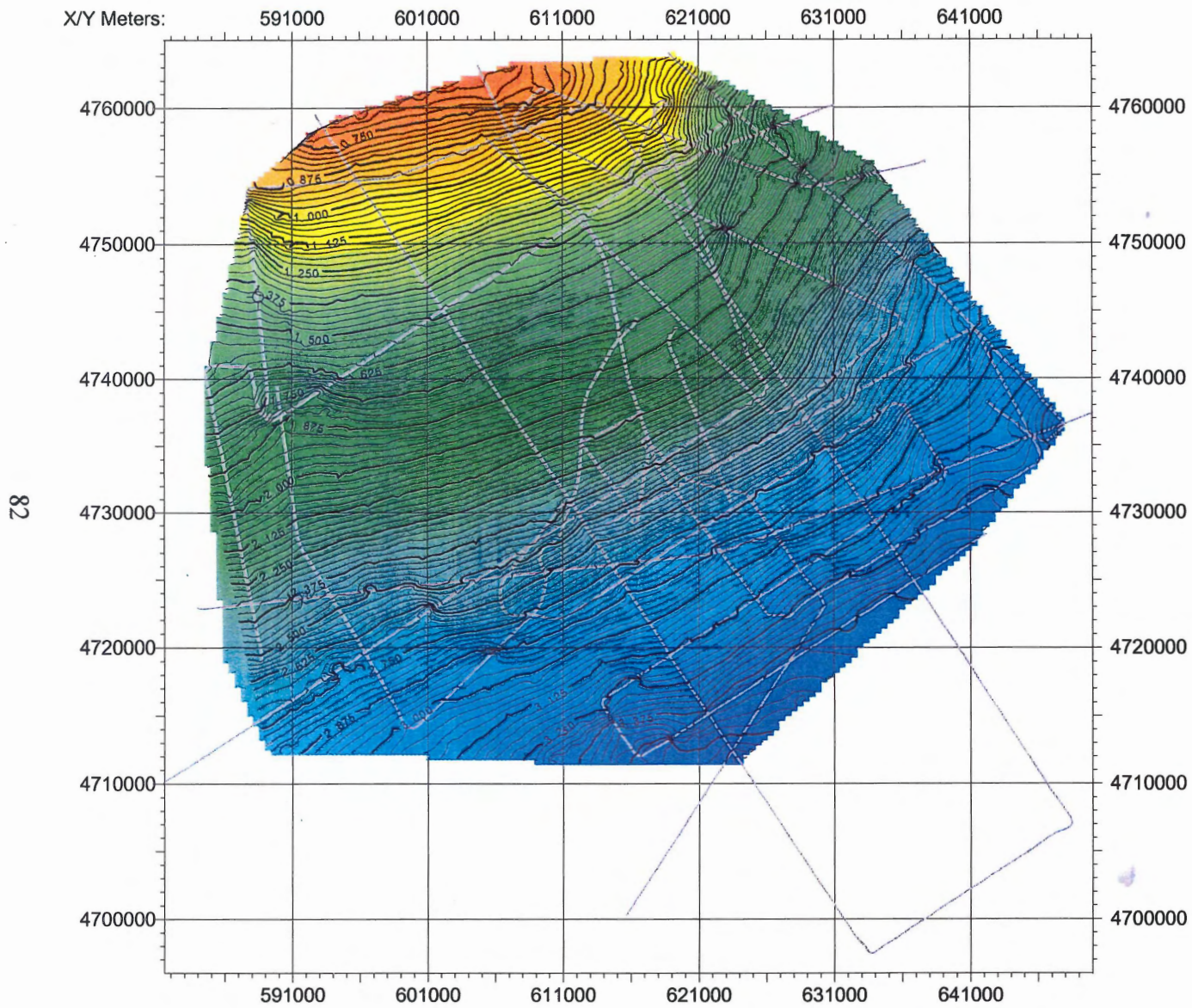
Figure A8: Brown horizon structure map. Scale bar indicates TWTT in seconds. Contour interval is 25 ms with bold contours every 125 ms.
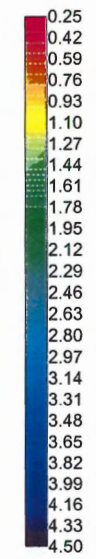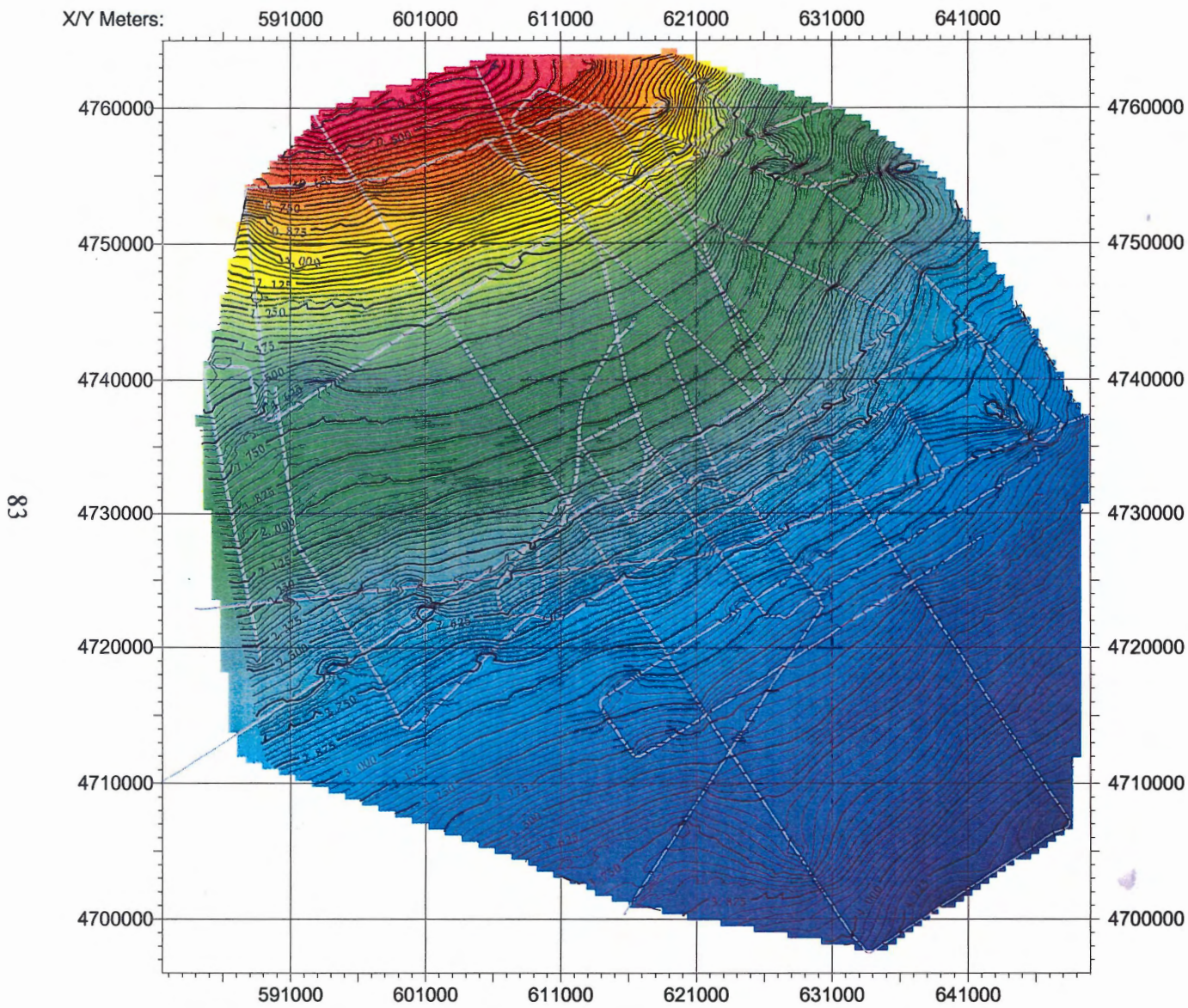
Figure A9: Seafloor structure map. Scale bar indicates TWTT in seconds. Contour interval is 25 ms with bold contours every 125 ms.

APPENDIX B:
ISOCHRON MAPS FROM REFLECTION PROFILES

TABLE OF CONTENTS
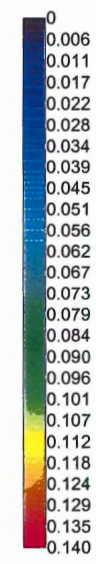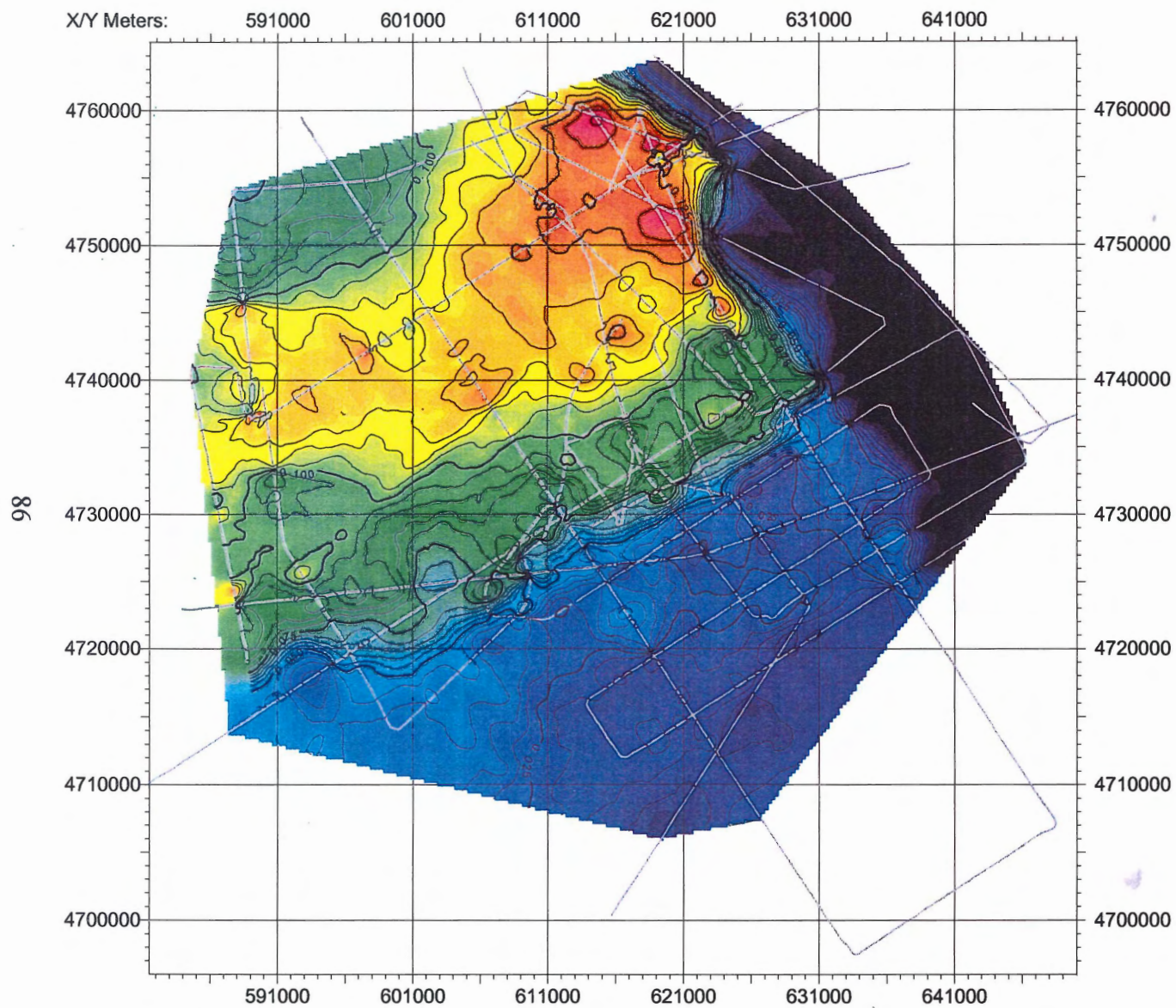
Figure B1: Red-blue isochron. Contour interval is 5 ms TWTT with bold contour every fifth interval. Scale is TWTT in seconds.
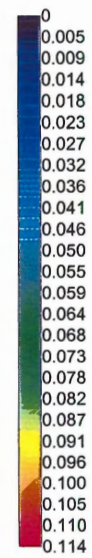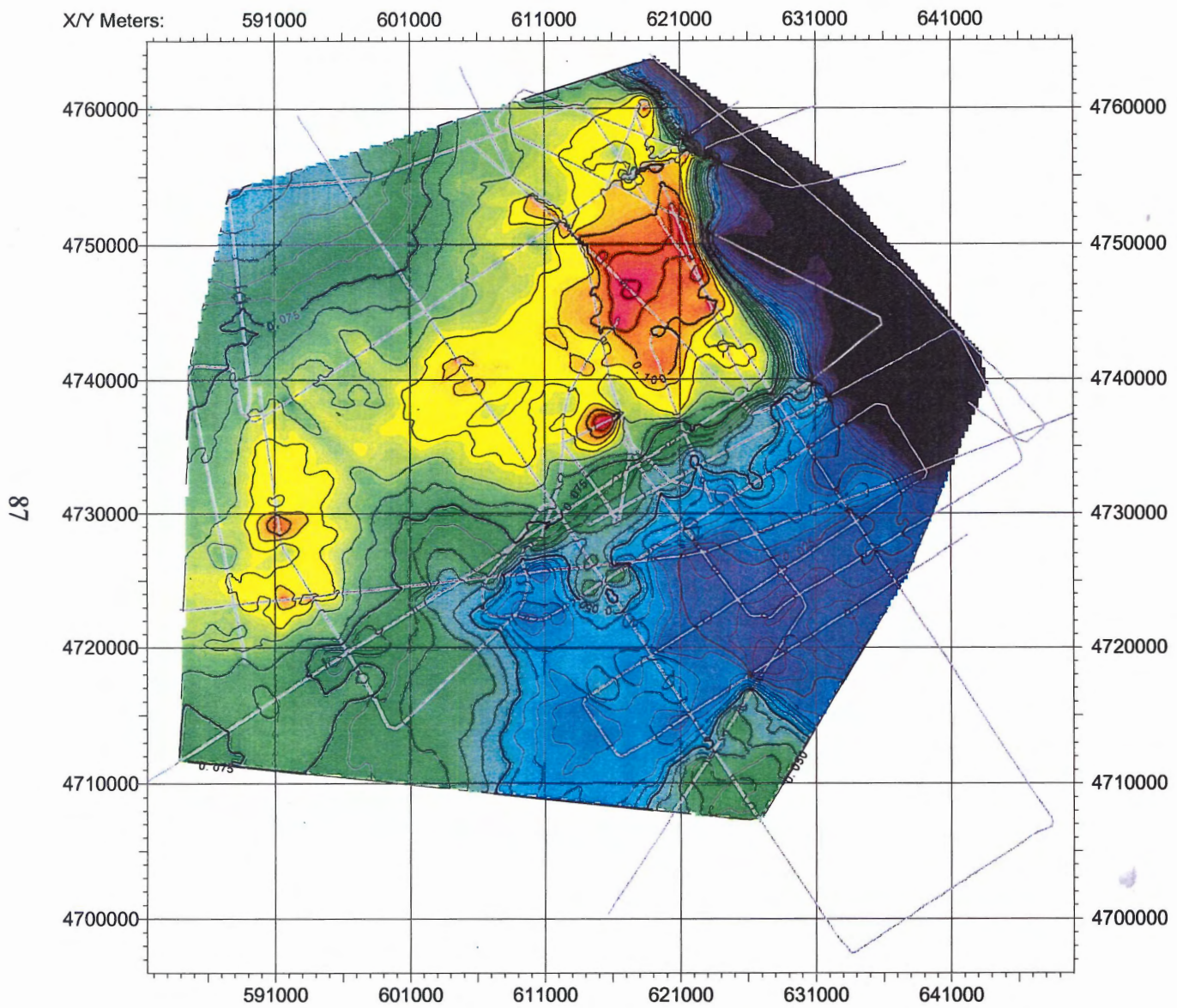
Figure B2: Blue-magenta isochron. Contour interval is 5 ms TWTT with bold contour every fifth interval. Scale is TWTT in seconds.
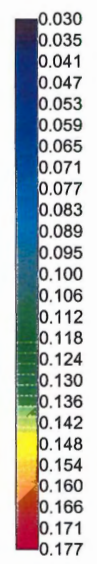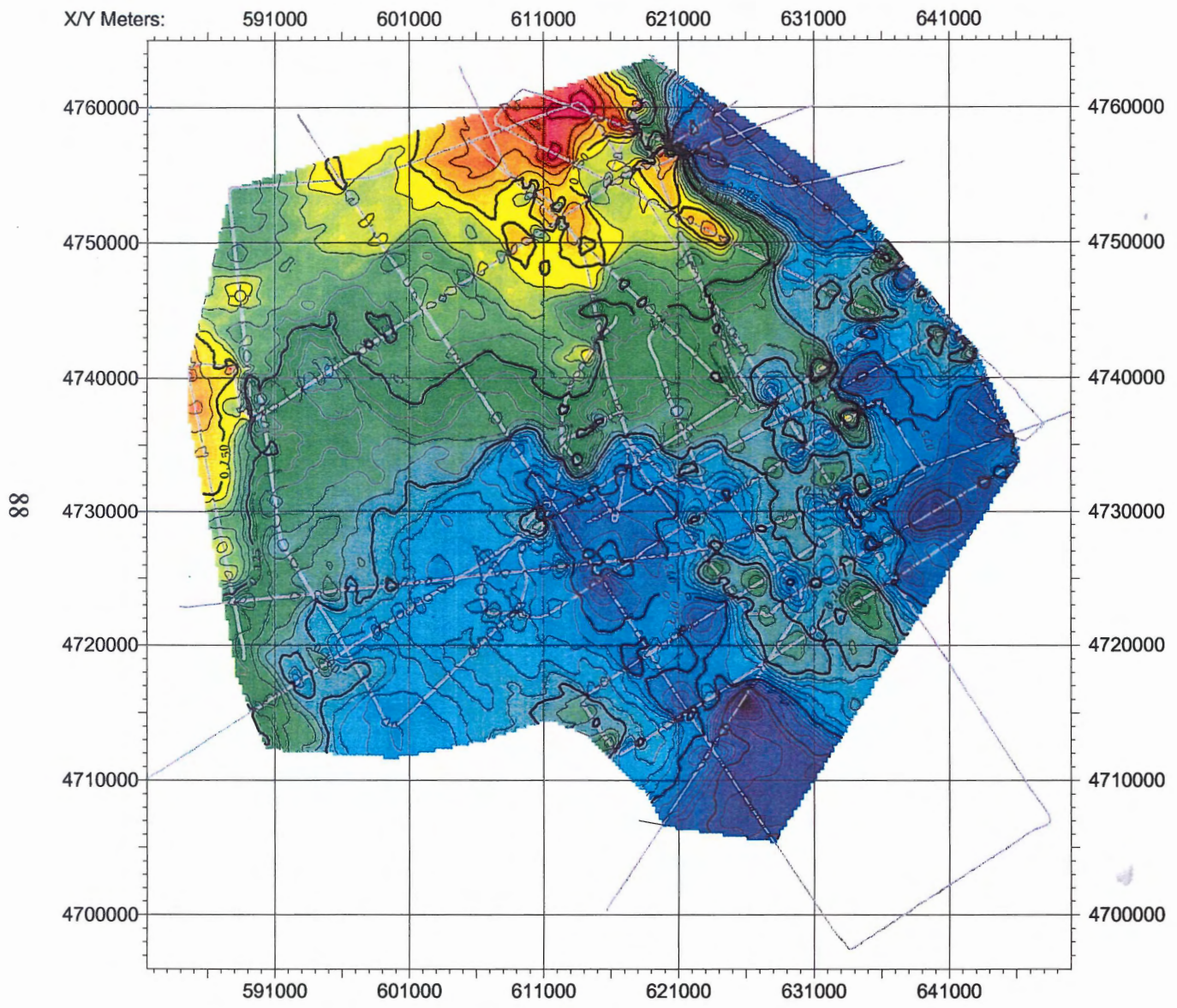
Figure B3: Magenta-grey isochron. Contour interval is 5 ms TWTT with bold contour every fifth interval. Scale is TWTT in seconds.
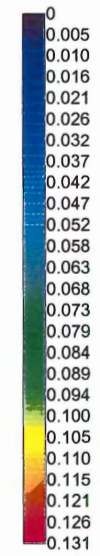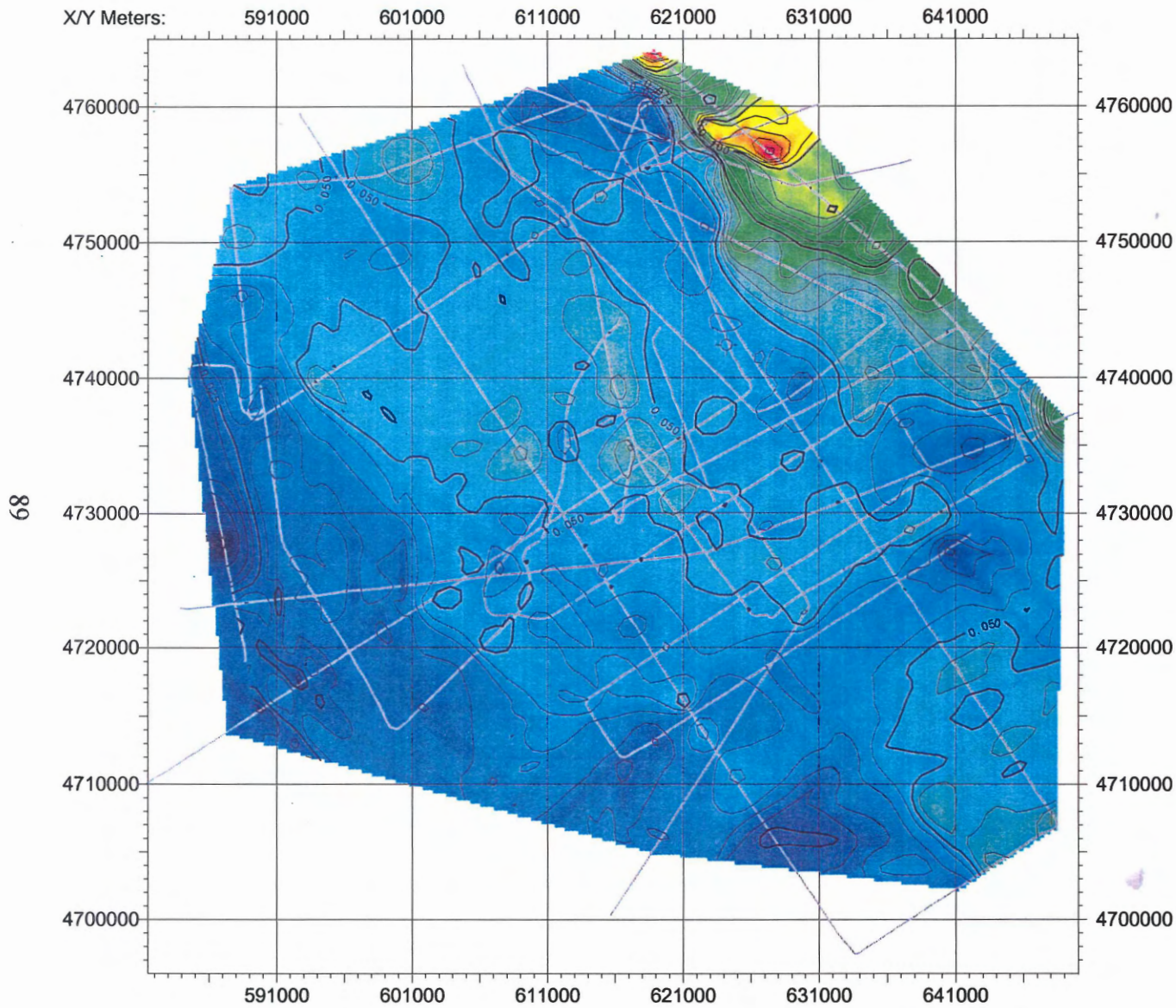
Figure B4: Grey-rose isochron. Contour interval is 5 ms TWTT with bold contour every fifth interval. Scale is TWTT in seconds.

68
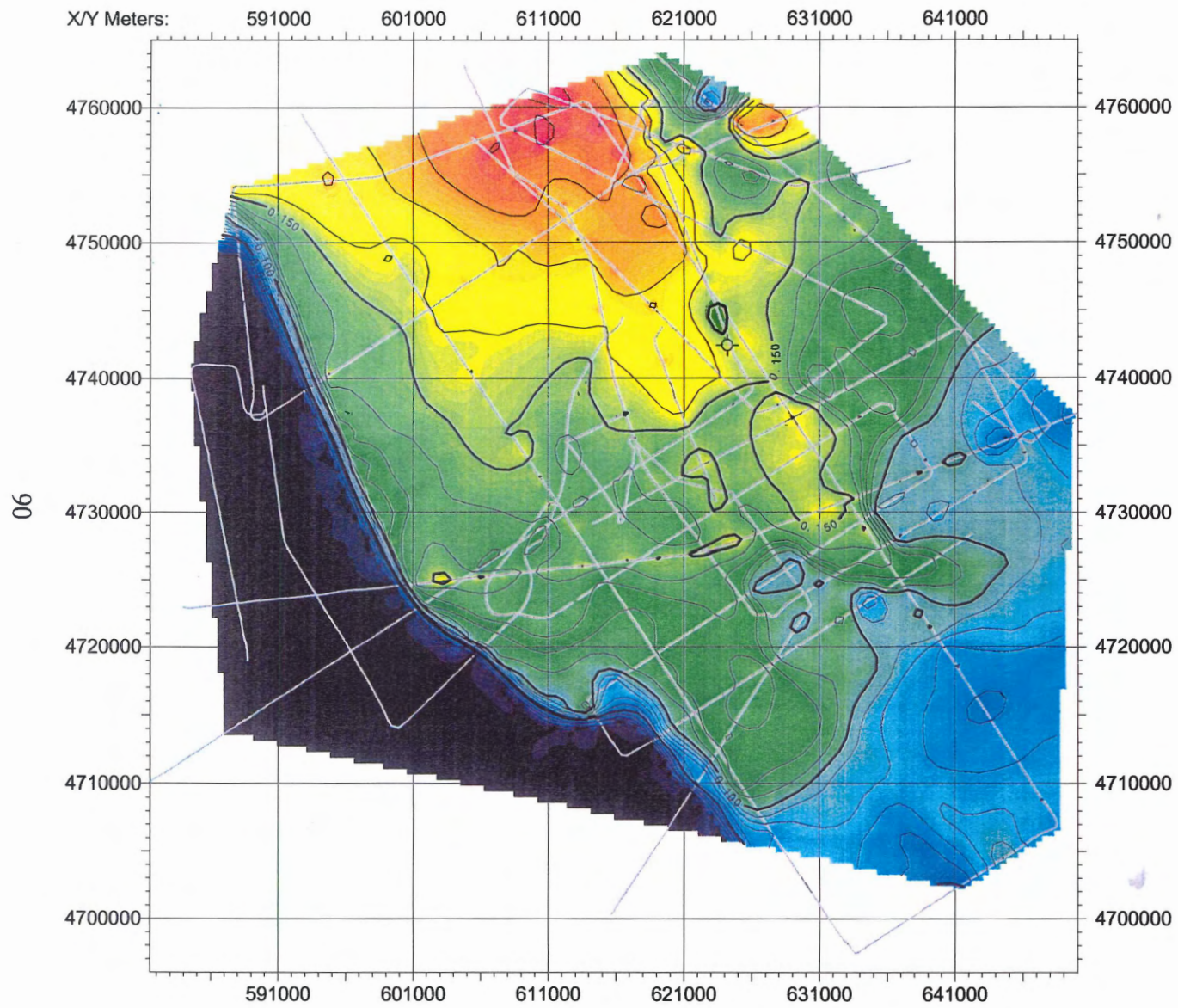
Figure B5: Rose-flesh isochron. Contour interval is 10 ms TWTT with bold contour every fifth interval. Scale is TWTT in seconds.
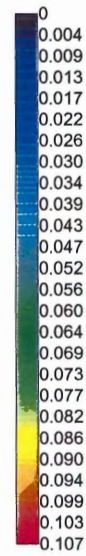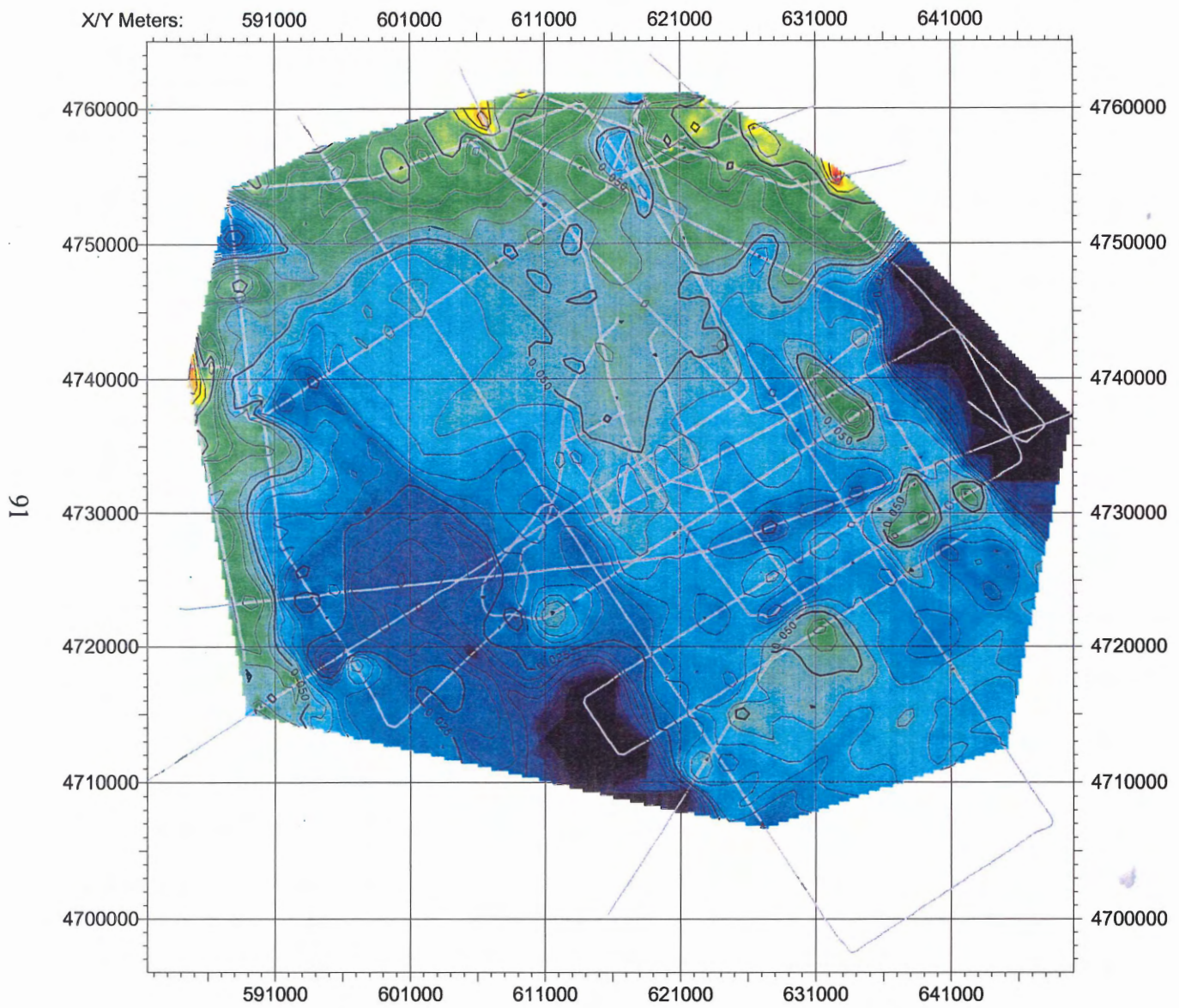
Figure B6: Flesh-carmine isochron. Contour interval is 5 ms TWTT with bold contour every fifth interval. Scale is TWTT in seconds.
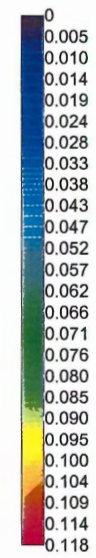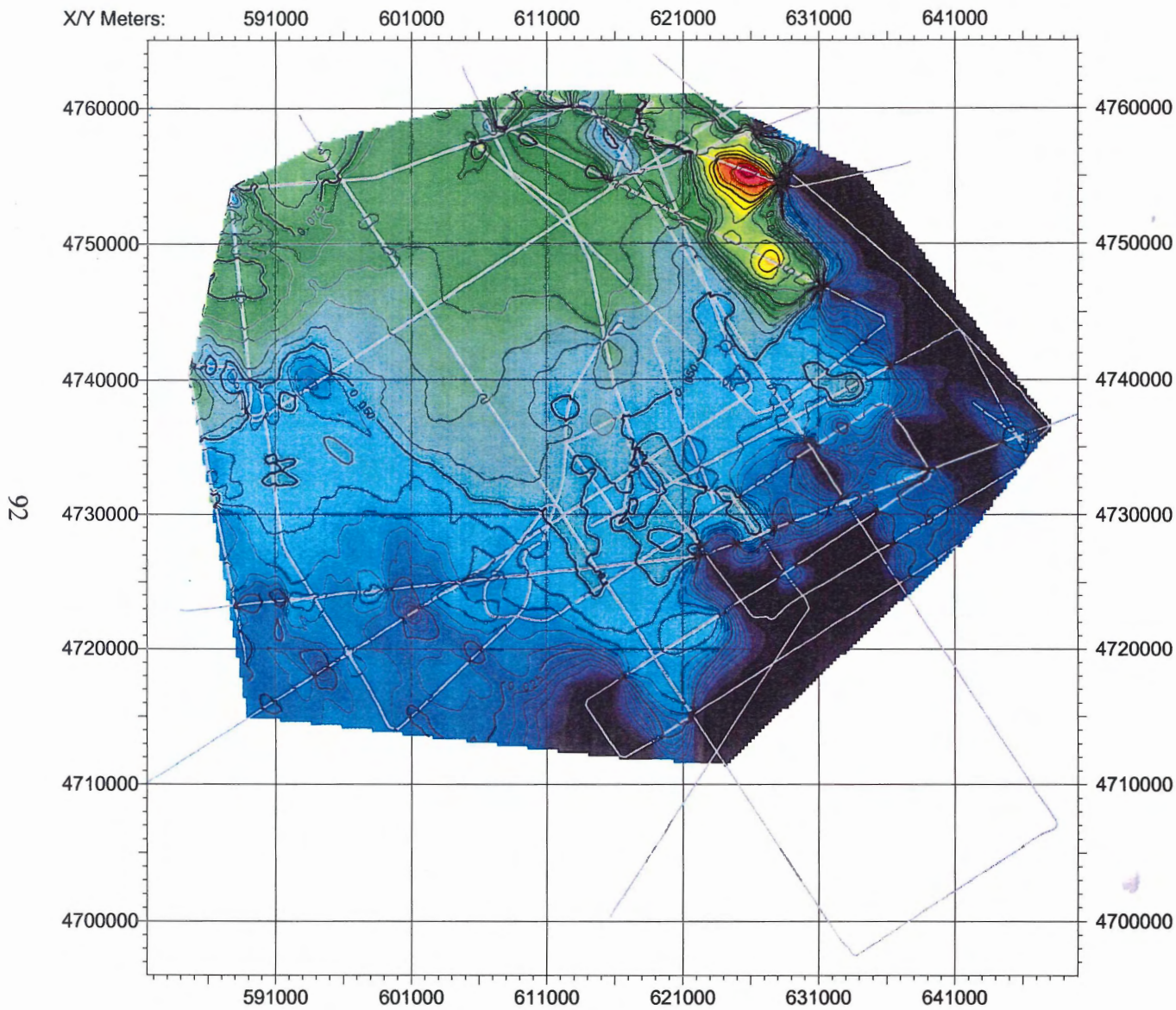
Figure B7: Carmine-brown isochron. Contour interval is 5 ms TWTT with bold contour every fifth interval. Scale is TWTT in seconds.
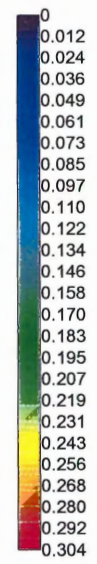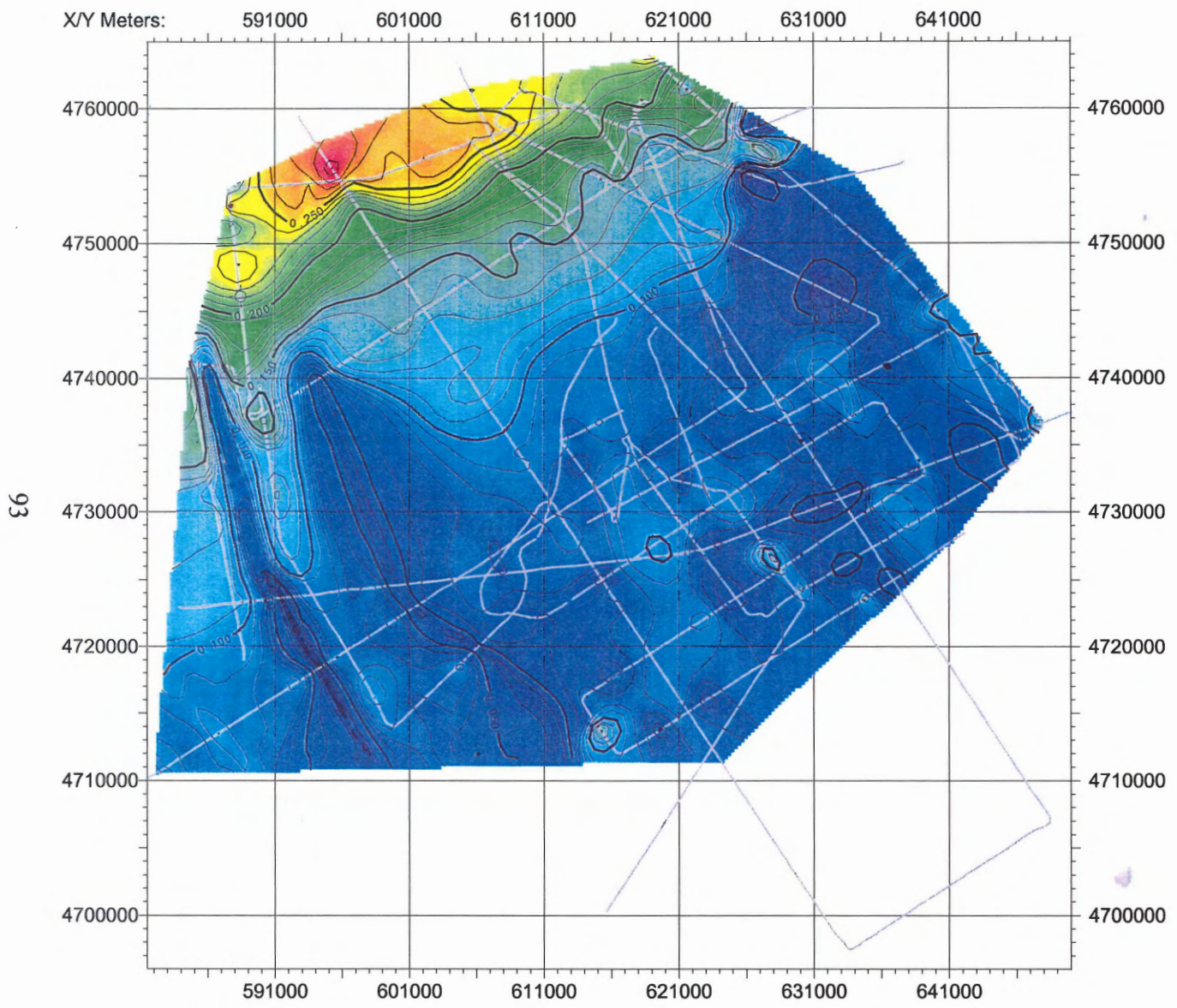
Figure B8: Brown-seafloor isochron. Contour interval is 10 ms TWTT with bold contour every fifth interval. Scale is TWTT in seconds.

93
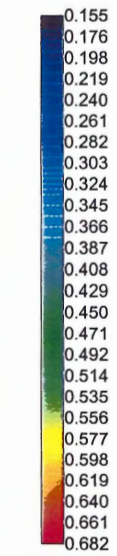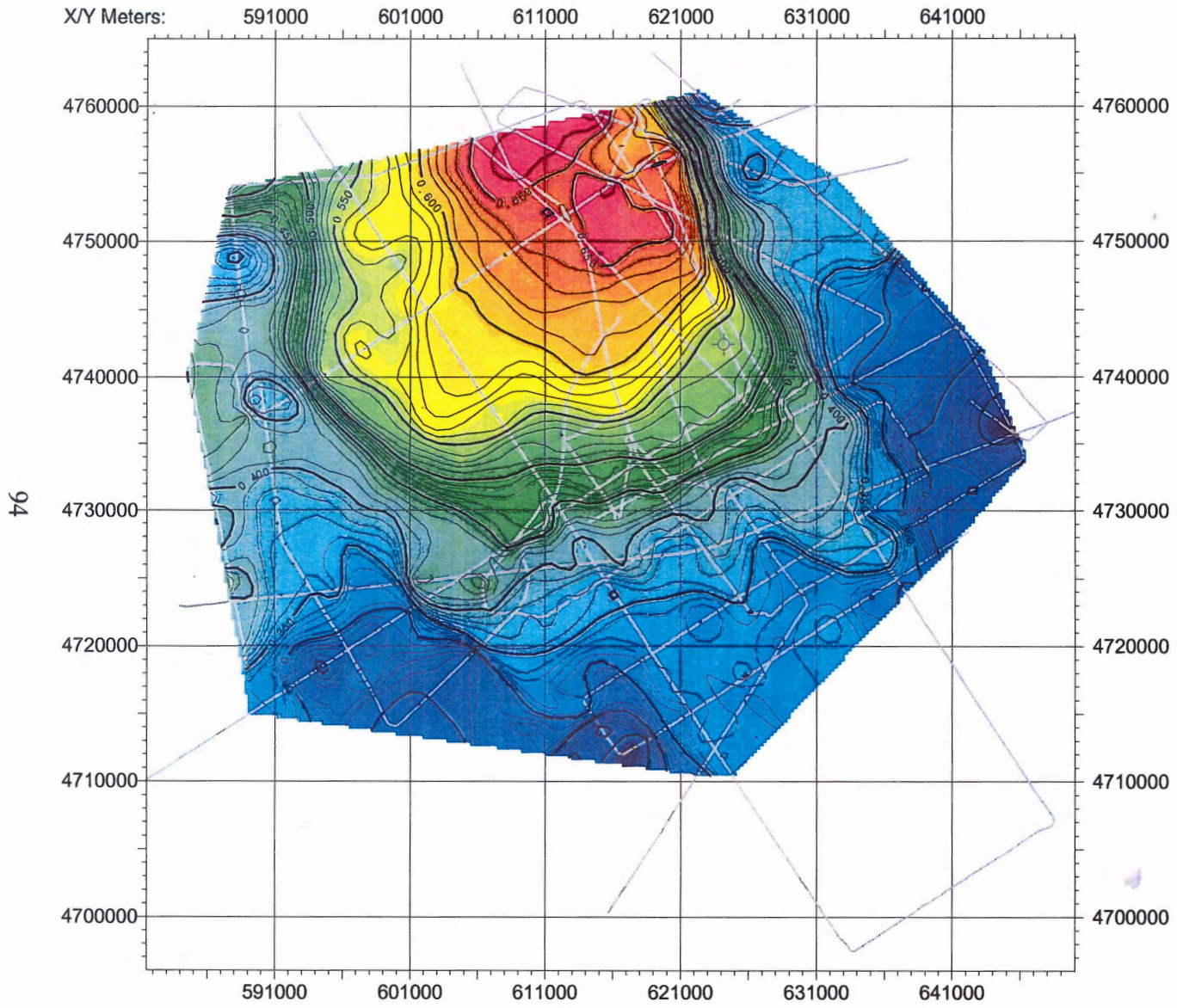
Figure B9: Red-carmine isochron. Contour interval is 10 ms TWTT with bold contour every fifth interval. Scale is TWTT in seconds.
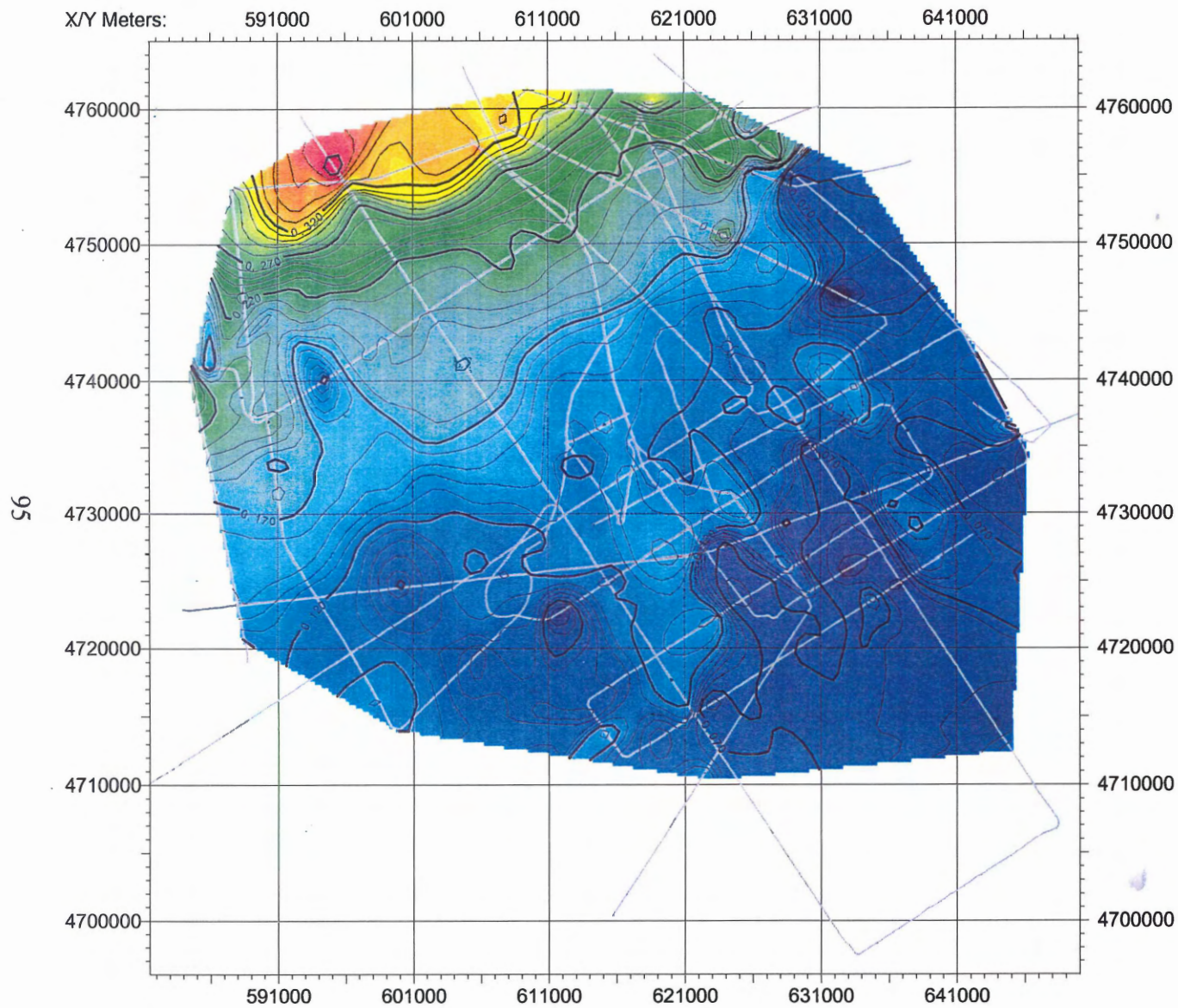
Figure B10: Carmine-seafloor isochron. Contour interval is 10 ms TWTT with bold contour every fifth interval. Scale is TWTT in seconds.
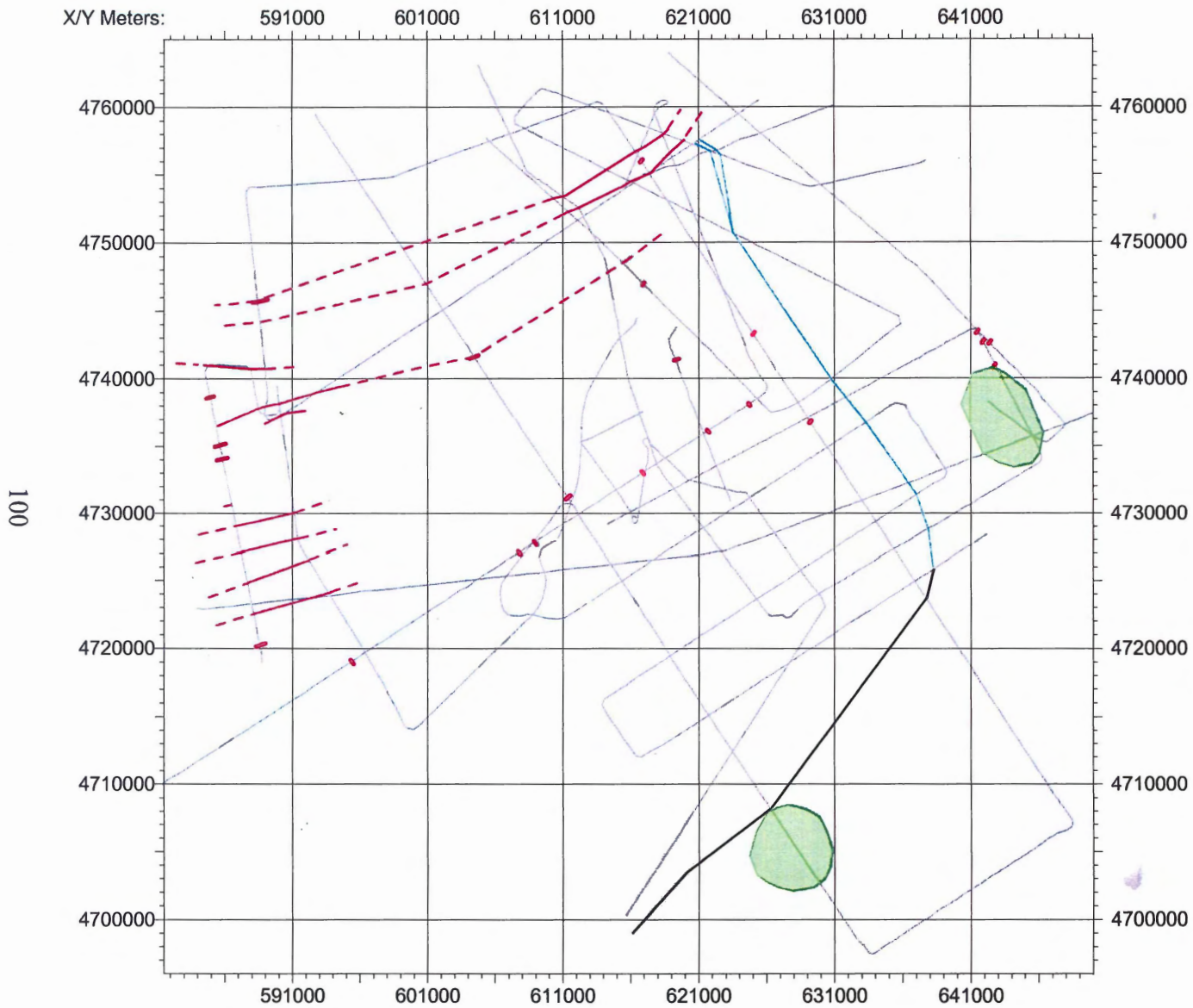
APPENDIX C:
INTERVAL FEATURE MAPS

TABLE OF CONTENTS

Figure C1: Significant features identified at the red horizon. Fault correlations are tentative and do not imply activity during the interval. Limit of correlation indicates where salt dome related features inhibit accurate correlations. Erosion in northeast area likely occurred during the magenta-grey interval.

key to symbols

- Type 1 fault
- Type 2 fault (uncorrelatable, tentative correlation, correlatable)
- channel (inferred)
- significant erosion of interval (inferred, observed)
- unidentified feature
- limit of correlation
- salt deformation
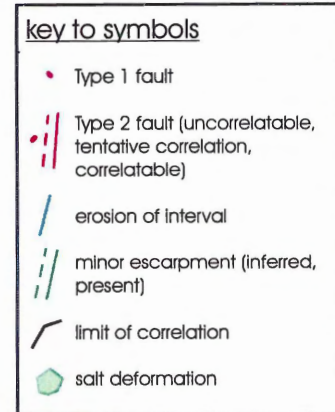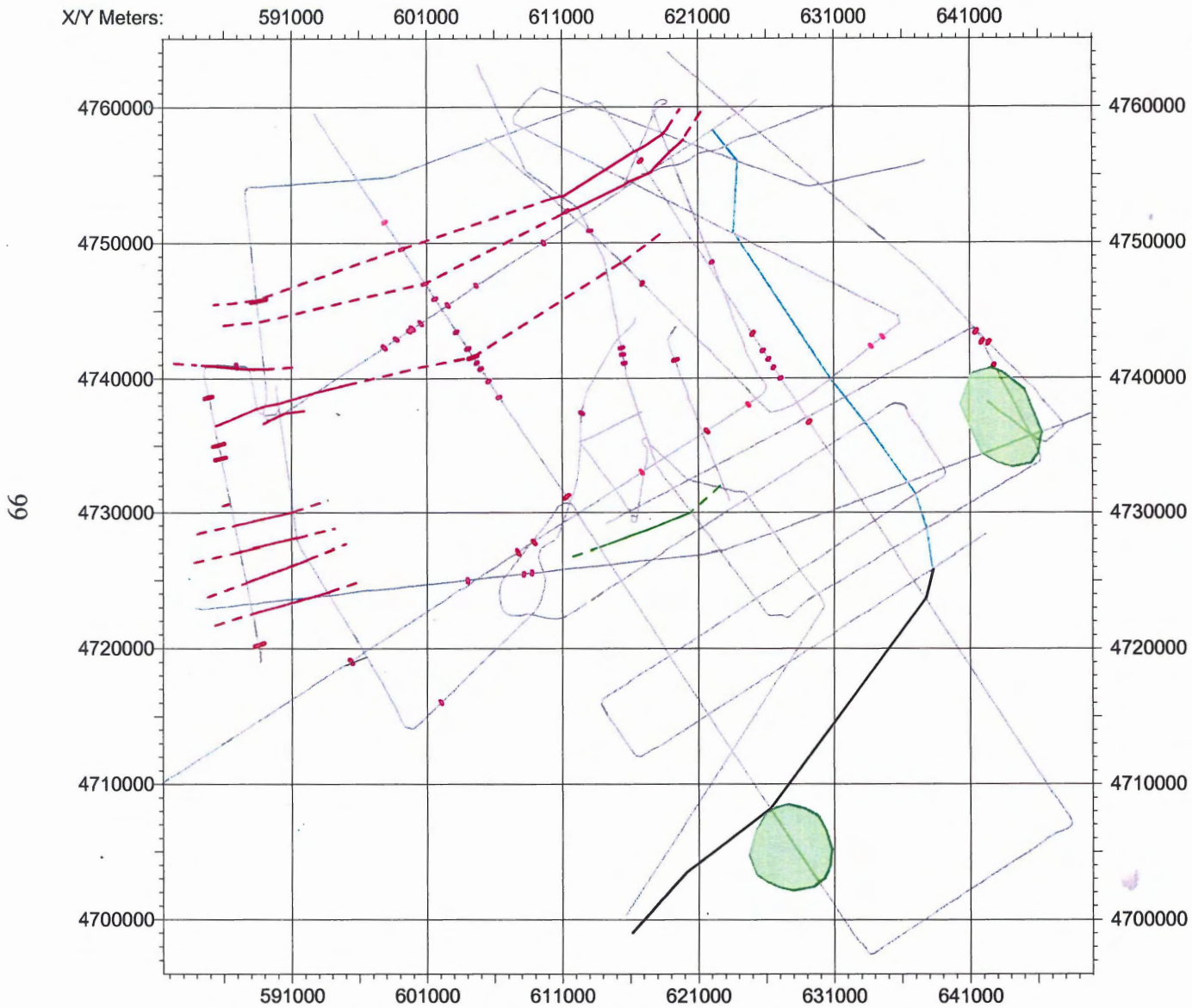
Figure C2: Significant features identified in the red-blue interval. Fault correlations are tentative and do not imply activity during the interval. Limit of correlation indicates where salt dome related features inhibit accurate correlations. Erosion in the eastern region occurred during the magenta-grey interval.
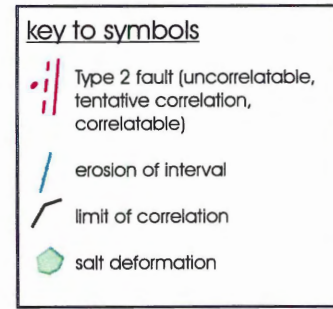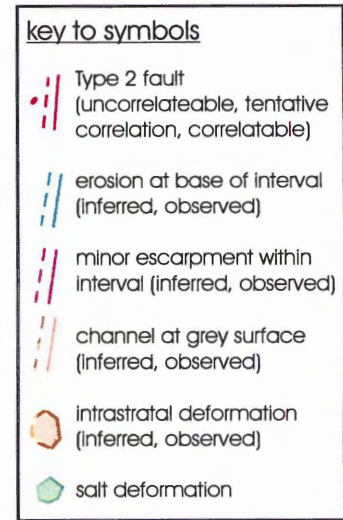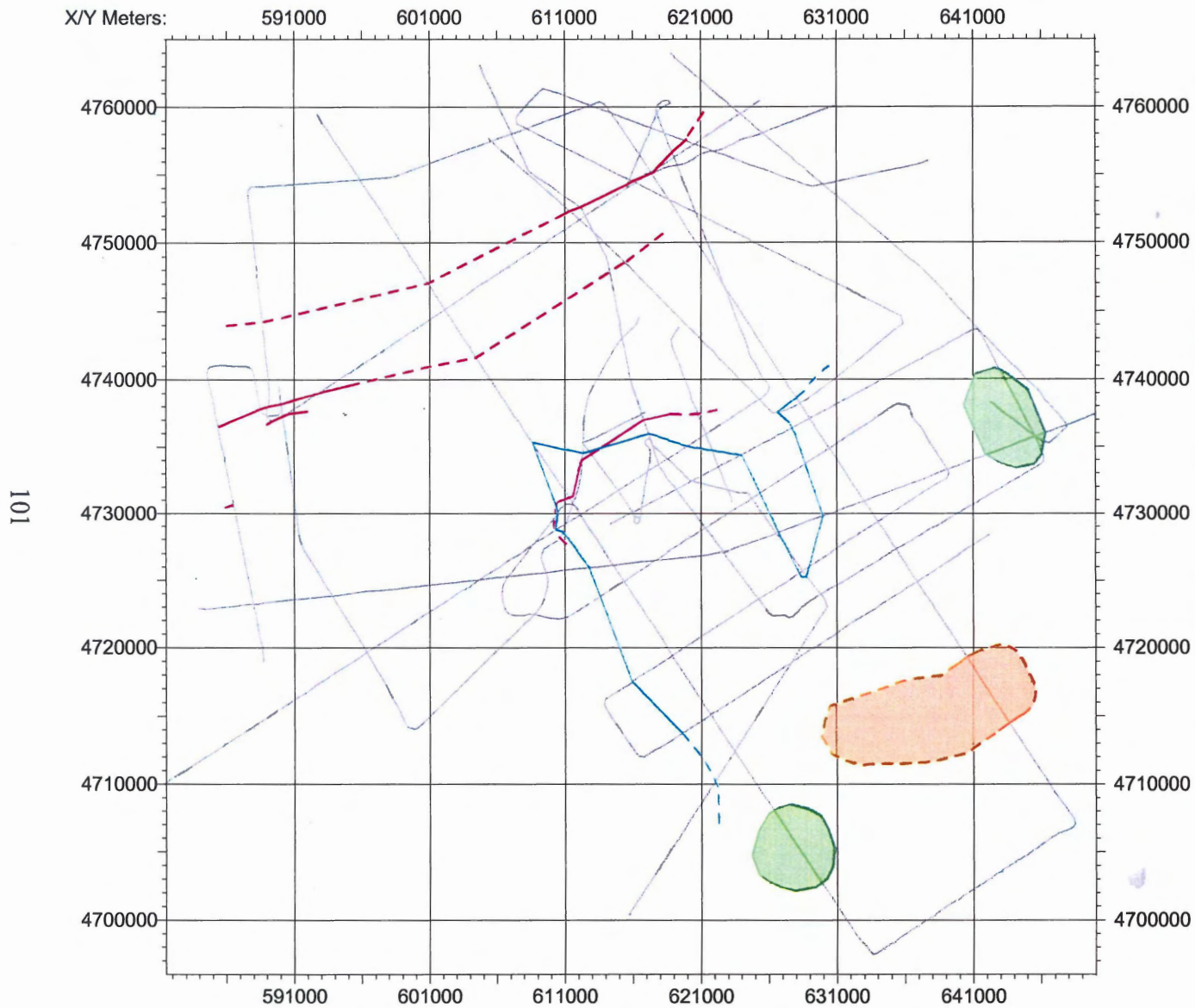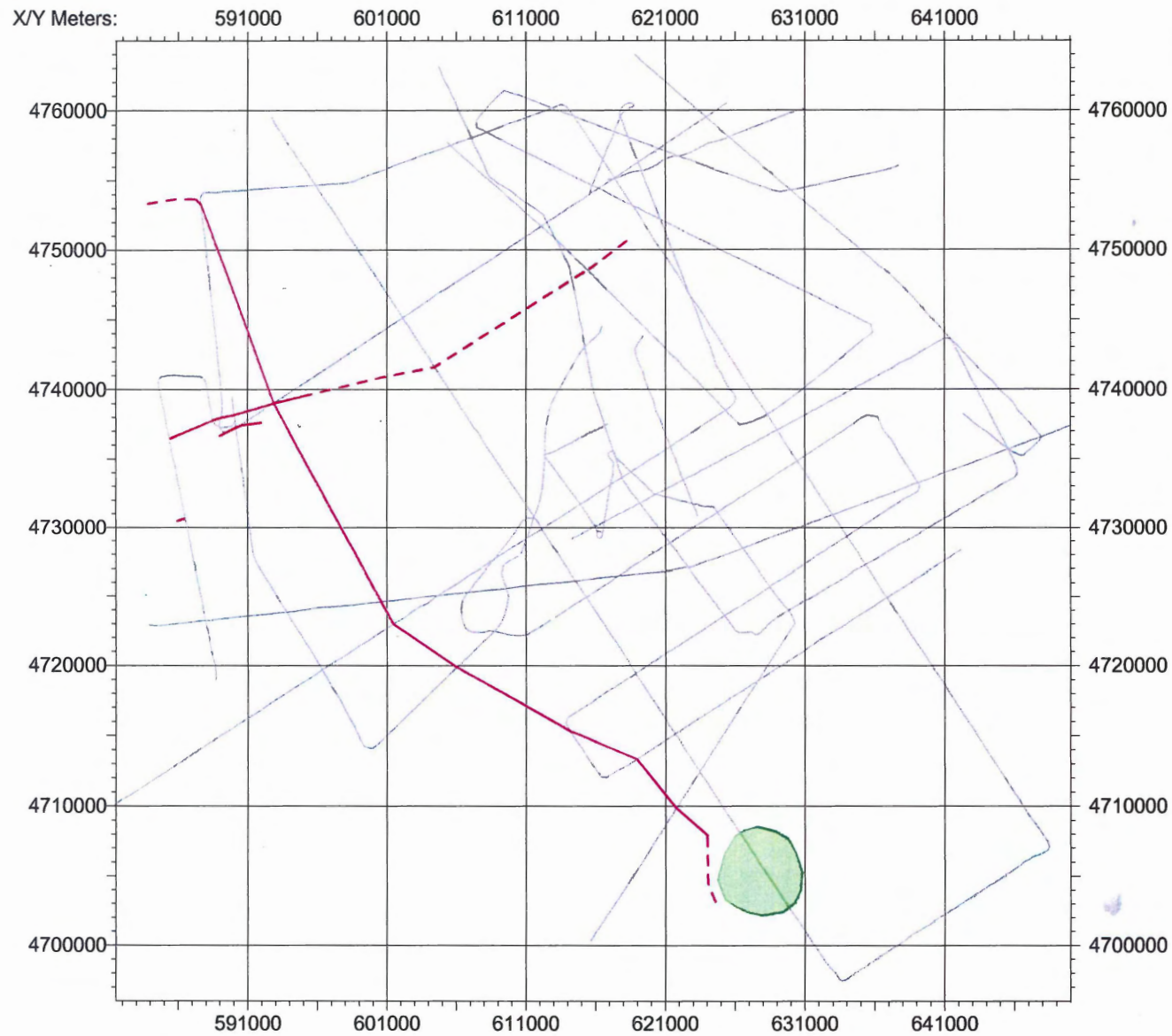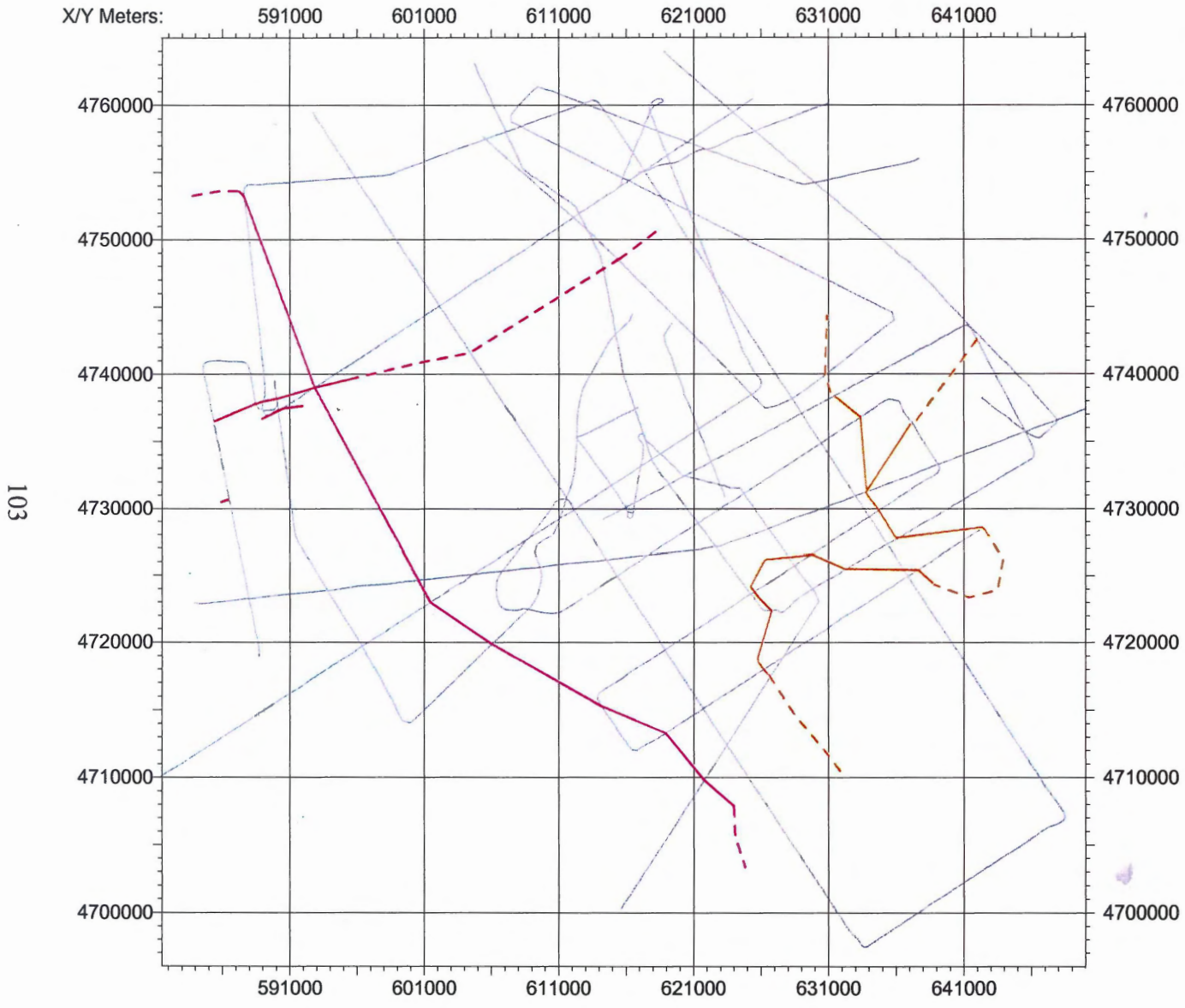
Figure C3: Significant features identified in the blue-magenta interval. Fault correlations are tentative and do not imply activity during the interval. Limit of correlation indicates where salt dome related features inhibit accurate correlations. Erosion in the eastern region occurred during the magenta-grey interval.

key to symbols

- Type 2 fault (uncorrelatable, tentative correlation, correlatable)
- erosion of interval
- limit of correlation
- salt deformation

Figure C4: Significant features identified in the magenta-grey interval. Fault correlations are tentative and do not imply activity during the interval. Intrastratal deformation is related to salt. Erosion in the eastern region occurred during the magenta-grey interval.

key to symbols

Type 2 fault (uncorrelateable, tentative correlation, correlatable)

erosion at base of interval (inferred, observed)

minor escarpment within interval (inferred, observed)

channel at grey surface (inferred, observed)

intrastratal deformation (inferred, observed)

salt deformation

Figure C5: Significant features identified in the grey-rose interval. Fault correlations are tentative and do not imply activity during the interval. Escarpment in the western region occurred during the flesh-carmine interval.
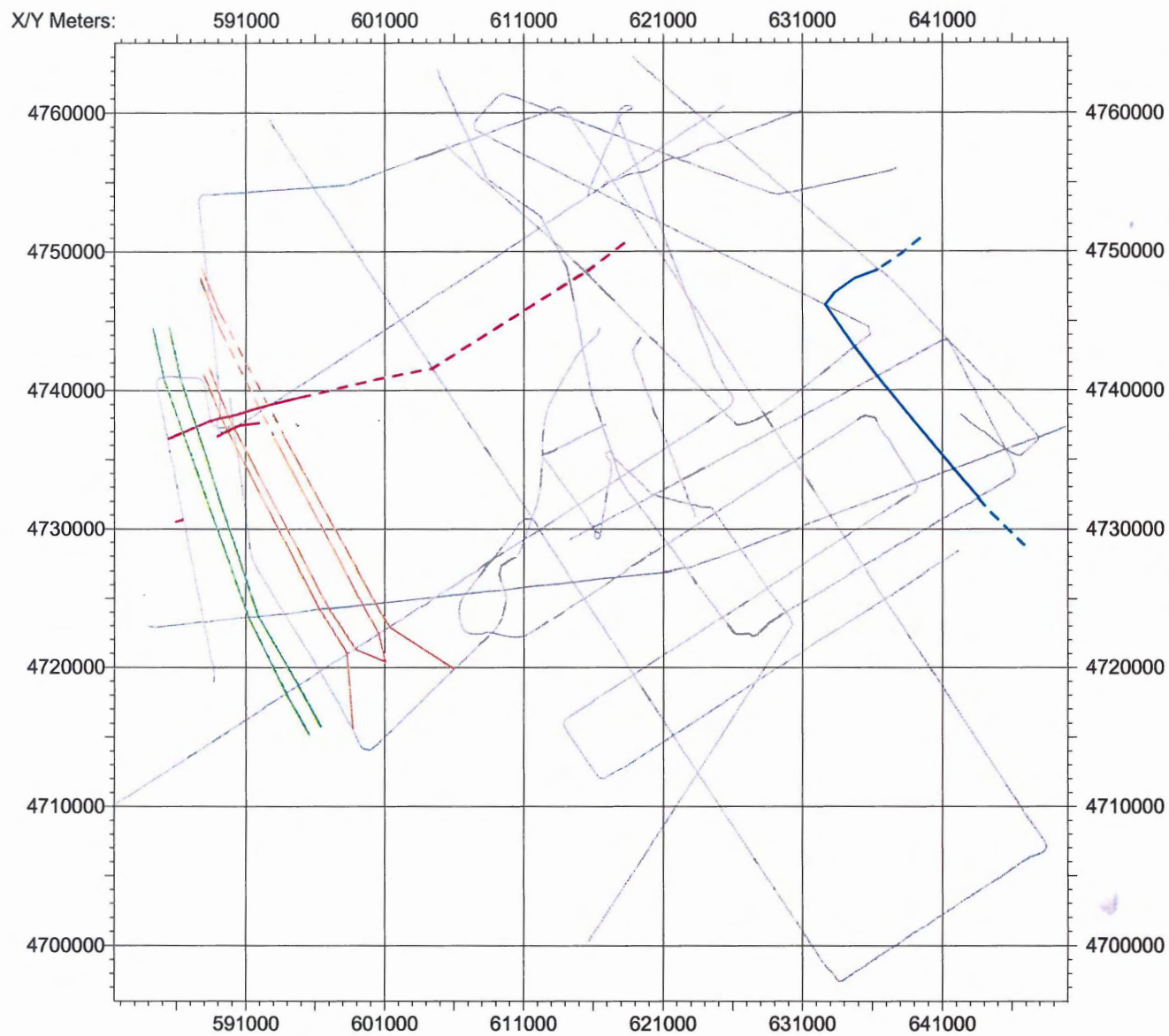
Figure C6: Significant features identified in the rose-flesh interval. Fault correlations are tentative and do not imply activity during the interval. Escarpment in the western region occurred during the flesh-carmine interval.

key to symbols

Type 2 fault
(uncorrelateable, tentative correlation, correlatable)

major escarpment
(inferred, observed)

minor escarpment within interval (inferred, observed)

103

Figure C7: Significant features identified in the flesh-carmine interval. Fault correlations are tentative and do not imply activity during the interval. Channels in the western region developed following an escarpment at the base of the interval.
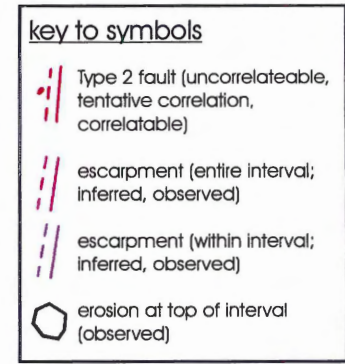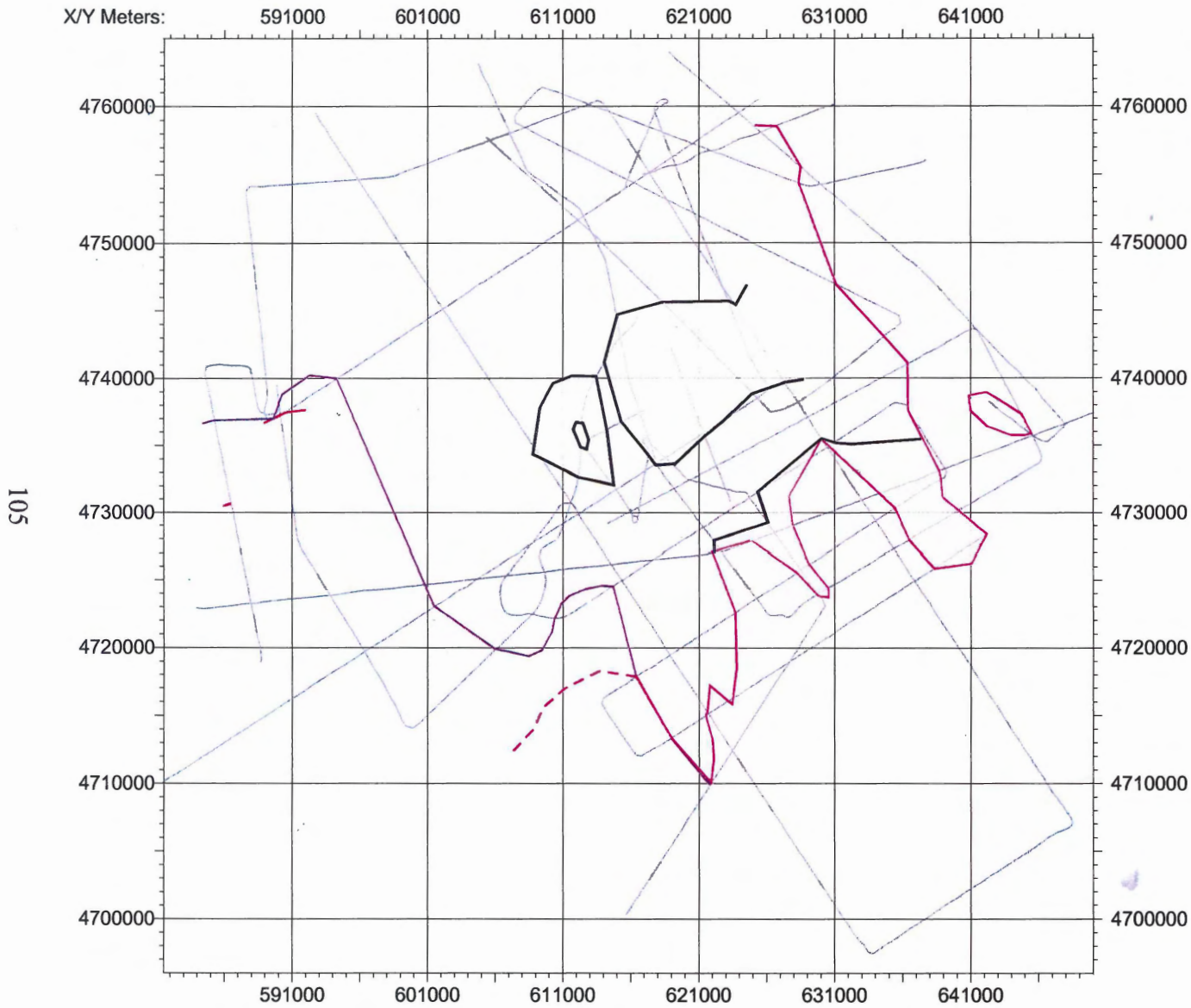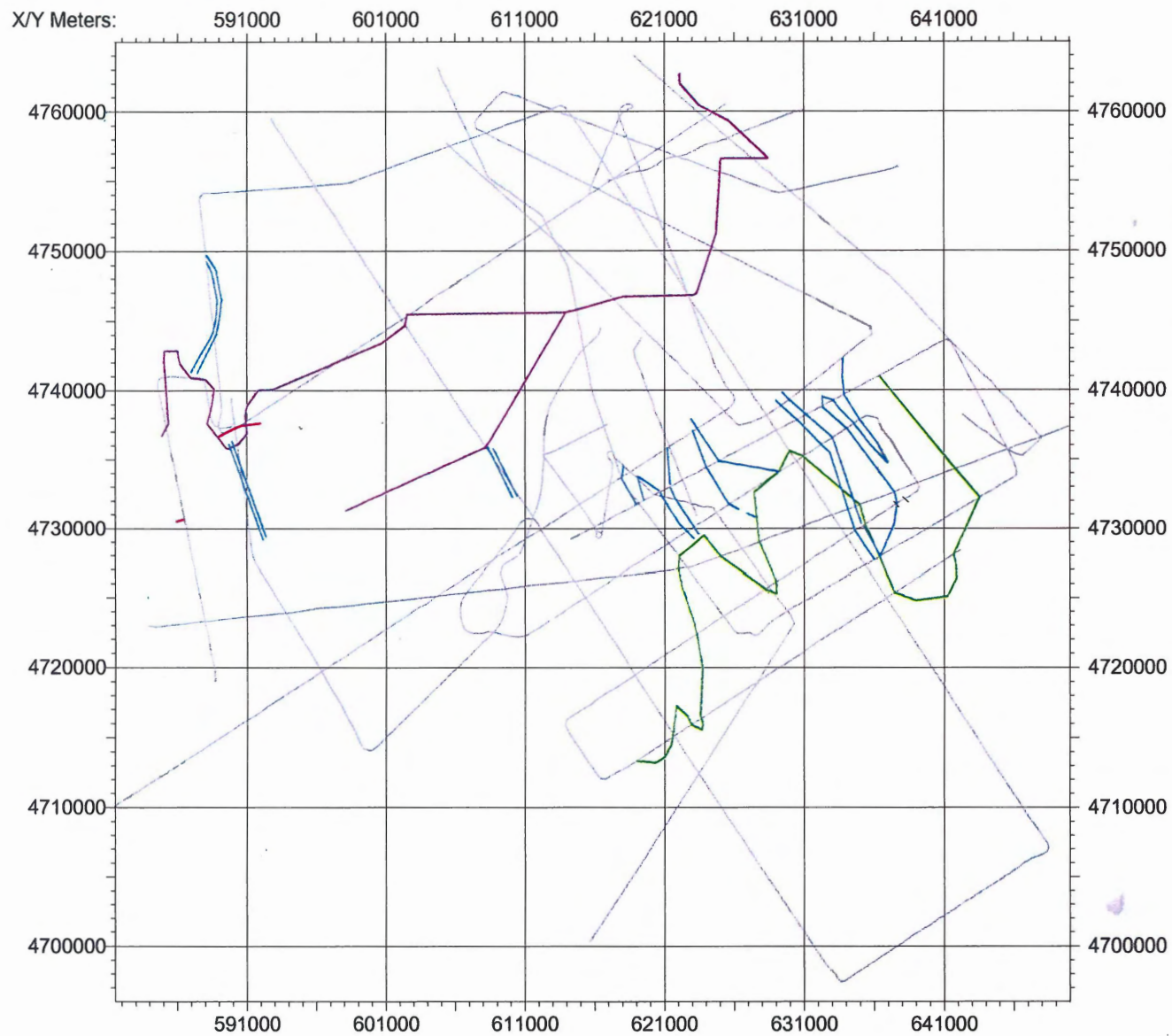
key to symbols

Type 2 fault (uncorrelateable, tentative correlation, correlatable)

levied channel (inferred, observed)

erosional channel (inferred, observed)

escarpment (entire interval; inferred, observed)

X/Y Meters:

104

Figure C8: Significant features identified in the carmine-brown interval. Fault correlations are tentative and do not imply activity during the interval.

key to symbols

Type 2 fault (uncorrelateable, tentative correlation, correlatable)

escarpment (entire interval; inferred, observed)

escarpment (within interval; inferred, observed)

erosion at top of interval (observed)

Figure C9: Significant features identified in the brown-light red interval. Fault correlations are tentative and do not imply activity during the interval.

key to symbols

Type 2 fault (uncorrelateable, tentative correlation, correlatable)

escarpment (minor; inferred, observed)

escarpment (base of interval; inferred, observed)

channel (inferred, observed))

X/Y Meters:

106

key to symbols

Type 2 fault (uncorrelateable, tentative correlation, correlatable)

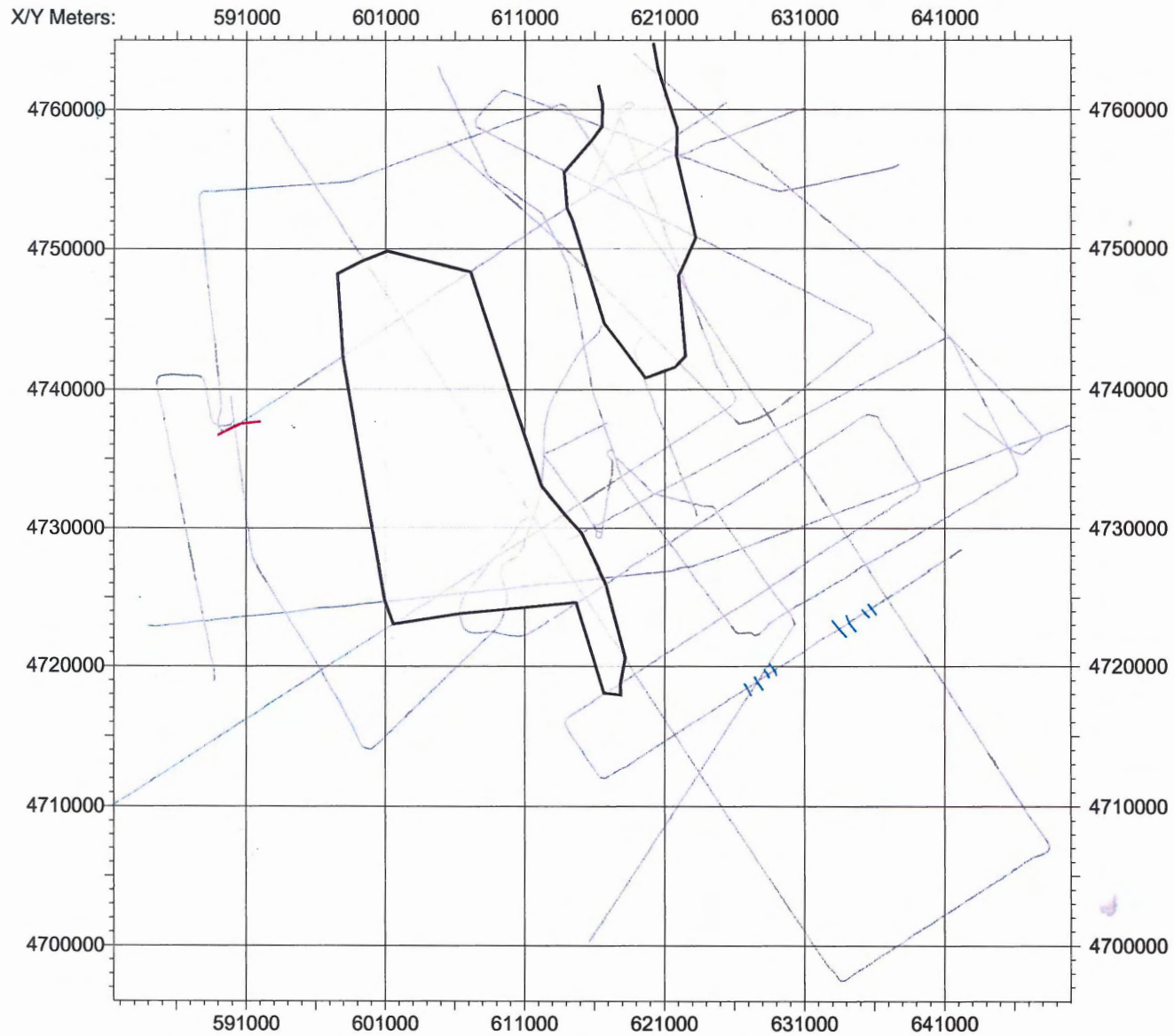channel

erosion at top of interval (observed)

Figure C10: Significant features identified in the light red-seafloor interval. Fault correlations are tentative and do not imply activity during the interval. Channels on lowers slope cannot be correlated upslope.

APPENDIX D:
SEISMIC SECTIONS INTERPRETED

Line	Bulk Shift (seconds)	Survey	Year Acquired
Line036-59	0	HUD2000-036	2000
Line036-60	0	HUD2000-036	2000
Line036-61_62	-0.006	HUD2000-036	2000
Line036-63	-0.004	HUD2000-036	2000
Line036-64	-0.004	HUD2000-036	2000
Line042-67	0.41	HUD2000-042	2000
Line042-68	0	HUD2000-042	2000
Line042-69_west	1.605	HUD2000-042	2000
Line042-70	0.006	HUD2000-042	2000
Line042-71	0.006	HUD2000-042	2000
Line042-72	0.01	HUD2000-042	2000
Line042-73	0.003	HUD2000-042	2000
Line042-74	0.008	HUD2000-042	2000
Line042-75	0.008	HUD2000-042	2000
Line048A_29	0.002	HUD2001-048A	2001
Line048A_30	0.502	HUD2001-048A	2001
Line048A_31	0.002	HUD2001-048A	2001
Line048A_32	0.012	HUD2001-048A	2001
Line048A_33	3.598	HUD2001-048A	2001
Line048A_34	-0.007	HUD2001-048A	2001
Line048A_35	-0.007	HUD2001-048A	2001
Line048A_36	0.0035	HUD2001-048A	2001
Line048A_37	2.405	HUD2001-048A	2001
Line048A_38	0.005	HUD2001-048A	2001
Line048A_39	2.803	HUD2001-048A	2001
Line048A_40	2.803	HUD2001-048A	2001
Line048A_41	0.007	HUD2001-048A	2001
Line2002-046-55	2.007	HUD2002-046	2002
Line2002-046-56	0.011	HUD2002-046	2002
Line2002-046-57	0.4141	HUD2002-046	2002
Line2002-046-58	0.4147	HUD2002-046	2002
Line98039-19_west	2.505	HUD98039	1998
Line98039-20	2.005	HUD98039	1998
Line99036-102	0.2125	HUD99036	1999
Line99036-103	1.9105	HUD99036	1999
Line99036-104	0	HUD99036	1999
Line99036-105	2	HUD99036	1999
Line99036-108	1.1044	HUD99036	1999
Line99036-109	1.1044	HUD99036	1999
Line99036-110	1.6044	HUD99036	1999
Line99036-111	1.3044	HUD99036	1999
Line99036-112	0.3044	HUD99036	1999